Electro-Chemo-Mechanical Phenomena in Solid-State Battery Electrodes and Interfaces

by

Andrew L. Davis

A dissertation submitted in partial fulfillment
of the requirements for the degree of
Doctor of Philosophy
(Mechanical Engineering)
in the University of Michigan
2021

Doctoral Committee:

Associate Professor Neil P. Dasgupta, Chair
Associate Professor Jeff Sakamoto
Professor Donald J. Siegel
Professor Katsuyo Thornton

Andrew L Davis

AndrewLD@umich.edu

ORCID iD: 0000-0002-4264-5259

This dissertation is dedicated to my parents and grandparents from whom I inherited my love of learning and my drive to further my education. I would also like to thank my siblings who each have supported and uplifted me in numerous ways throughout this process.

Acknowledgements

To begin with, I would like to thank my advisor, Neil, who taught me early on that graduate school is a marathon, not a sprint, and who has run with me through the past five years. I greatly appreciated both your enthusiasm for our work and your sincere mentorship that always showed that you also cared about me and my success.

I would also like to thank each of my committee members, each of whom I have brought distinct and valuable insights to this work. I would particularly like to thank Jeff for years of insightful collaboration and mentorship. I would also like to thank Katsuyo for her collaboration and astute feedback. I would also like to thank those from the Sakamoto and Thornton groups who I have had the opportunity to collaborate with, especially Regina Garcia-Mendez, Bryan Kinzer, Vishwas Goel, and Asma Sharafi.

I would also like to thank all of the members of the Dasgupta group for the numerous things I have learned from my interactions with each one of you. In particular, I would like to thank Eric Kazyak, who has been a close mentor and friend ever since I first moved to Michigan, and who I have worked closely with throughout my time here. I would also like to thank others in the battery subgroup, each of whom I have worked closely with.

I am also grateful for the funding and technical support that supported this work including: the National Science Foundation Graduate Research Fellowship (Grant DGE1256260), the Ford-University of Michigan Alliance Program, the Bosch Energy Research Network (BERN), the University of Michigan College of Engineering, and the Michigan Center for Materials Characterization.

Lastly, I would like to thank everyone else who has supported me both professionally and personally and made my time at Michigan such a great experience.

Table of Contents

Acknowledgements iii

List of Figures vii

Abstract xvi

Chapter 1 Introduction 1

Motivation 1
Outline 3
Individual and Group Research Statement 4

Chapter 2 Background 6

Li-Ion Batteries and the Impetus for Increasing Energy Density 6
Promise and Chalenges of Li Metal Anodes 7
Solid State Batteries 8
Solid Electrolytes - Ionic conductivity 10
Solid Electrolytes - Electrochemical Stability 11
Solid Electrolytes – Mechanical Properties 13
Promising Solid Electrolytes 14
Composite Electrodes 15
Multi-Modal Analysis 17
Operando Video Microscopy 17
Operando X-ray Photoelectron Spectroscopy (XPS) 19

Chapter 3 Understanding SEI formation and Improving Interface Stability with Atomic Layer Deposition 21

Results and Discussion 24

Li-Li Symmetric Cells 24
Operando X-ray Photoelectron Spectroscopy 30
Operando optical visualization 38
Conclusions 43
Experimental Section 44
Preparation of LGPS State Electrolyte 44
Li-Li Symmetric Cell Assembly 45
LTO Pre-lithiation 45
LTO Anode-free Cell Assembly 46
ALD Al_2O_3 Surface Coating of LGPS Pellets 46
Electrochemical Characterization 47
SEM and Optical Microscopy 47
Optical Visualization Cell 48
Operand Photoelectron Spectroscopy (op-XPS) 48
Auger Electron Spectroscopy 48
Chapter 4 Interphase Dynamics in Anode-Free Solid-State Batteries 49
Experimental Section 51
Preparation of Solid Electrolyte 51
Li/SE/Cu Half Cell for Electrochemical Analysis (Figure 4.2A) 52
LTO/SE/Mo Half Cell for *Operando* Video Microscopy (Figure 4.2B) 55
LTO/SE Half Cell for *Operando* XPS (Figure 4.2C) 56
Results and Discussion 57
Bulk Electrochemistry 57
Operando Video Microscopy 61
Operando X-Ray Photoelectron Spectroscopy 63
Conclusion 69
Chapter 5 The Effects of the Physical Properties of Li on the Critical Current Density 70
Results and Discussion 73
Synchronized Electrochemical Testing and *Operando* In-plane Li|LLZO|Li Cell Analysis 73
Derivation of Solid Li Pseudo-Viscosity 80
Comparison of Viscosity and Diffusivity vs. Critical Current Density Across the Melting Point of Li 82
Conclusions 83

Experimental Procedures 84
LLZO Synthesis and Pre-Conditioning 84
O*perando* Optical Li Cycling Cell 84
Chapter 6 Rate Limitations in Composite Solid-State Battery Electrodes 87
Chapter 7 Conclusions and Future Work 113
Conclusions 113
Future Work 115
Bibliography 117

List of Figures

Figure 1.1. Global fossil fuel consumption by type from 1800 to 2019. 1

Figure 1.2. Electric vehicle sales over time. 2

Figure 2.1. Schematic showing the components of a Li-ion battery. 7

Figure 2.2. Schematic showing dendrite formation leading to dead Li accumulation. 8

Figure 2.3. History of solid-state electrolyte development. 9

Figure 2.4. Ionic conductivities of various solid electrolytes. 11

Figure 2.5. Electrochemical stability window of common Li compounds (orange) and solid electrolytes (green). Sulfide label has been added for convenience. 12

Figure 2.6. *Operando* video microscopy images showing Li penetration in LLZO..... 13

Figure 2.7. Summary of solid electrolyte properties..... 15

Figure 2.8. Schematic and SEM image of a solid-state composite electrode. 16

Figure 2.9. Schematics showing *operando* video microscopy setups for (A) plan-view, (B) angled, and (C) cross-section observation. 17

Figure 2.10. Still frames from *operando* video showing synchronization of the video and the voltage trace. 18

Figure 2.11. Schematic showing setup and spectra for *operando* XPS 19

Figure 3.1. FIB-SEM cross section of the ALD coated LGPS surface. The ALD conformally coats the LGPS. Growth rates measured by SEM match those measured by elipsometry on adjacent Si samples. Pt was deposited in the SEM to achieve a clean cross section of the ALD. 24

Figure 3.2. (a) Schematic of uncoated and ALD coated Li-Li symmetric cells. (b) Nyquist plot of the uncoated and ALD coated samples immediately after assembly. All EIS was performed at 26 °C. (c,d) EIS measurements of impedance over several time scales in both the coated and uncoated samples. e) Voltage traces of uncoated and ALD-coated Li-Li symmetric cells during cycling. During each half cycle 0.1 mAh/cm^2 (~0.44 μm) of Li was plated at a constant current of 0.1 mA/cm^2. Comparisons between early and late cycle voltage traces are shown in Figure 3.5a..... 25

Figure 3.3. Optical and SEM images of the LGPS surface. (a) the LGPS surface before contact with Li metal. Images of the uncoated LGPS interface are shown after contact with Li metal for (b,g) 1 hr and (c,h) 10 hr. Images of the ALD coated LGPS surface are shown after contact with Li metal for (d,i) 1 hr and (e,j) 10 hrs. 27

Figure 3.4. Comparison of XPS measurements for uncoated (black) and ALD coated (red) LTO/LGPS anode-free cells. (a,f) Schematic showing uncoated and ALD coated anode-free cells. XPS spectra of the S 2p and O 1s peaks were acquired with and without bias at t = 0 hrs (initial) and t = 12 hrs (final). The S 2p spectra at t = 0 hrs (b,g) and t = 12 hrs (d,i) correspond to LGPS and Li_2S respectively. The O 1s spectra in the ALD coated sample at t = 0 hrs (h) and t = 12 hrs (j) correspond to the Al_2O_3 film and Li_xAl_yO layer respectively. The O 1s spectra in the uncoated sample at (c,e) correspond to impurities..... 31

Figure 3.5**.** (a) Voltage profiles of uncoated and ALD coated Li-Li symmetric cells at 8 hrs and 68 hrs of cycling. (b) LTO/LGPS/LTO symmetric cell charging cycles with a current density of 0.02 mA/cm^2. Little change is observed after formation cycles (8 hrs after start of cycling) and after significant cycling (after 68 hrs of cycling)..... 33

Figure 3.6. Spectra from opXPS at the LPGS surface for the Li 1s, Al 2p, S 2p, Ge 2p, P 2p, and O 1s peaks. Data is plotted such that spectra of high intensity appear white. 35
Figure 3.7. AES spectrograph of ALD coated LGPS surface after opXPS experiments. The lithiated ALD film has cracked and Li metal has plated in the cracks. 36
Figure 3.8. Timeline and schematics showing evolution of the LGPS surface during opXPS experiments. (a) The Uncoated sample shows rapid reduction of the LGPS into Li_2S, Li_xP and Li_xGe. After ~6 hr, Li_2O begins forming at the surface. Li metal plating is not observed even after 12 hr. (b) The ALD coated sample shows the lithiation of the Al_2O_3 layer into Li_xAl_yO which leads to cracking of the ALD film. As the cracking occurs, the LGPS begins to be reduced and by ~7 hr Li metal begins plating out in the cracks. ΔBE is the change in binding energy observed in the XPS spectra. 37
Figure 3.9. *Operando* optical microscopy of LTO/LGPS/Mo anode-free cells. (a) and (b) show schematics of the anode-free cells in the uncoated and ALD coated cases respectively. (e,f) Before charging in both the uncoated and ALD coated samples, the circular Mo current collector is visible on the surface of the LGPS. (c,d) FIB-SEM cross-sectional images show clean interfaces between the Mo and the LGPS, with the ALD film visible at the interface of the ALD coated sample. (g) In the uncoated sample, after 10 hr charging at 0.01 mA/cm^2 visible darkening occurs across the surface of the current collector as the LGPS under the Mo is reduced. (i) After charging, cross-sectional FIB-SEM confirms reduction across the entire LGPS/Mo interface. (h) In contrast, after only 2 hrs of charging at 0.01 mA/cm^2, the ALD coated sample shows Li metal deposition in several hotspots with other regions of the ALD sample showing no visible LGPS reduction. (j) Cross-sectional FIB-SEM confirms that away from hotspots there is little evidence of LGPS reduction or Li metal plating. (i) Cross-sectional FIB-SEM at the hotspots shows Li

metal and reduced LGPS underneath cracks in the Mo. Additional Li-metal is visible on the surface after having extruded through cracks in the ALD/Mo bilayer. (l) Voltage profile of LTO/LGPS/Mo anode-free cells at varying current densities. 39

Figure 3.10**.** (a) Extended voltage trace of 0.01 mA/cm^2 uncoated half cell shown in Figure 3.9. Even after 23 hr the cell has not reached 1.53 V (the Li/LTO OCV potential). (b) Voltage traces from Figure 3.9l plotted with respect to charge passed. At higher current densities Li metal plating occurs with less total charge passed. 41

Figure 3.11. Final lithiation cycle and following OCV rest of LTO electrode in liquid electrolyte coin cell. 45

Figure 3.12. Optical microscopy of ALD coated LGPS surfaces with different numbers of ALD cycles after 1 hr of contact with Li. 200 cycles of Al_2O_3 showed significantly better stabilization than 20 cycles. 47

Figure 4.1. Nyquist plot of Mo/SE/Mo cells. Ionic conductivity measurements of LGPS and LPSCl after cold pressing. 52

Figure 4.2. Cell configurations. In each configuration Li is plated from the counter electrode up to the anode-free surface at the top of the cell. A) bulk cell with a Cu foil current collector at the anode-free interface. When studying the anode-free interface in LGPS, a thin layer of LPSCl was added at the Li counter electrode interface. B) Operando video microscopy cell with a sputtered Mo current collector at the anode-free interface. C) Operando XPS cell using an electron gun as a virtual electrode. 53

Figure 4.3. Li-Li symmetric cell cycling. A) LGPS and LPSCl stability during cycling. For each cell, 0.1 mAh/cm^2 was cycled at 0.1 mA/cm^2. The LPSCl sample exhibits stable cycling throughout the experiment, indicating minimal SEI growth. In contrast, the LGPS sample shows

a continuing increase in cell impedance throughout cycling. B) Overlay of the 1st and 50th cycle in LPSCl showing negligible evolution in the voltage trace..... 54
Figure 4.4. Bulk cell voltage traces. A) Full voltage traces. B) Zoomed in view. In the LPSCl cell the voltage rapidly drops below 0 V, indicating Li plating. In the LGPS the voltage never reaches 0 V..... 58
Figure 4.5. Bulk anode free cell cycling at different rates. Voltage traces of LGPS and LPSCl Li/SE/Cu cells at 10 and 100 μA/cm^2. The trend showing increased SEI formation in the LGPS sample is consistent at both current densities. 59
Figure 4.6. Cyclic Voltammetry on bulk anode free cells. (LPSCl) As the voltage is decreased from the OCV (1.75 V), only a slight negative current is obverved above 0 V, indicating only minimal SEI formation. Past 0 V, a significant current is observed due to Li plating. As the sweep direction is reversed, the current switches direction as soon as 0 V is passed indicating the plated Li metal is being stripped. After all Li is stripped, the current drops back close to 0. (LGPS) As the voltage decreases below 0.8 V, the LGPS sample shows significant current corresponding to SEI formation which continues throughout the scan. As the scan direction is reversed, the current remains negative implying continued SEI formation and no reverse current to indicate stripping of Li metal..... 60
Figure 4.7. Bulk cell optical microscopy. Optical microscopy of the SE and Cu surfaces after the first half cycle. In the LPSCl sample, minimal SEI is observed and Li deposits are visible on both surfaces. In the LGPS sample, both surfaces have significant SEI byproducts and mechanical degradation. No Li is visible on the surface. 61
Figure 4.8. Operando video microscopy images and voltage traces. A) Top-down microscope images of the circular Mo current collector on the SE both before and after plating. After images

show SEI formation in both samples, however, Li whiskers are only visible on the LPSCl sample. B) Sample voltage traces confirming that only the LPSCl sample goes below the Li/Li^+ potential and begins plating Li. In the video, Li whisker nucleation is confirmed to occur when voltage drops below the Li/Li^+ potential. 62

Figure 4.9. Operando XPS core scans and corresponding optical microscopy. A-D and E-H) Core scans throughout the experiment for the LPSCl and LGPS samples respectively, with each scan corresponding to an addition 6 min. of charging. I-K and L-N) Corresponding optical images of anode-free surface throughout experiment. 64

Figure 4.10. Operando XPS peak fitting. A-D) S 2p, P 2p, Cl 2p, and Li 1s peak fits for LPSCl. E-H) Corresponding peaks for LGPS with Ge replacing Cl. Peaks are shown for 0, 6 and 60 min of plating. 65

Figure 4.11. Li Reaction Pathway**s.** A) Schematic showing possible Li reaction pathways. B-E) Schematic showing differences between SEI composition and the unstabilizing impact of the electronically conducting Li_xGe phase in the LGPS sample. 67

Figure 5.1. Schematic representation of the optical in-plane test setup of molten li current sweep tests. 73

Figure 5.2. Synchronized Electrochemical Testing and *Operando* Visualization of Molten Li on LLZO. Current is swept from 0 to 2000 mA/cm^2 at a rate of (2 $mA/(cm^2 \cdot s)$). From 0 to 550 mA/cm^2 the cell exhibits a linear voltage response (A-B) and the shell layer on the stripping (left) electrode begins to buckle. At 800 mA/cm^2 (C) deviation from voltage linearity is observed and secondary Li droplets appear at the base of the plating electrode. At 2000 mA/cm^2 (D) the secondary Li droplets continue to grow while the cell deviation from voltage linearity is amplified. The full video is included in Video S1. 74

Figure 5.3. FIB-SEM Analysis of Molten Li|LLZO Cell after Current Sweep and Proposed Li Secondary Droplet Mechanism Schematic. (A) FIB-SEM showing site of Li secondary droplet extrusion. (B) FIB-SEM etched area showing Li filling pre-existing porosity leading to a Li secondary droplet surface eruption. The Li secondary droplet was removed before imaging. (C) Schematic of proposed mechanism of filament propagation and secondary droplet formation... 75

Figure 5.4. Critical Current Density (CCD) vs. Temperature for LLZO. The orange circle represents the current sweep molten Li CCD with standard deviation shown for results of this paper at 195 °C. Solid Li reference data and trend lines come from Wang et al.,[113] Sharafi et al.,[124] and Tsai et al.[103] 77

Figure 5.5. Solid Li Filament Propagation for Optical Current Sweeps. Solid Li current sweep at 170 ℃ for Ta-LLZO (Plating from left to right). Subsurface propagation dominates due to the mechanical properties of solid Li..... 79

Figure 5.6. Viscosity vs. Strain Rate and Li^0 Diffusivity of both Solid and Molten Li. Viscosity versus diffusivity of Li as a function of temperature across the melting point of Li. Since the exact strain rate is unknown it is presented as a range. 82

Figure 6.1. (A-C) Plan-view (top-down) and (D-F) FIB cross-sectional SEM images of graphite/LPSCl composite electrodes with varying graphite/SE ratios. The dark regions are graphite, and the bright regions are LPSCl. 91

Figure 6.2. Electronic and ionic conductivity measurements of graphite composite electrodes with different graphite ratios and temperatures. 92

Figure 6.3. (A) Accessible capacities at increasing lithiation rates for various graphite/SE ratios. Sample loadings are 1.87 mAh/cm^2. (B-E) Corresponding lithiation voltage traces for each graphite ratio. 94

Figure 6.4. (A) Accessible capacity during the CC portion of the lithiation of the 1.87 mAh/cm^2 cells from figure 2 in the main text. (B) CCCV lithiation capacities normalized by the mass of the composite electrode. 95
Figure 6.5. (A) Delithiation capacities for 1.87 mAh/cm^2 cells from Figure 2 in the main text. All delithiation cycles were performed at C/8 but are plotted under the C-rate of their corresponding lithiation step. Some coulombic inefficiency is apparent in the early cycles of the 40% and 60% Gr samples due to continued SEI formation. (B) Corresponding voltage traces for each graphite ratio and C-rate. Again, voltage traces are labeled with the c-rate of their corresponding lithiation step. Delithiation voltage traces have also been normalized to lithiation capacity achieved in the lithiation step to allow for a more direct comparison. 96
Figure 6.6. (A) Top town ex-situ images of graphite composite electrodes showing color changes in the graphite phase throughout lithiation. Electrodes were lithiated at C/32 to various SOC. Electrode areal capacities are 1.87 mAh/cm^2 with a graphite fraction of 46%. (B) Schematic showing custom cell for *operando* visualization of composite electrode cross. (C) Zoomed out view showing Li/graphite half cell assembled in the visualization platform..... 98
Figure 6.7. (A-F) Time series showing zoomed in microscope images of 40% Gr composite electrode at different states of charge during C/4 lithiation. Full videos for 40-80% Gr are included in the Supporting Information. (G-H) Schematics showing transport limitations due to ion conduction within the SE (G) and Li diffusion within the graphite (H). 100
Figure 6.8. Time series showing zoomed in microscope images of 40% Gr composite electrode at different states of charge during C/4 delithiation. 101
Figure 6.9. (A-F) Cross section snapshots at C/16 (top row) and C/4 (bottom row) rates, taken after 16 hr and 4 hr of lithiation respectively. Composite electrodes are shown with various

graphite ratios (40%-80% Gr) and an areal capacity of 4 mAh/cm^2. To normalize the field of view for the different graphite ratios, the magnification is increased as graphite loading increases. 102

Figure 6.10. Cross section snapshots at 16 hr (C/16 lithiation) and 4 hr (C/4 lithiation) for composite electrodes with various graphite ratios (40%-60% Gr) and an areal capacity of 1.87 mAh/cm^2. To normalize the field of view for the different graphite ratios, the magnification is increased as graphite loading increases. 103

Figure 6.11. (A-E) Evolution of local Li site fraction in the 40% Gr electrode during C/4 charging at different SOCs. (F) Local SE potential in the electrode. 106

Figure 6.12. Simulation results for a κ value ~11 times higher than the nominal value, conducted to examine the effect of ionic conductivity in SE. (A-E) Evolution of local Li site fraction in the 40% Gr electrode during C/4 charging at different SOCs. (F) Local SE potential in the electrode. 107

Figure 6.13. Simulation results for a DGr value 10 times higher than the nominal value, conducted to examine the effect of Li diffusivity in the active material. (A-E) Evolution of local Li site fraction in the 40% Gr electrode during C/4 charging at different SOCs. (F) Local SE potential in the electrode. 108

Figure 6.14. (A-E) Evolution of local Li site fraction in the 40% Gr electrode during C/16 charging at different SOCs. (F) Local SE potential in the electrode. 109

Abstract

Expanding our capacity for energy storage is vital to the worldwide push to address climate change by transitioning to renewable energy. Improving battery technologies by increasing energy density, cycle life, charge rates, and safety will accelerate this change. Solid-state batteries (SSBs) are a promising technology for step improvements in each of these areas. Despite marked progress over the past decade, significant hurdles still need to be overcome to enable the widespread commercialization of SSBs.

The primary goal of this thesis is to gain a more fundamental understanding of the electro-chemo-mechanical phenomena that govern SSB performance. By improving our understanding of these underlying mechanisms, we can more efficiently design battery systems that address each of these challenges. In this thesis, *operando* techniques are used to examine model systems to elucidate the mechanisms that both limit (1) cycle life and (2) charge rates.

Cycle life in Li batteries is largely limited by undesirable side reactions and/or structural changes that both consume the Li reservoir and degrade the performance of the electrodes and electrolytes. This is especially detrimental in Li metal batteries, where the Li anode is highly reactive. The first section of this thesis aims to understand undesirable reactions that occur at the Li metal/solid electrolyte (SE) interface in SSBs. Specifically, the role of interfacial chemistry is investigated by both changing the SE used and adding interlayers between the Li and SE. It is observed that adjusting the interfacial chemistry can limit the impact of these side reactions. *Operando* video microscopy and *operando* x-ray photoelectron spectroscopy are used to

investigate the time-dependent interplay between interfacial chemistry and morphology. Distinct differences in the chemical evolution are observed between SEs that form stable interlayers after reacting with Li metal and those that continue to react, leading to battery failure. Additionally, design rules are established for artificial interlayers used to stabilize the Li/SE interface.

Increasing charge rates in SSBs requires improvement in both the Li metal anode, where high current densities can lead to short-circuiting, and in composite electrodes, where slow Li transport into the depth of the electrode hinders fast charging. The second aim of this thesis probes both the mechanical properties that lead to Li penetration of the SE (short-circuiting) and the electrode properties that slow down Li transport. By synchronizing *operando* video microscopy with cycling data of both Li electrodes and composite electrodes, the microscale impact of fast charging is observed and correlated to signatures in the voltage traces. Molten Li electrodes are used as a model system to show that the mechanical properties of Li play a crucial role in cell shorting. Graphite composite electrodes are used to observe heterogeneous lithiation of the electrode caused by Li transport limitations in both the SE and active material phases.

In summary, this thesis improves our understanding of the mechanisms that limit both cycle life and charge rates in SSBs. Design rules based on these insights are given that can aid in the development of SSBs that last longer and can charge faster.

Chapter 1

Introduction

Motivation

Over the past century, technological innovation has transformed nearly every aspect of society, from how we eat to how we travel. Fossil fuels have been a fundamental part this transformation by providing the energy required for each of these activities (Figure 1.1).[1] As industrialization

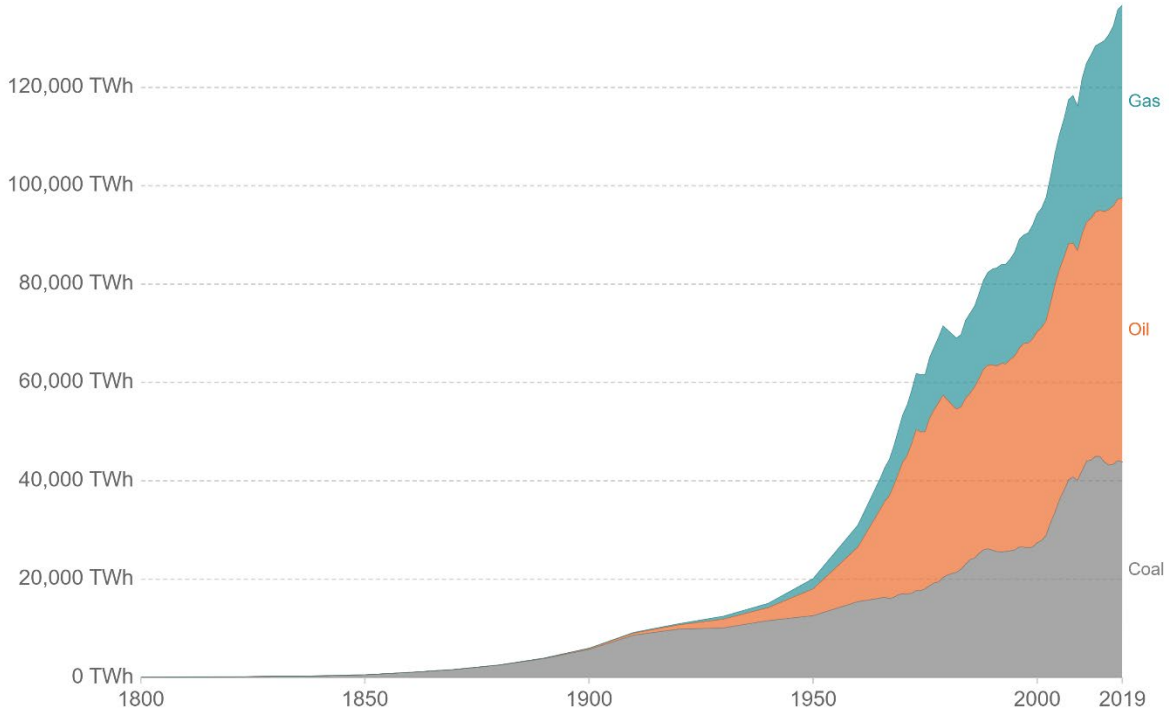

Figure 1.1. Global fossil fuel consumption by type from 1800 to 2019.[1]

continues and expands around the world, the demand for cheap energy will only continue to increase. Despite the numerous improvements enabled by this transition, it comes at a substantial cost. High levels of CO_2 and other greenhouse gasses emitted from the use of fossil fuels have begun to change the global climate at an alarming rate, and this is only expected to continue as long as we continue to consume fossil fuels.

Eliminating our reliance on fossil fuels while simultaneously allowing continued industrialization worldwide has become one of the defining challenges of our time. To address this, our rapid transition to renewable energy sources is imperative. A critical component of this transition is cheap, reliable methods of storing and transporting energy derived from these sources.

In the past few decades, Li-ion batteries (LIBs) have transformed energy storage and enabled the era of personal electronics. As LIB costs have plummeted in the past several years, their use has expanded into grid-scale storage projects and electric vehicles, with electric vehicle sales increasing exponentially. They are now expected to transform the automotive sector in the

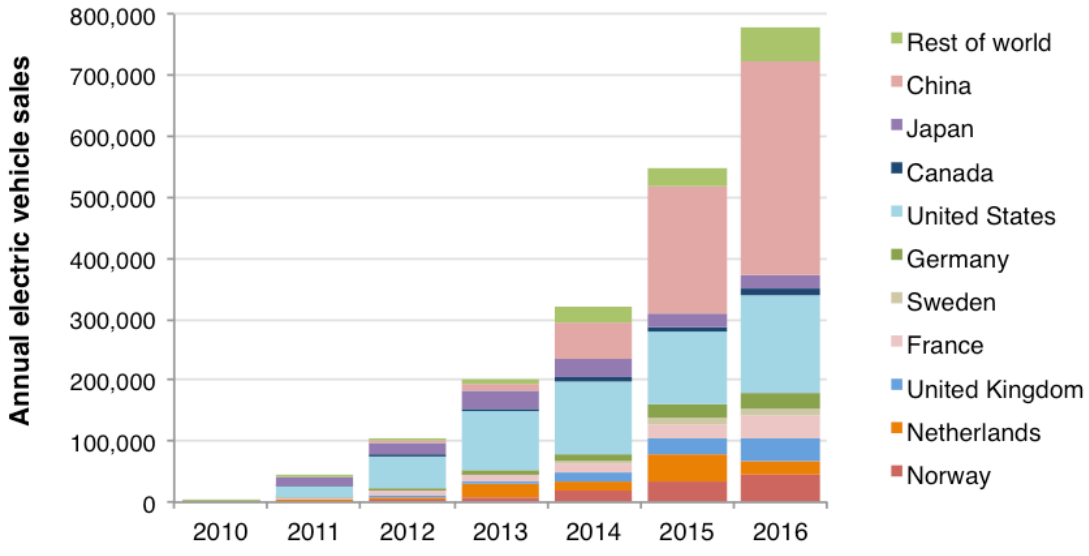

Figure 1.2. Electric vehicle sales over time.[3]

coming decade. Further progress in batteries will allow their prices to drop even farther to enable electric vehicles to be cost competitive with internal combustion engine vehicles (Figure 1.2).[2,3]

SSBs are promising technology to simultaneously increase battery safety while decreasing cost by enabling higher energy density materials.[4] Despite early promising results, the disparate mechanisms that govern performance in SSBs vs. LIB are not fully understood. The overarching goal of this thesis is to probe the complex interplay between the electro-chemo-mechanical phenomena that control the evolution of multiple crucial interfaces, and by understanding these mechanisms increase our ability to rationally design SSBs with high capacities, long cycle lives, and low cost.

Outline

Chapter 2 provides background knowledge on the basics of LIBs and SSBs with particular attention paid to the basic physics that govern SSBs, including Li transport and the electro-chemo-mechanical phenomena that govern SSB interface evolution and performance. Additionally, background will be provided on many of the characterization and manufacturing techniques used throughout the remainder of the thesis.

Chapter 3 through 5 explore the electro-chemo-mechanical evolution of Li/SE interfaces. Chapter 3 probes the time-dependent degradation of Li/SE interfaces and explores the impact and evolution of interlayers used to stabilize the interface. Chapter 4 investigates the impact on interface stability of SE chemistry and illustrates the impact of electrochemical stability on anode free battery performance. Chapter 5 focuses on a molten Li model system used to probe the role that mechanical properties of both the Li metal and the SE play on filament formation and cell failure.

Chapter 6 investigates the phenomena that govern power/energy density tradeoffs in composite electrodes, using graphite as a model system. The effects of the electrode microstructure and the properties of both the SE and the active material on the severity of rate limitations are also explored.

Chapter 7 concludes this thesis by summarizing the key findings and the overall impact on the field, as well as presenting directions for future work.

Individual and Group Research Statement

The research in this dissertation represents not only my own work, but also significant effort from many of my collaborators and co-authors. Below is a summary of the individual contributions to the work presented here.

Chapter 3 is adapted from Davis et al.[5] Andrew L. Davis prepared the samples and performed the electrochemical measurements and the optical microscopy. Regina Garcia-Mendez developed the sample fabrication protocol. Kevin N. Wood and Glenn Teeter developed the *operando* XPS method and performed both the *operando* XPS and the Auger experiments. Eric Kazyak helped with the ALD processing and data analysis. Kuan-Hung Chen prepared and lithiated the LTO electrodes. Neil P. Dasgupta and Jeff Sakamoto supervised the research and assisted with manuscript preparation and revision.

Chapter 4 is adapted from Davis et al.[6] Andrew L. Davis and Daniel W. Liao prepared the samples and ran the bulk electrochemical experiments. Andrew L. Davis also performed *operando* and *ex situ* optical microscopy and corresponding data analysis. Eric Kazyak performed the *operando* XPS experiments. Kevin N. Wood developed the *operando* XPS

method and advised on the *operando* XPS experimental setup. Neil P. Dasgupta supervised the research and assisted with manuscript preparation and revision.

Chapter 5 is adapted from Kinzer et al.[7] Bryan Kinzer prepared the LLZO samples for optical analysis. Andrew L. Davis developed the molten Li experimental setup. Bryan Kinzer and Andrew L. Davis performed the *operando* optical imaging and data analysis. Thorben Krauskopf and Hannah Hartmann prepared samples for and performed *operando* SEM experiments and analysis. Will S. LePage assisted with mechanical property theory and calculations. Eric Kazyak assisted with *ex situ* SEM and *operando* optical imaging setup development. Jeff Sakamoto and Neil P. Dasgupta supervised the research and assisted with manuscript preparation and revision.

Chapter 6 is adapted from Davis et al.[8] Andrew L. Davis, Daniel W. Liao, Mark N. Main, and John Lee prepared the samples and ran the bulk electrochemical experiments. Andrew L. Davis developed the *operando* video microscopy setup and performed *operando* experiments. Vishwas Goel constructed the electrochemical dynamics model. Eric Kazyak performed FIB-SEM and advised on operando setup development. Neil P. Dasgupta and Katsuyo Thornton supervised the research and assisted with manuscript preparation and revision.

Chapter 2

Background

Li-Ion Batteries and the Impetus for Increasing Energy Density

Since their commercialization 30 years ago, LIBs have transformed many aspects of modern life by enabling high density energy storage. Conventional LIBs consist of three major components: an anode that stores Li^+ in a high energy state, a cathode that stores Li^+ in a low energy state, and an electrolyte which allows Li^+ transport between the two (Figure 2.1).[9] Traditionally, graphite anodes and $LiCoO_2$ (LCO) cathodes are used. Compared to their predecessors, each of these are significantly higher energy density materials, which has allowed for the compact energy storage required for personal electronics and early electric vehicles. However, further improvements in energy density would not only be enabling for even smaller or longer lasting electronics, but are also key for decreasing battery cost per kWh to enable widespread adoption of electric vehicles.

As the demand for electric vehicles has skyrocketed in recent years, the push to improve on Li-ion technologies has accelerated. Significant progress in the energy density and cycle life of LIBs has been achieved by moving to higher energy density materials and refining battery charging and manufacturing; however, as we approach the fundamental limits of Li-ion

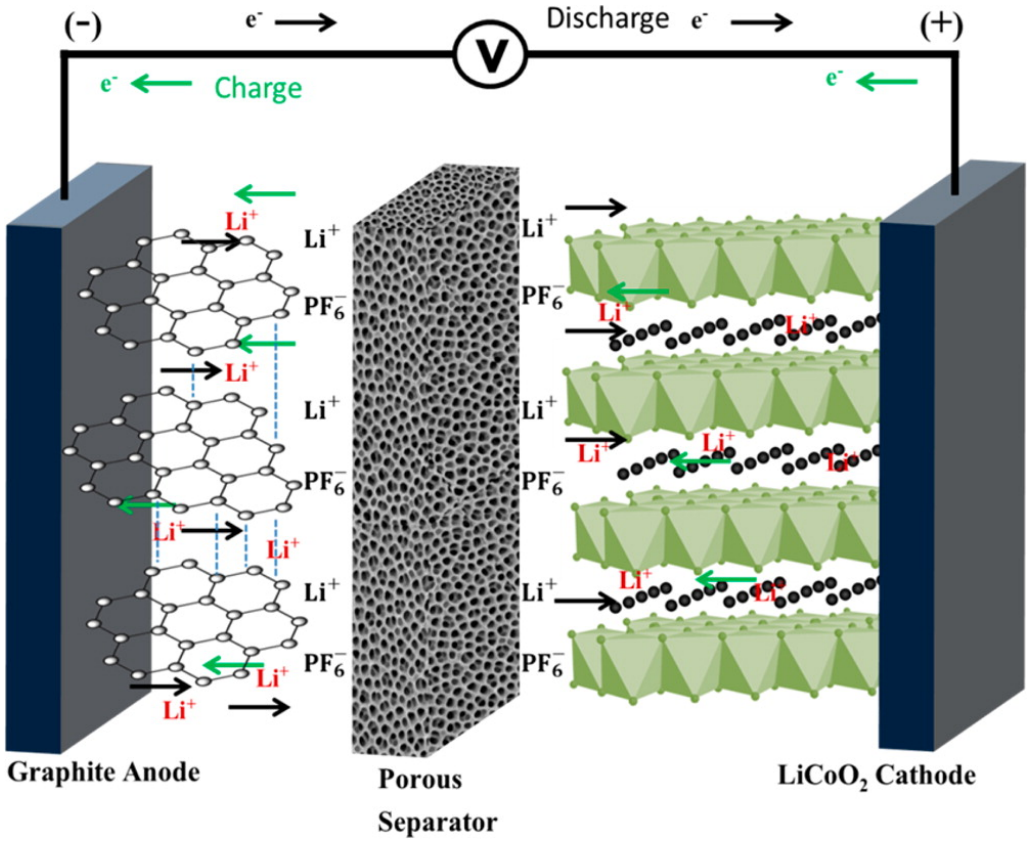

Figure 2.1. Schematic showing the components of a Li-ion battery.[9]

technology, improvements become more and more difficult. This has driven the push for next-generation battery chemistries that promise step increases in battery energy density, safety, and cycle life.[10]

Promise and Chalenges of Li Metal Anodes

Next-generation chemistries look at replacing current anode, cathode and/or separator materials. In particular, Li metal anodes are foundational to many of the next-generation chemistries with high theoretical energy densities.[11,12] Li metal has a high theoretical capacity of 3,860 mAh/g (~10x the capacity of graphite anodes). Despite this high energy density, commercialization of rechargeable batteries based on Li metal remains elusive due to a number of challenges that limit

the safety and cycle life of current Li metal anodes. The high reactivity of Li metal leads to problematic reactions with the electrolyte, forming a solid electrolyte interphase (SEI) that degrades battery performance. Additionally, the unconstrained expansion and contraction of the Li metal anode during cycling leads to dendrite formation, which causes addition SEI formation and dead or inactive Li formation, both of which lead to permanent loss of capacity and an increase in cell polarization (Figure 2.2). Dendrite formation can also cause short circuiting of the cell, causing battery failure.[13,14] Despite significant efforts to address these obstacles, achieving long cycle life with liquid electrolytes has remained elusive.

In contrast to the limited progress achieved with Li metal anodes in liquid electrolytes, long cycle life has been demonstrated in Li metal anodes where liquid electrolyte is replaced with a SE. Preliminary results from a small number of studies investigating Li metal anodes with SEs have shown stable cycling for >1000 cycles.[15,16]

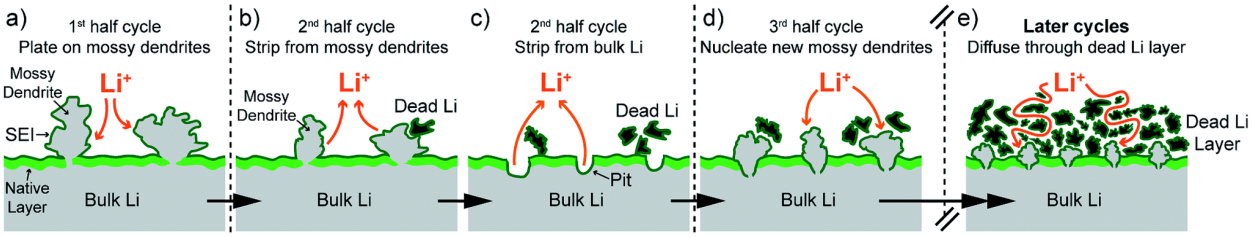

Figure 2.2. Schematic showing dendrite formation leading to dead Li accumulation.[14]

Solid State Batteries

SSBs are a promising system for addressing many of the challenges faced with next-generation chemistries, especially Li metal anodes. SSBs have a similar structure to standard LIBs, but the liquid electrolyte and separator are replaced by a SE. This increases battery safety by removing the flammable liquid electrolyte responsible for battery fires. Additionally, the

mechanical properties of the SE help to constrain the Li metal anode, potentially allowing for extended cycling.

Over the past 50 years, several different classes of SE have been developed.[17–19] As our fundamental understanding of the science behind Li-ion conduction within SEs has improved, successively higher performance SE candidates have been designed. There are a number of properties that govern the performance of SEs. Some of the most critical include ionic conductivity, electrochemical stability, and mechanical properties. The following sections will give an introduction into each of these properties.

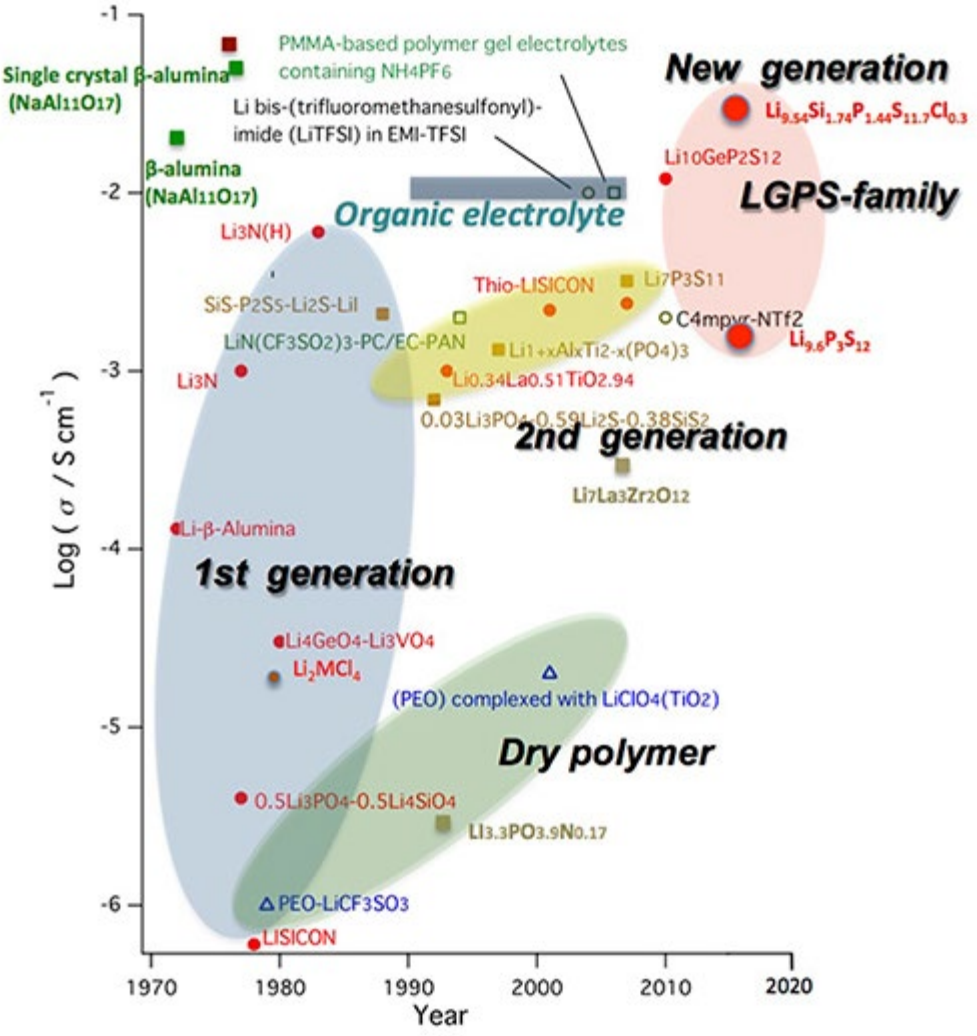

Figure 2.3. History of solid-state electrolyte development.[17]

Solid Electrolytes - Ionic conductivity

Like liquid electrolytes, SE allow for the transport of Li^+ through the material; however, the transport mechanism is distinct. Mass transport is governed by the Nernst-Plank Equation, where the mass flux of Li^+ (J) is given by:

$$J = -\nabla\left[D\,\nabla c + \frac{zF}{RT} D\,c\,\nabla\phi\right]$$

Diffusion Migration

where D is the diffusion coefficient, c is the concentration of mobile Li^+, z is the valence of the ion, F is Faraday's constant, R is the gas constant, T is the temperature, and ϕ is the electric field. There are two terms in the equation: diffusion, which is driven by a concentration gradient, and migration, which is driven by an electric field. In a liquid electrolyte, both the positive and negative ions are mobile, so any electric field applied to the system leads to rapid movement of the ions until no electric field remains. Therefore, the flux of Li^+ is driven almost exclusively by diffusion. In contrast, SEs have a transference number of unity (only the positive ions, Li^+, are mobile), so, due to electrostatic forces, no significant concentration gradients form. Therefore, the flux of Li^+ is driven almost exclusively by migration. For migration, the relationship between the electric field and the flux of Li^+ are proportional to the diffusion coefficient and the concentration. For simplicity, these terms are generally combined into an ionic conductivity.

The ionic conductivity of various SEs is shown in Figure 2.4.[18] The equivalent conductivity of a state-of-the-art liquid electrolyte is indicated by the dashed line at the top. A number of SEs, primarily LISICON-like and Argyrodite sulfide electrolytes, have achieved ionic conductivities comparable to liquid electrolytes.

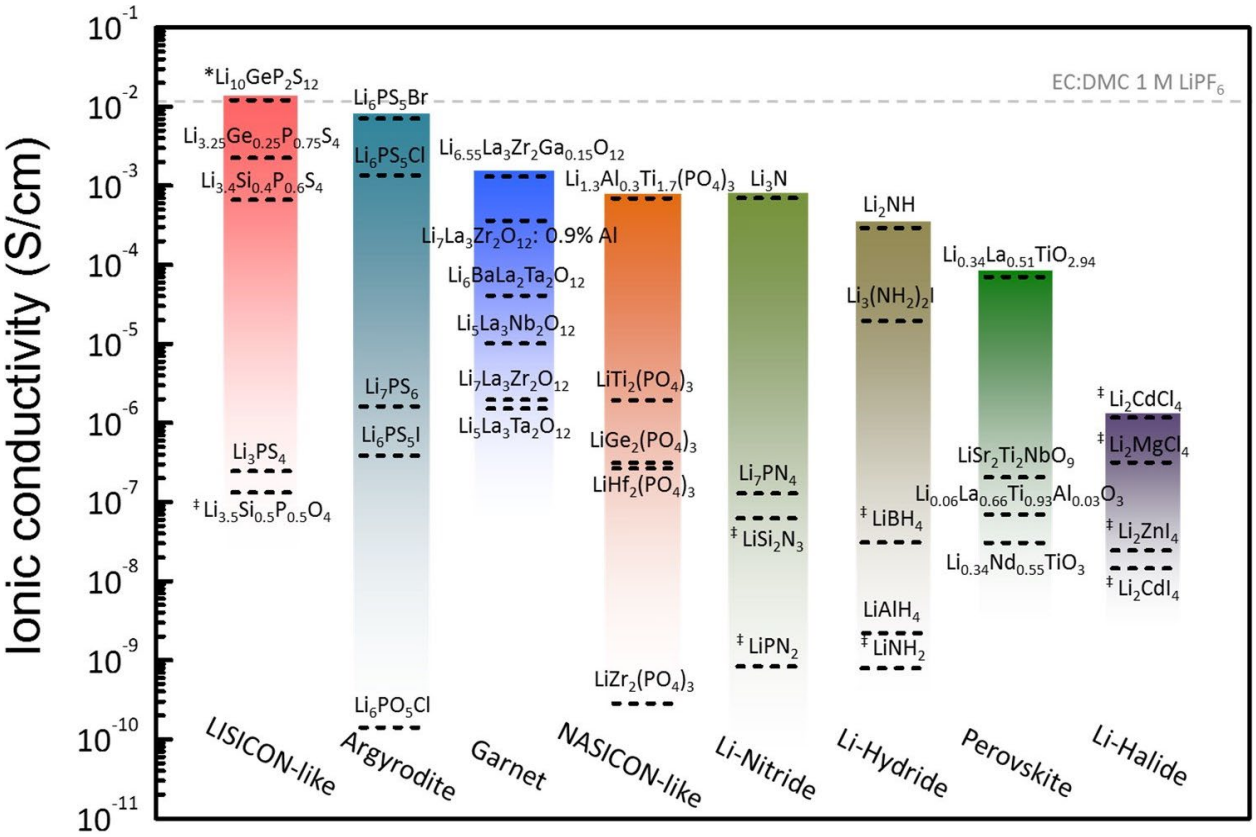

Figure 2.4. Ionic conductivities of various solid electrolytes.[18]

Solid Electrolytes - Electrochemical Stability

Due to the high reactivity of Li metal, many SEs also suffer from SEI formation in a similar way to liquid electrolytes. The thermodynamics governing these reactions can be summarized by the electrochemical stability window. This is the electrochemical window within which the SE will not react. If the electrochemical potential of Li in the adjacent material goes above or below the window bounds, the SE will be respectively reduced (lithiated) or oxidized (delithiated), forming SEI. The electrochemical stability window of a number of common Li compounds (orange) and SE (green) are given in Figure 2.5.[20] It should be noted that Li metal is at 0 V vs. Li/Li^+ and therefore is not stable vs. most SEs, especially the sulfide electrolytes with high ionic

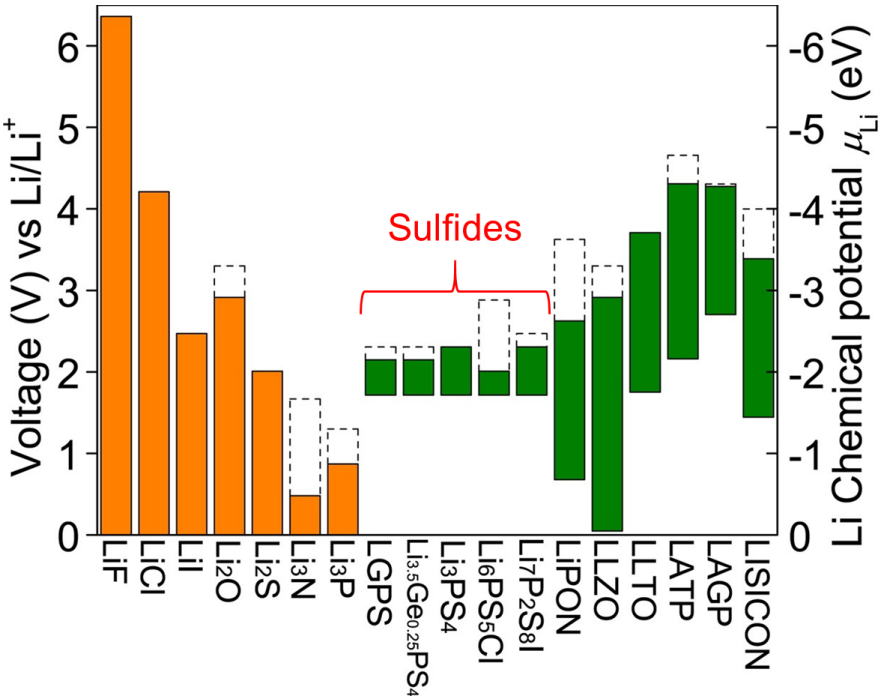

Figure 2.5. Electrochemical stability window of common Li compounds (orange) and solid electrolytes (green).[20] Sulfide label has been added for convenience.

conductivities. $Li_7La_3Zr_2O_{12}$ (LLZO) is one of only SEs that is stable vs. Li metal. In addition to instability many SEs exhibit against Li metal anodes, most of the SEs are also not stable vs. high voltage cathodes (~4-5 V vs. Li/Li^+). This is also a challenge that needs to be addressed, but in this thesis I will focus predominantly on anode materials.

Fortunately, thermodynamics does not tell the whole story of SE electrochemical stability. Thermodynamics indicates whether a reaction is energetically favorable; however, the rate at which the reaction will occur, or whether the reaction will occur at all, are largely dependent on the reaction kinetics. Within the SEs that are thermodynamically unstable, two distinct categories of SE emerge.[20,21] The first category is those which are kinetically unstable and continuously form an SEI, which leads to a thick SEI that increases cell impedance, causing low energy efficiency and eventual cell failure. The second category is those that are kinetically stable, meaning that after a thin SEI layer is formed, the rate of further decomposition is greatly

decreased. This leads to a thin, stable SEI with minimal impact on cell impedance. These differences will be discussed in more detail in Chapter 3.

Solid Electrolytes – Mechanical Properties

The final characteristic of SEs that is important to understand for this thesis is their mechanical properties. During the early development of SEs, it was widely theorized that, in contrast to liquid electrolytes, ceramic SEs would mechanically constrain Li metal, therefore preventing dendrites and dead Li formation. However, subsequent studies have shown that at high charge/discharge rates Li filaments still form and can short circuit the cells, despite the high modulus of SEs (Figure 2.6).[22]

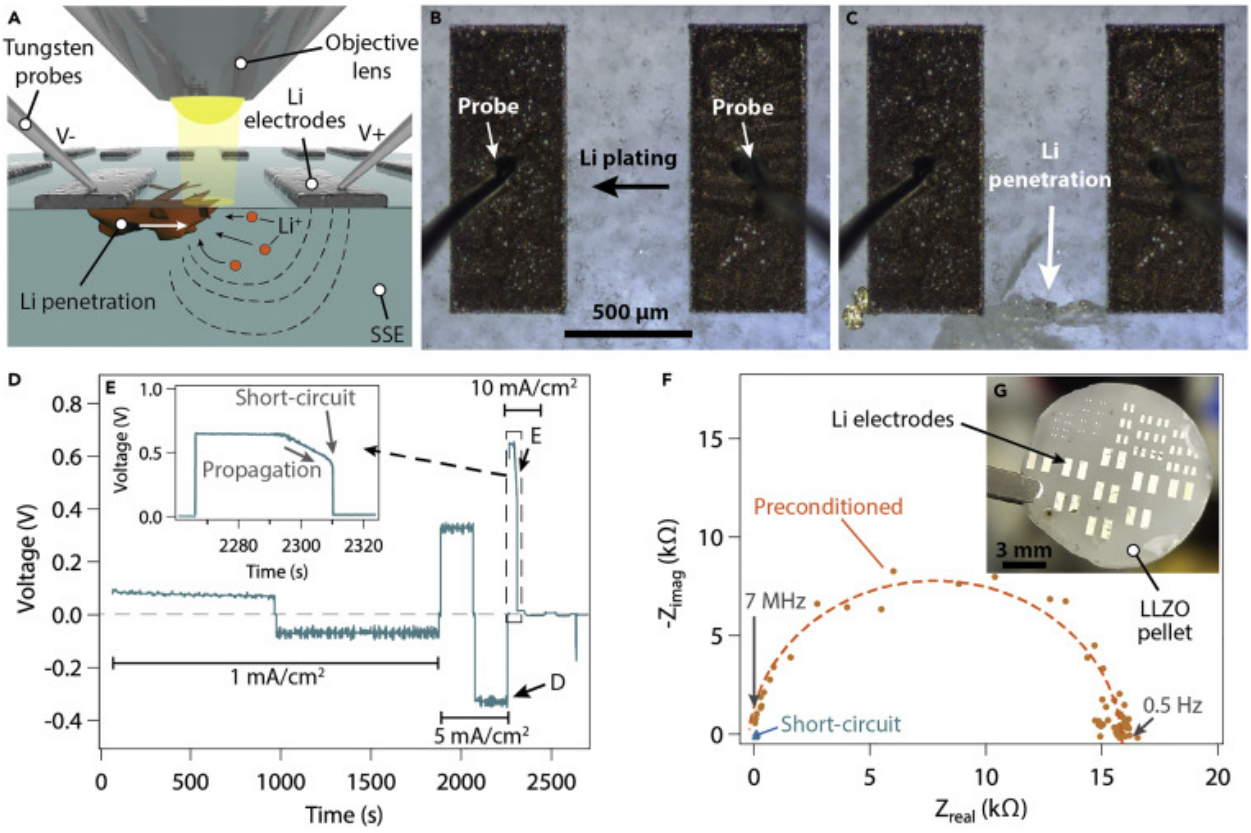

Figure 2.6. *Operando* video microscopy images showing Li penetration in LLZO.[22]

At lower current densities short circuiting has been shown to not occur even over >1000 cycles.[15,16] The current density at which filament nucleation occurs is called the critical current density (CCD). The CCD is dependent on a number of parameters including the mechanical properties of the SE, the amount of charge passed during each cycle, the cell temperature, etc.

Recent efforts have begun to explain the mechanism by which Li metal, a fairly soft material, is able to penetrate hard ceramic SE. Two main mechanisms have been proposed.[23,24] In Mechanism 1, current focusing in defects or surface flaws leads to an increase in localized mechanical stress, which causes SE fracture.[25–29] In Mechanism 2, electronic defects within the SE lead to the internal nucleation of Li metal in the SE.[27,30,31] Further discussion of these mechanisms will be given in Chapter 4.

Additionally, the mechanical properties of SE have a significant impact on SSB manufacturing. Some SEs, such as the sulfides, have comparably low yield strength and can therefore be manufactured at lower temperatures and pressures.[32] In contrast, oxide electrolytes currently require high temperature and pressure manufacturing processes, although lower temperature processes are under investigation.[33]

Promising Solid Electrolytes

A summary of different SE types and their respective properties is given in Figure 2.7.[4] By analyzing these three properties of SEs, several promising candidates emerge. This thesis will focus on three of the most widely studied: $Li_{10}GeP_2S_{12}$ (LGPS), Li_6PS_5Cl (LPSCl), and $Li_7La_3Zr_2O_{12}$ (LLZO). LGPS is sulfide SE and has one of the highest known ionic conductivities (~10 mS/cm), but it is both thermodynamically and kinetically unstable vs. Li metal. LPSCl is a sulfide SE with slightly lower ionic conductivity (~1 mS/cm) and although it is also

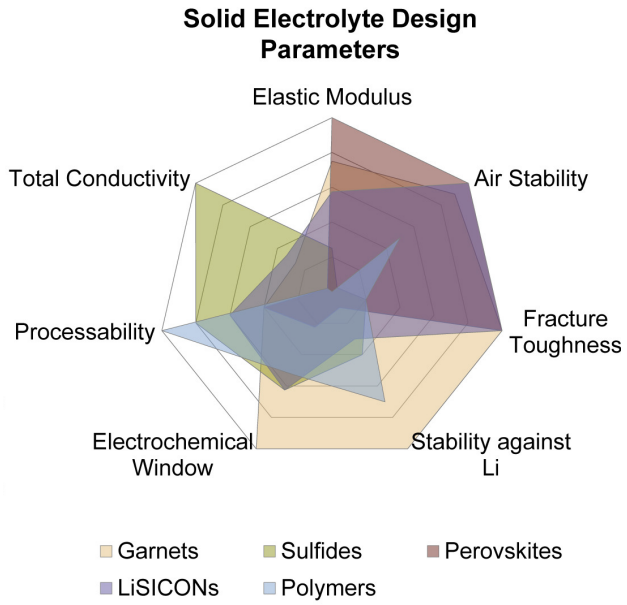

Figure 2.7. Summary of solid electrolyte properties.[4]

thermodynamically unstable vs. Li metal, it is kinetically stable. LLZO is an oxide electrolyte, and although it has lower ionic conductivity (~0.1 mS/cm) it is stable vs. Li metal. Chapter 2 will focus on understanding the instability of LGPS vs. Li metal and challenges and design rules for using interlayers to improve stability. Chapter 3 will focus on the understanding the differences in stability vs. Li metal between LGPS and LPSCl. Chapter 4 will focus on understanding the mechanisms behind Li filament formation in LLZO. Chapter 5 moves away from Li metal and instead focuses on the mechanisms governing Li transport in composite electrodes (described below), using LPSCl and graphite as a model system.

Composite Electrodes

In addition to the SE separator, composite electrodes are another critical component to SSBs. Composite electrodes consist of a blend of SE and active material and somewhat resemble Li-ion

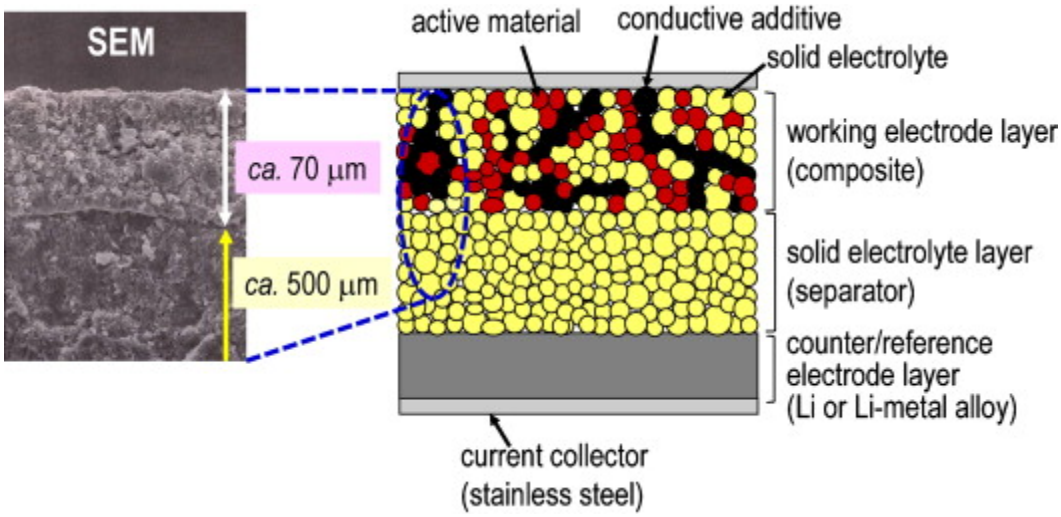

Figure 2.8. Schematic and SEM image of a solid-state composite electrode.[34]

electrodes (Figure 2.8).[34] Composite anodes (e.g., graphite/SE composites) could be used to improve LIB safety. Additionally, enabling composite electrodes is an important challenge for the cathode side of SSBs. The structure of solid-state composite electrodes mirrors many aspects of porous electrodes in liquid electrolyte systems. However, some significant differences exist in the phenomena that govern Li transport through the electrode. In liquid electrolyte systems, the active material particles are easily wetted by the liquid electrolyte, leading to good ionic transport across the entire particle surface. In contrast, in SE systems the electrodes are <100% dense when pressed. Additionally, volume expansion/contraction during cycling can lead to additional porosity within the electrode. This porosity leads to less interfacial contact area between SE and active material particles.[35,36] Another significant difference is the mechanism between Li^+ transport within the electrodes. As discussed above, Li^+ transport in solid-state systems is predominantly due to migration in an electric field because the single-ion conducting nature of SEs prevents concentration gradients from developing. In contrast, in liquid electrolytes, Li^+ transport is dominated by diffusion due to concentration gradients. These concentration gradients result in the strong current inhomogeneity seen in liquid electrolyte systems. Due to this difference, there is

sometimes the perception that current inhomogeneity will be suppressed in SE systems; however, rate limitations in SE based composite electrodes remain.[37,38] Chapter 5 will further discuss the mechanisms behind these rate limitations and give design rules for improving composite electrode rate capability.

Multi-Modal Analysis

This thesis largely focuses on using a multi-modal approach to gain insight into the complex interplay between the electro-chemo-mechanical phenomena that control battery evolution and cycling. In particular, *operando* techniques allow for probing the evolution of battery microstructure, chemistry, and electrochemistry during battery operation. In this thesis, I will regularly reference two main *operando* techniques (*operando* video microscopy and *operando* x-ray photoelectron spectroscopy*)*. The following sections will give an introduction to each of these techniques.

Operando Video Microscopy

One of the techniques that this thesis relies most heavily on is *operando* video microscopy. This technique is adapted from similar techniques developed by the Dasgupta research group for

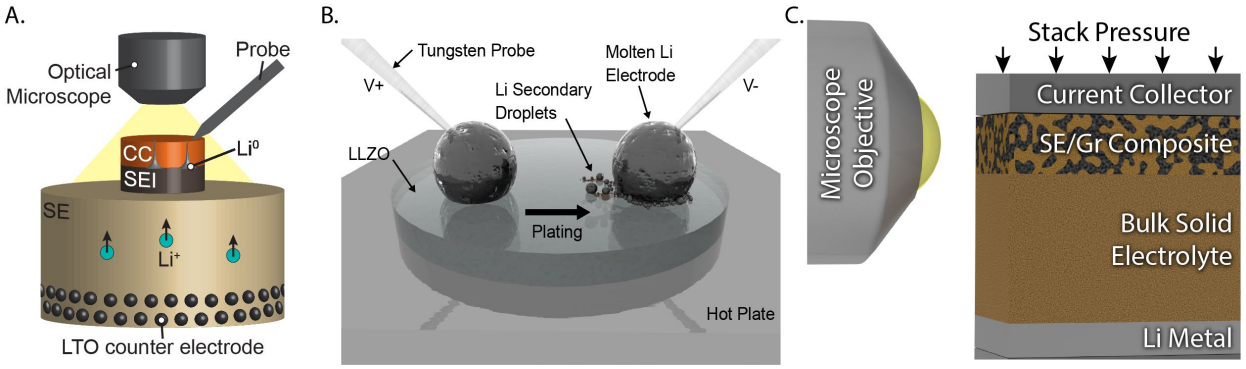

Figure 2.9. Schematics showing *operando* video microscopy setups for (A) plan-view,[6] (B) angled,[7] and (C) cross-section observation.[8]

visualization in liquid electrolyte systems but has been adapted for SE systems.[13,14,39] There are three versions of this platform discussed in this thesis. The first is a plan-view setup, where the electrode is viewed from the top down through a thin sputtered current collector (Figure 2.9A).[6] This setup is used for observing SEI formation and Li plating on the surface of the electrolyte and will be discussed in more detail in Chapters 3 and 4. The second setup allows for an angled view of the sample, which allows for visualization of the regions around bulk molten Li electrodes (Figure 2.9B)[7] and will be discussed in more detail in Chapter 5. The third setup is for observation of the electrode cross-section. This allows for visualization of electrode microstructure and evolution in composite electrolytes (Figure 2.9C)[8] and will be discussed in more detail in Chapter 6.

In addition to facilitating *operando* visualization, these techniques allow for synchronization of the video with the electrochemical voltage traces. This enables correlation of changes observed in the microscope to electrochemical signatures. An example of this is shown in Figure 2.10.

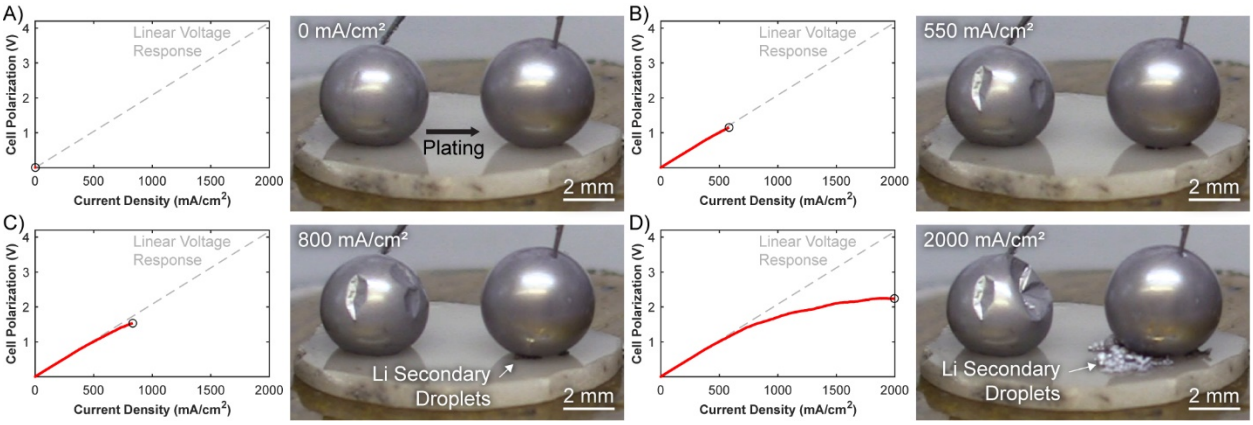

Figure 2.10. Still frames from *operando* video showing synchronization of the video and the voltage trace.[7]

Operando X-ray Photoelectron Spectroscopy (XPS)

In addition to visualization of the electrode through *operando* microscopy, understanding the chemical evolution of the interface is important. *Ex situ* XPS is a commonly used technique for analyzing the composition and binding environment of a surface. XPS is based on the photoelectric effect where the surface is bombarded with x-rays and then the energy of the emitted electrons is measured. By subtracting the energy of the emitted electrons from the original x-ray energy, the electron binding energy can be determined. By comparing the binding energies with those of known compounds, the surface composition can be determined.

Operando XPS was developed by Wood et al. and uses the same technique. However, it is performed on a SE as Li metal is plated out on the surface using an electron gun, which draws

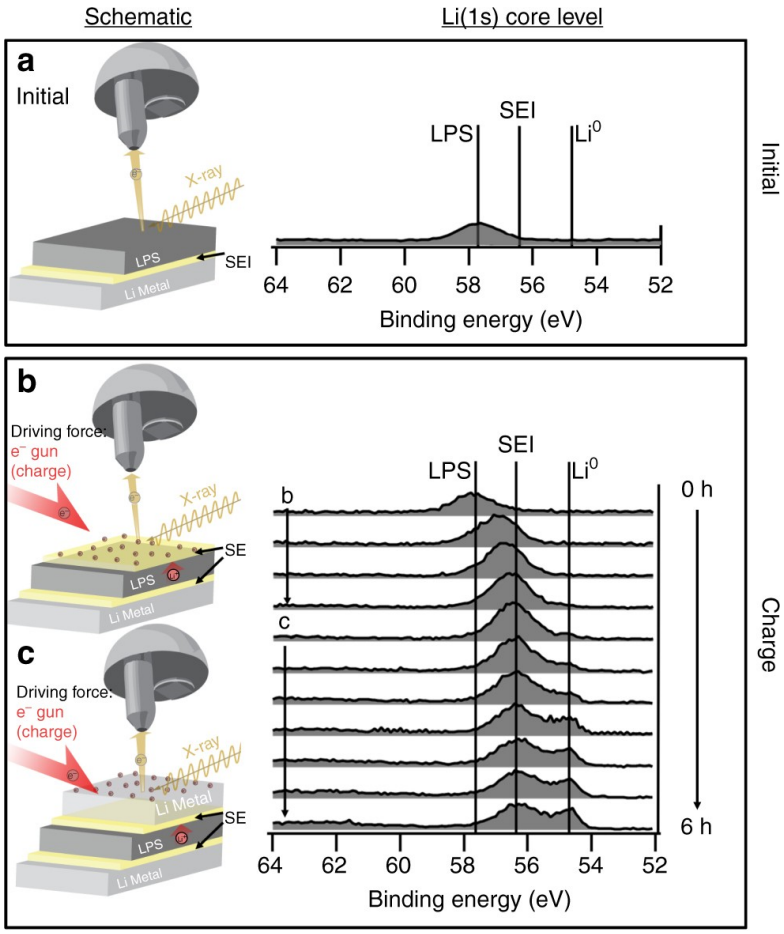

Figure 2.11. Schematic showing setup and spectra for *operando* XPS [40]

Li^+ from the counter electrode up to the electrolyte surface.[40] This allows for chemical analysis of the surface throughout SEI formation and Li plating (Figure 2.11). Further details are given in Wood et al.[40] and in Chapters 3 and 4 of this thesis.

Chapter 3

Understanding SEI formation and Improving Interface Stability with Atomic Layer Deposition

Adapted with permission from Davis, A. L.; Garcia-Mendez, R.; Wood, K. N.; Kazyak, E.; Chen, K.-H.; Teeter, G.; Sakamoto, J.; Dasgupta, N. P. Electro-Chemo-Mechanical Evolution of Sulfide Solid Electrolyte/Li Metal Interfaces: *Operando* Analysis and ALD Interlayer Effects. *Journal of Materials Chemistry A* **2020**, *8* (13), 6291–6302.

As mentioned in Chapter 2, sulfide SE materials have shown particular promise for high performance solid-state batteries because of their high ionic conductivities, which are comparable to or higher than that of liquid electrolytes.[41–44] Previous efforts have shown that sulfide SEs are compatible with room temperature processing and can enable fast charging in full cells.[32,45] Despite this promise, sulfide SEs have a narrow electrochemical stability window, which causes degradation at the Li metal/SE interface. This degradation leads to high interfacial impedance and eventual cell failure.[46–49]

The decomposition of sulfide SEs, and corresponding SEI after contact with Li metal, has been characterized by various experimental and computational techniques, including x-ray photoelectron spectroscopy (XPS), Raman spectroscopy, x-ray diffraction, and density functional theory modeling.[40,50–52] Two distinct types of SEI chemistry have been observed.[20,21,53] The first

is an electronically insulating SEI such as that formed at the Li/Li_2S-P_2S_5 (LPS) interface, which decomposes Li_2S and Li_3P.[40] After initial SEI formation, further transport of electrons to the SEI/SE interface is limited, leading to a kinetically stable interface. The second type of SEI chemistry is a mixed electronic/ionic conducting interface, such as that formed by $Li_{10}GeP_2S_{12}$ (LGPS), which is formed of Li_3P, Li_2S, and an electronically conducting Li−Ge alloy ($Li_{15}Ge_4$).[47,54–56] In this mixed conducting case, electronic conductivity allows for electron transport to the SEI/SE interface even after initial SEI formation, leading to continued decomposition of the electrolyte.

One approach that has been proposed for stabilizing the sulfide electrolyte/Li-metal interface is the introduction of an artificial SEI by deposition of thin-film interlayers. An ideal artificial SEI layer would mirror a kinetically stable SEI, which is ionically conductive but electronically insulating.[47,57] In addition, it would exhibit a wide electrochemical window, low charge-transfer resistance at both the electrode and electrolyte interfaces, and it would be mechanically robust to allow volume changes upon charging/discharging to occur without degradation. Several recent studies that incorporate artificial SEI layers have observed decreases in interfacial degradation at low current densities (<1 mA/cm^2).[58–62]

One technique that has proven to be effective for the fabrication of artificial SEIs in various liquid and solid-state electrolyte systems is atomic layer deposition (ALD).[63–68] ALD is a modified chemical vapor deposition processes that conformally deposits thin (0.1-100 nm) films of a wide range of materials with atomically-precise control of thickness and composition.[69–71] This fine control of thickness and composition allows for atomically-precise control of artificial SEI interlayers.

As one of the most well-behaved, low temperature ALD processes, ALD Al_2O_3 has received particular attention as an interlayer in both liquid and solid-state battery systems. In liquid electrolyte systems, ALD Al_2O_3 has been shown to improve interface stability of both Li metal anodes and high voltage cathodes.[63,72–76] In solid state systems, ALD Al_2O_3 has also been shown to decrease improve by improving the wettability between Li metal/SE interfaces.[68]

In the past several years, initial efforts have begun to explore ALD interlayers for stabilizing the Li-metal interface in sulfide SE systems. Two recent studies in particular have explored directly depositing ALD Al_2O_3 layers onto the surface of Li metal foils, which were subsequently brought into contact with the sulfide SE.[77,78] While improvements in interfacial stability were observed, interfacial impedance in ALD Al_2O_3 coated Li metal was reported to increase during cycling. It was proposed that mechanical degradation of the ALD Al_2O_3 layer may play a role in the eventual degradation of the interlayer during cycling.[77] This proposed mechanism is consistent with the observation that ALD Al_2O_3 coatings on Li metal can experience fracture under tensile stresses.[79] Therefore, an improved understanding of the dynamic mechanisms and the coupled electro-chemo-mechanical evolution of ALD Al_2O_3 interlayers during cycling is important to the future development of artificial SEI layers. As a well behaved ALD process which has been investigated as an artificial SEI interlayer, ALD Al_2O_3 is an ideal model system for understanding the impact and failure mechanisms of artificial SEI.

In this work, we apply a multi-modal characterization approach to understand the impact of ALD interlayers on interfacial degradation of the LGPS/Li metal interface. We demonstrate that direct deposition of Al_2O_3 interlayers onto an LGPS surface delays interfacial degradation by modifying the dynamic evolution of SEI chemistry and morphology as the electrolyte first

comes into contact with Li. Electrochemical measurements of the ALD-coated samples indicate a delay in SEI growth and corresponding increase in interfacial impedance. Optical and scanning electron microscopy show that SEI formation and growth leads to mechanical degradation of the interface and confirm that ALD interlayers delay interfacial degradation. Additionally, *operando* x-ray photoelectron spectroscopy (opXPS) was used to probe differences in the chemistry of the SEI in coated and uncoated samples. Auger electron spectroscopy (AES) and *operando* optical video microscopy demonstrate the chemo-mechanical breakdown of the ALD interlayer, which leads to heterogeneous Li plating and eventual breakdown of the LGPS. These results provide insight into the mechanisms behind eventual failure of artificial SEI layers, and highlight the importance of mechanical properties in the development of future interlayers.

Results and Discussion

Li-Li Symmetric Cells

To probe the Li/LGPS interface, Li-Li symmetric cells with and without ALD coatings were assembled as shown in Figure 3.2a. 20 nm of Al_2O_3 was directly coated onto LGPS surfaces inside of an argon glovebox-integrated ALD system, allowing for surface modification and electrochemical testing without any air exposure. The ALD/LGPS interface was examined using cross sectional SEM (Figure 3.1). Electrochemical impedance spectroscopy (EIS) and post-

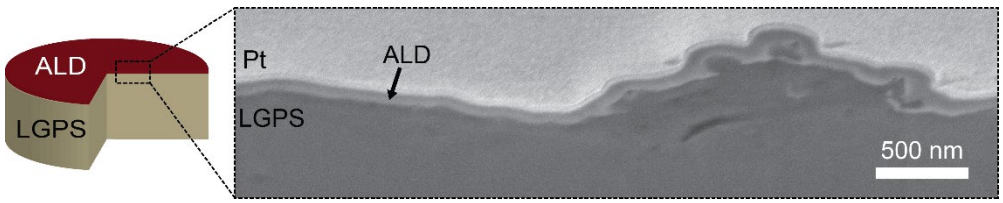

Figure 3.1. FIB-SEM cross section of the ALD coated LGPS surface. The ALD conformally coats the LGPS. Growth rates measured by SEM match those measured by elipsometry on adjacent Si samples. Pt was deposited in the SEM to achieve a clean cross section of the ALD.

mortem microscopy of these cells under open circuit conditions were used to study the effects of ALD interlayers on interfacial degradation. To study the dynamic evolution of the interface

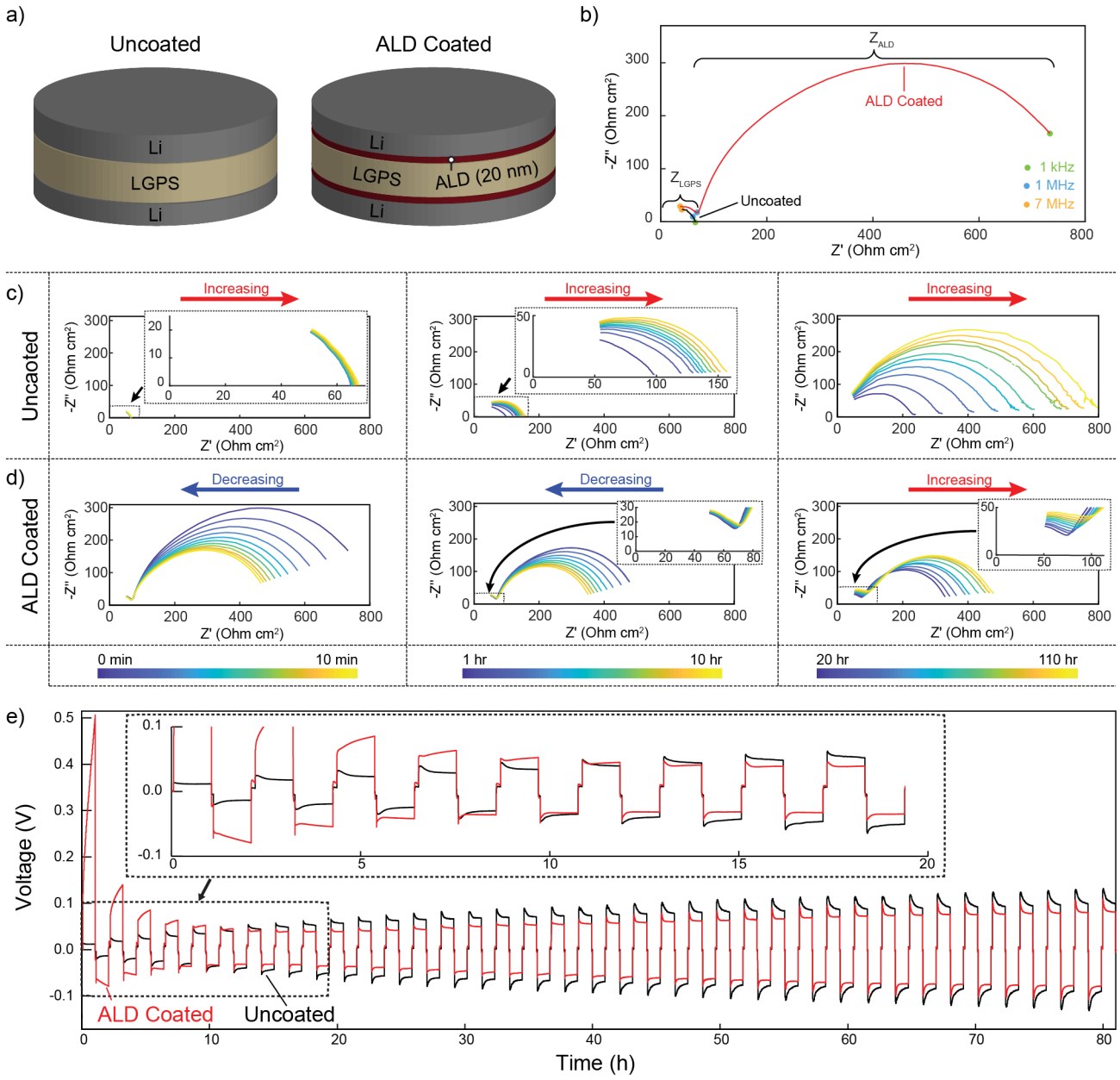

Figure 3.2. (a) Schematic of uncoated and ALD coated Li-Li symmetric cells. (b) Nyquist plot of the uncoated and ALD coated samples immediately after assembly. All EIS was performed at 26 °C. (c,d) EIS measurements of impedance over several time scales in both the coated and uncoated samples. e) Voltage traces of uncoated and ALD-coated Li-Li symmetric cells during cycling. During each half cycle 0.1 mAh/cm^2 (~0.44 µm) of Li was plated at a constant current of 0.1 mA/cm^2. Comparisons between early and late cycle voltage traces are shown in Figure 3.5a

under cycling, a complementary set of Li-Li symmetric cells were cycled at 0.1 mA/cm^2 and the voltage traces between the coated and uncoated samples were compared (Figure 3.2e).

Uncoated Li-Li Symmetric Cell. EIS analysis of uncoated samples immediately after assembly indicated LGPS conductivities of 3-4 mS/cm, which is comparable to those found in literature (Figure 3.2b).[41,54,58,59] A continuous increase in impedance over time at open circuit was measured by EIS (Figure 3.2c). The interface did not stabilize, even after several days of Li contact, after which time the impedance had increased by more than an order of magnitude. Similarly, in the uncoated cell that was cycled (Figure 3.2e), the voltage trace steadily increased throughout cycling (Figure 3.2e). The increasing impedance seen in both the cycled and un-cycled (open circuit) cells is attributed to the reduction of LGPS, which results in continual evolution of the SEI layer.

Disassembly and post-mortem optical microscopy of the open circuit cells provided evidence of LGPS reduction. Although Li metal initially adheres strongly to the LGPS surface, after 1 hr, the interface degraded to the point that the Li was easily removed from the surface, which resulted in significant visual darkening (Figure 3.3b). After 10 hrs of Li contact, the extent of this degradation increased, resulting in a surface with a larger density of reduction products (Figure 3.3c). Higher magnification images show that darkening is caused by black spots uniformly scattered across the surface. SEM images of the interface (Figure 3.3g-h) revealed that within the black spots, the surface is pitted, leaving a highly textured and fragmented surface.

The pitting and texturing of the surface is attributed to mechanical fracture of the LGPS. A recent study showed that sulfide SEs can expand significantly as they are reduced (in some cases up to 56%).[80] Using lattice parameters from The Materials Project, similar volume expansion calculations on LGPS decomposing into Li_2S, Li_3P and $Li_{15}Ge_4$ show a similar 52%

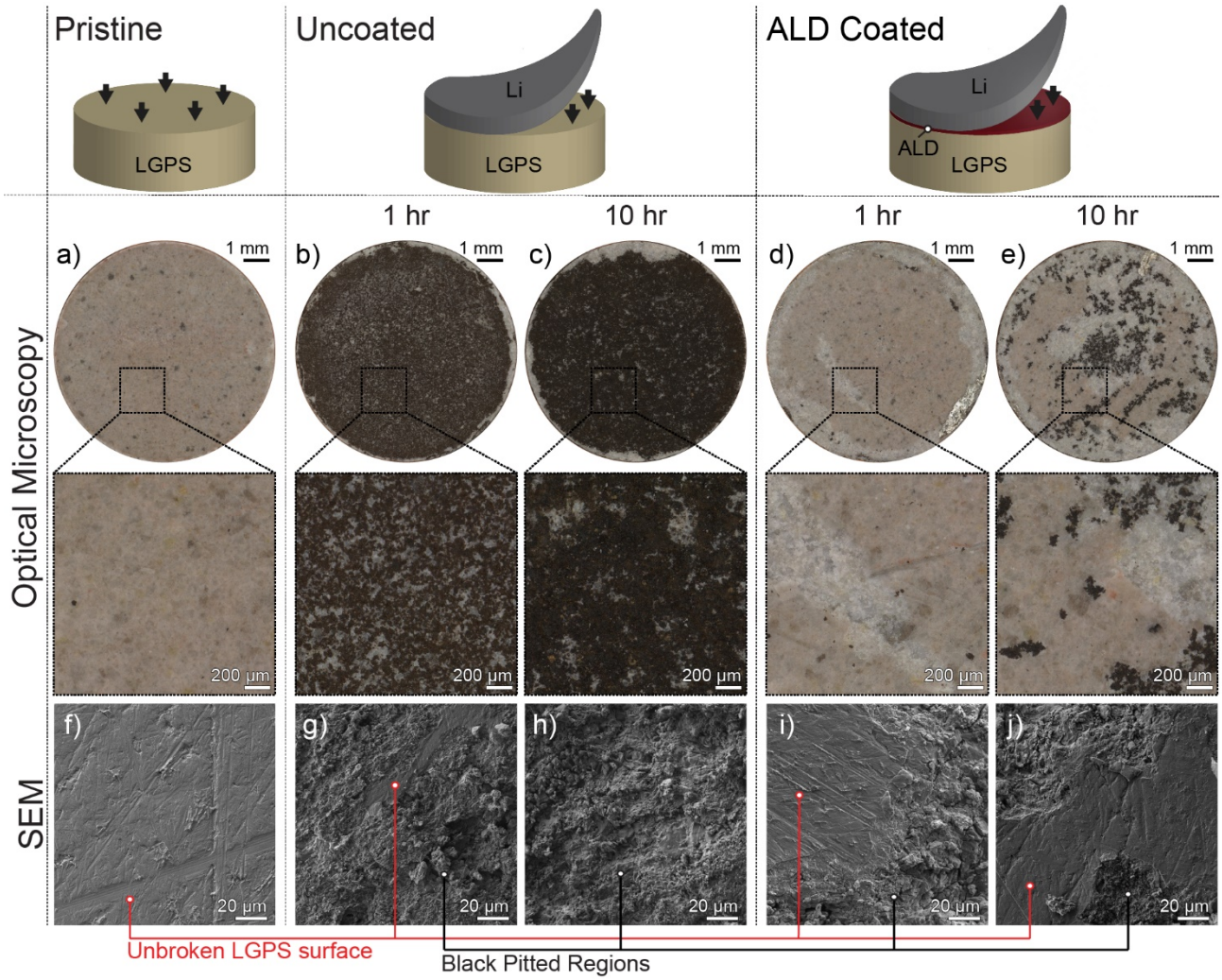

Figure 3.3. Optical and SEM images of the LGPS surface. (a) the LGPS surface before contact with Li metal. Images of the uncoated LGPS interface are shown after contact with Li metal for (b,g) 1 hr and (c,h) 10 hr. Images of the ALD coated LGPS surface are shown after contact with Li metal for (d,i) 1 hr and (e,j) 10 hrs.

expansion. [80,81] This expansion leads to mechanical fracturing LGPS in these blackened regions as it forms SEI compounds. In the uncoated sample, the majority of the surface has reacted, and the decreased ionic conductivity of these reduction products, combined with the mechanical degradation of the interface, lead to increased interfacial impedance in the degraded regions.

ALD Coated Li-Li Symmetric Cell. Before contact with Li metal, optical microscopy images of the LGPS surface showed a clean, polished surface (Figure 3.3a,f). EIS analysis of the ALD-coated sample immediately after cell assembly exhibits a high frequency semicircle of

similar magnitude to the uncoated sample. In addition, a second, lower frequency semicircle can also be observed (Figure 3.2b). The higher frequency semicircle corresponds to the bulk ionic conductivity of LGPS, which demonstrates that the ALD treatment does not significantly affect the bulk electrolyte. The lower frequency semicircle is thus attributed to the Al_2O_3 film.
EIS measurements over time in the ALD coated sample show that the bulk LGPS impedance (the higher-frequency semicircle) is significantly more stable than in the uncoated sample, and it does not significantly change for the first 10 hrs. It then increases slowly over the next 100 hrs (Figure 3.2d). In contrast, the impedance associated with the ALD layer (the lower frequency semicircle) decreases rapidly over the first 10 min. It continues to decrease slowly through the first 10 hrs, after which it begins to slowly increase over the next 100 hrs. Even after the total impedance of the ALD-coated sample begins increasing, the rate of increase remains significant slower than that of the uncoated sample and the total impedance of the uncoated sample eventually exceeds that of the ALD coated sample.

The cell cycling data (Figure 3.2e) further corroborate the trends observed in the EIS results. In the ALD-coated cell, a rapid drop in voltage was observed during the first several cycles, after which the voltage of the cell begins to increase. It is noteworthy that the time required for the impedance to first decrease, and then increase in the ALD-coated samples is similar for both the open-circuit and cycled cells. This implies that the reduction in impedance of the ALD film is predominantly driven by the chemical reaction with Li-metal, not by Li-ion transport through the film.

In contrast to the uncoated samples, after disassembly of the ALD-coated open circuit cells, the Li remained tightly adhered to the LGPS surface. Post-mortem optical microscopy and SEM analysis were used to demonstrate the delay in surface degradation as a result of ALD

treatment. After 1 hr of contact, there is very little darkening of the surface (Figure 3.3d). After 10 hrs of contact, sparse black spots are visible, implying that LGPS degradation is beginning to occur (Figure 3.3e). SEM images (Figure 3.3i,j) show that these black spots correspond to pitted and textured areas, similar to those seen across the entire surface of the uncoated sample. In agreement with the electrochemical data, these results demonstrate that the ALD film is able to temporarily stabilize the LGPS surface, but eventually starts to break down.

Previous computational studies have indicated that Al_2O_3 is not electrochemically stable in contact with Li metal. In particular, a recent study on potential interfacial layers for the stabilization of Li metal anodes shows a 1.23V (vs Li/Li^+) cathodic limit for pure Al_2O_3.[82] On the other hand, lithiated alumina phases (Li_xAl_yO) show significantly lower cathodic limits. Confirming these computational results, experimental studies have shown that Al_2O_3 protective layers in contact with Li-metal lithiate to form Li_xAl_yO, which has a higher ionic conductivity than Al2O3.[63,83–85] In addition to ionic conductivity changes, both modeling and experimental methods have shown that lithiation of Al_2O_3 leads to significant volume expansion (V/V_0=2.1).[86]

In agreement with these studies, we attribute the decrease in impedance in the ALD coated samples over the first 10 hrs to the lithiation of the Al_2O_3 to form Li_xAl_yO, which has a higher ionic conductivity than Al_2O_3.[84,85] As the film expands during lithiation, it eventually begins to fracture, which allows Li metal to contact the LGPS directly. Although bypassing the ALD interlayer initially contributes to the decrease in interfacial impedance, once the Li-metal contacts the LGPS directly, the LGPS begins to locally decompose at the interface in the fracture regions. Similar to that in the uncoated sample, the decomposition of the LGPS at the interface leads to the observed increase in interfacial impedance and the formation of localized dark spots seen in the ALD coated sample after 10 hrs of Li contact.

Operando X-ray Photoelectron Spectroscopy

The EIS and electrochemical-cycling data indicate that mechanical and chemical changes at the Li/LGPS interface evolve dynamically with time. To further probe these changes and the mechanisms behind the eventual mechanical failure of the ALD film, *operando* XPS (opXPS) was performed. In this technique, Li ions are electrochemically driven toward the SE surface allowing for real-time quantification of the chemical evolution of the SEI as it forms.[40,87]

OpXPS Overview. In opXPS, an electron gun is used to provide a flux of electrons to the surface of an exposed SE (Figure 3.4a). The backside of the SE is in direct contact with a Li source, and the electronically conductive Li source is grounded. Since the SE is an electronic insulator, as electronic charge accumulates on the exposed SE surface, a potential builds up across the cell. As the electrochemical potential of the exposed surface becomes more negative, Li ions are removed from the Li source and driven towards the exposed, analytical interface. At the surface, the Li ions can combine with electrons to form reduction products.

In addition to monitoring chemical changes at the interface, opXPS can also be used to analyze the total impedance and corresponding polarization associated with different cell layers.[40] During opXPS analysis, XPS measurements can be taken with and without bias (with or without electrons flooding the surface). The difference in peak position between these two measurements is equivalent to the potential difference from the grounded bottom electrode up to the phase being probed (Figure 3.4). For example, assume that after driving Li to the surface, the test cell had a chemical composition of LTO/LGPS/Li_2S/Li^0. If the Li_2S peak position without bias is 162.0eV and under bias the peak position shifts to 161.6eV, then the polarization across LTO/LGPS/Li_2S is 0.4eV. This hypothetical demonstrates how contributions to cell polarization can be measured up to an observed phase within the interface.

opXPS has been previously used to study the interfacial instability of Li_xP_yS (LPS).[40] It was demonstrated that the LPS decomposes into Li_2S, Li_3P and Li_2O before Li^+ can be reduced to

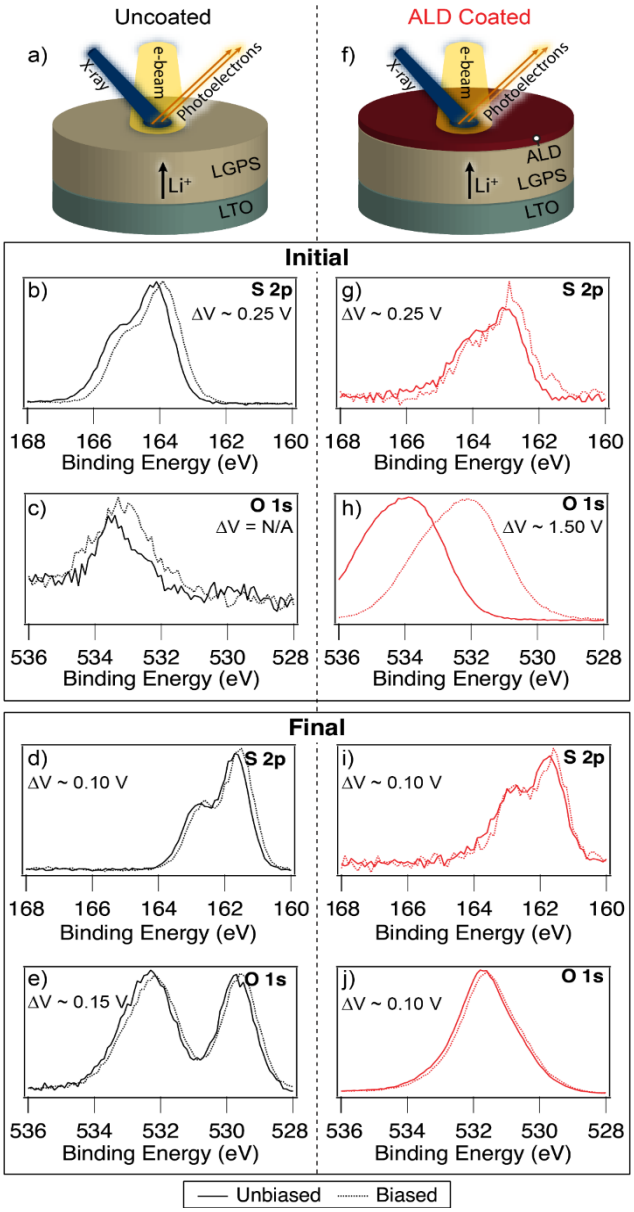

Figure 3.4. Comparison of XPS measurements for uncoated (black) and ALD coated (red) LTO/LGPS anode-free cells. (a,f) Schematic showing uncoated and ALD coated anode-free cells. XPS spectra of the S 2p and O 1s peaks were acquired with and without bias at t = 0 hrs (initial) and t = 12 hrs (final). The S 2p spectra at t = 0 hrs (b,g) and t = 12 hrs (d,i) correspond to LGPS and Li_2S respectively. The O 1s spectra in the ALD coated sample at t = 0 hrs (h) and t = 12 hrs (j) correspond to the Al_2O_3 film and Li_xAl_yO layer respectively. The O 1s spectra in the uncoated sample at (c,e) correspond to impurities.

form Li metal. For the reader's reference, a more comprehensive explanation of the details and physics of opXPS is also included in that study.[40]

OpXPS Polarization Measurements. In this study, opXPS was used to quantify the chemical evolution of the LGPS/Li-metal interface, with and without ALD interlayers. Anode-free cells were fabricated using a composite $Li_4Ti_5O_{12}$ electrode (LTO) as the Li source. LTO was chosen because it has a relatively flat voltage profile, and the fact that the LGPS/LTO interface is more stable than Li/LGPS (Figure 3.5b). The use of LTO therefore minimized changes in cell polarization associated with the bottom electrode/LGPS interface. For the ALD coated samples, a thinner (4 nm) coating was used so that the underlying LGPS spectra could simultaneously be observed.

For XPS analysis, the bare LGPS surface of the uncoated sample (Figure 3.4a) and the Al_2O_3 surface of the ALD-coated sample (Figure 3.4f) were exposed to an ultra-high vacuum (UHV) environment. A bias was applied for 12 hrs, which drove Li ions to the exposed surface. The cell polarization was measured at the start and end of the 12-hr lithiation. In this experiment, four different experimental conditions were measured for each sample, (I) before lithiation non-biased, (II) before lithiation biased, (III) after lithiation non-biased, (IV) after lithiation biased. For the control sample, Figure 3.4b shows the S 2p core spectrum under conditions I (solid line) and II (dashed line) while Figure 3.4g shows the S 2p under conditions III (solid line) and IV (dashed line).

Consistent with the EIS results from the Li-Li symmetric cells, the uncoated sample exhibits only a small shift in the S spectra with and without bias (0.25V, Figure 3.4b). Since the sulfur at this point is only associated with the LGPS phase, this shift corresponds to the polarization across the LTO/LGPS stack. The ALD-coated sample shows an equivalently small

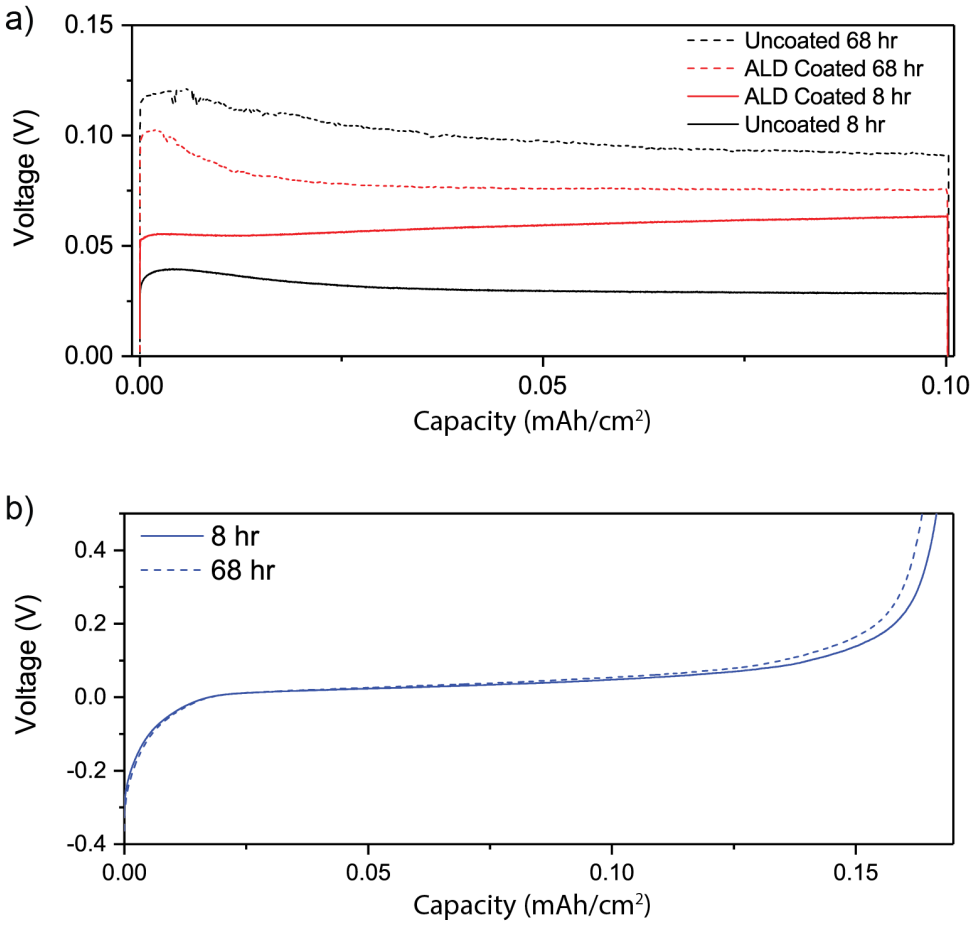

Figure 3.5. (a) Voltage profiles of uncoated and ALD coated Li-Li symmetric cells at 8 hrs and 68 hrs of cycling. (b) LTO/LGPS/LTO symmetric cell charging cycles with a current density of 0.02 mA/cm^2. Little change is observed after formation cycles (8 hrs after start of cycling) and after significant cycling (after 68 hrs of cycling).

shift in the S spectra (Figure 3.4g). This equivalent shift demonstrates that the polarization across the LTO/LGPS portions of the test cells were nearly identical, regardless of the presence of an ALD coating. These results are consistent with the EIS data shown in Figure 3.2b, where the high-frequency semi-circle associated with bulk transport through the LGPS is similar in both the coated and uncoated samples.

However, unlike the uncoated sample, the ALD coated sample exhibits a large shift in the O spectrum (~1.5V) under bias, which corresponds to polarization across the entire LTO/LGPS/Al_2O_3 stack (Figure 3.4h). Since ionic transport through the LTO/LGPS portion of

the stack contributed ~0.25V to the cell polarization, the contribution to polarization associated with the initial Al_2O_3 layer was ~1.25 V. However, the difference between the biased and unbiased spectra decreased rapidly during lithiation. After 12 hrs, the contributions to polarization associated with the Al 2p and O 1s (i.e. the initial ALD layer) were negligible (~0.1 V or less) (Figure 3.4j). These results agree well with the EIS and voltage trace data shown in Figure 3.2, which exhibited an initial decrease in impedance.

OpXPS Chemical Evolution Measurements. In addition to polarization measurements, opXPS was used to probe the time-dependent chemical evolution of the surface. Throughout the 12 hr lithiation of the coated and uncoated samples, XPS spectra (Li 1s, Al 2p, S 2p, C 1s, O 1s, and Ge 2p core levels) were acquired every 15 min. Spectra were taken while the bias was applied. The evolution of these XPS spectra is shown in Video A, and a graphical representation is shown in Figure 3.6. In the graphical representations, each image represents one core level for a specific sample (uncoated: grey, ALD coated: red), with areas of high intensity appearing white and areas of low intensity appearing black. Analysis of both Figure 3.6 and Video A reveal significant differences in the chemical evolution of the SEI layer between the two samples as Li is transported to the surface. An schematic summarizing the observed changes is given in Figure 3.8.

For the uncoated sample, S, P and Ge at the surface are quickly reduced to Li_2S, Li_xP and reduced Ge. These changes are clearly observed in the S 2p, P 2p, and Ge 2p core levels, but also evident in the Li 1s core spectra, which exhibit a consistent and gradual shift toward lower binding energy. (Figure 3.6 (i)) These reduction products match those expected based on previous computational and experimental studies.[47,54,55] After approximately 6-8 hrs, a low-binding-energy peak associated with Li_2O begins to appear (Figure 3.6 (ii)). Previous opXPS

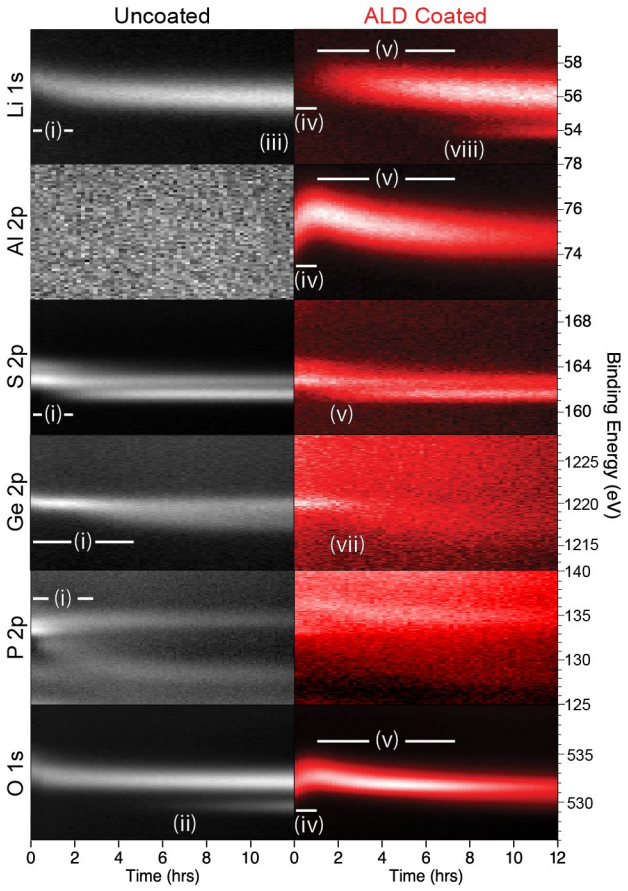

Figure 3.6. Spectra from opXPS at the LPGS surface for the Li 1s, Al 2p, S 2p, Ge 2p, P 2p, and O 1s peaks. Data is plotted such that spectra of high intensity appear white.

results on LPS show that this Li_2O formation originates from oxygen impurities in the SE.[40] Even after 12 hrs of charging, no metallic Li was present at the surface of the uncoated sample (Figure 3.6 (iii)).

For the ALD-coated sample, the initial Al_2O_3 coating attenuated the signal from Ge and P, and significantly reduced the signal associated with S. During the initial lithiation of this sample, the most significant chemical changes were observed in the Al 2p and O 1s core levels. As seen in Figure 3.6 (iv), during the first hr of lithiation the binding energies associated with the Al 2p and O 1s peaks increase; and for the Li 1s spectra very little Li was observed. After 1 hr, a more pronounced Li signal was observed and the Li 1s, Al 2p and O 1s core levels experienced a

notable decrease in binding energy (Figure 3.6 (v)). At around 2 hrs, a shift in the S peaks occurs, indicating some reduction of S into Li_2S on the LGPS surface (Figure 3.6 (vi)). Although greatly attenuated, a shift is also faintly visible in the Ge 2p peak indicating the reduction of germanium (Figure 3.6 (vii)). At the 6 hr point, a new low binding energy peak associated with Li metal appears (Figure 3.6 (viii)). These observations from Figure 3.6 indicated two things. First, the contribution to polarization associated with the ALD layer decrease dramatically during the first hr, which is evident by the increasing binding energy position (Figure 3.6 (iv)). Second, the ALD layer continues to chemically evolve during prolonged lithiation, which is evidenced by the decrease in binding energy after one hr of lithiation to form Li_xAl_yO (Figure 3.6 (v)).

To provide further mechanistic insight into the evolution occurring at the ALD interface, AES analysis was also performed after the 12-hr opXPS lithiation (Figure 3.7). These results indicate that cracks formed in the ALD layer, which lead to preferential localized Li deposition within the cracks.

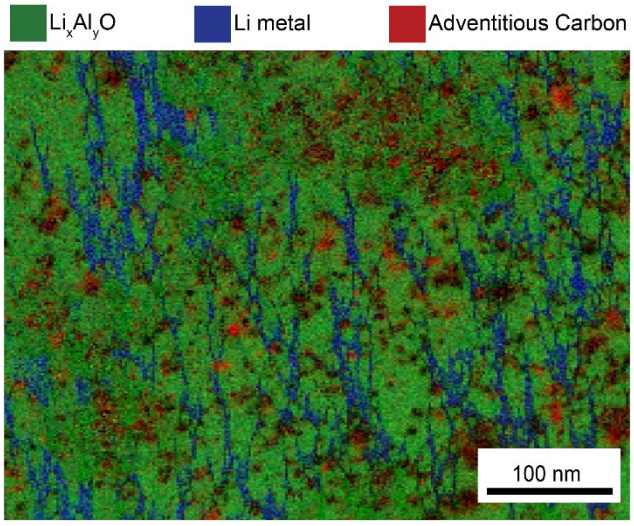

Figure 3.7. AES spectrograph of ALD coated LGPS surface after opXPS experiments. The lithiated ALD film has cracked and Li metal has plated in the cracks.

By combining the insights from the opXPS observations with the AES observations, we propose the following mechanism. During the initial lithiation of Al_2O_3, Li_xAl_yO begins to form, which causes an increase in ionic conductivity of the ALD film as it lithiates (Figure 3.8b). This increase in ionic conductivity results in a subsequent shift of spectral intensity toward higher binding energy in the opXPS measurements. However, the formation of Li_xAl_yO leads to cracking, as seen in the AES data, due to the volumetric expansion of the Al_2O_3 film as it reacts with lithium[83].The formation of these cracks likely coincide with appearance of Li_2S, which is an initial reduction component of LGPS reacting with Li. After 6 hrs, Li metal begins to appear

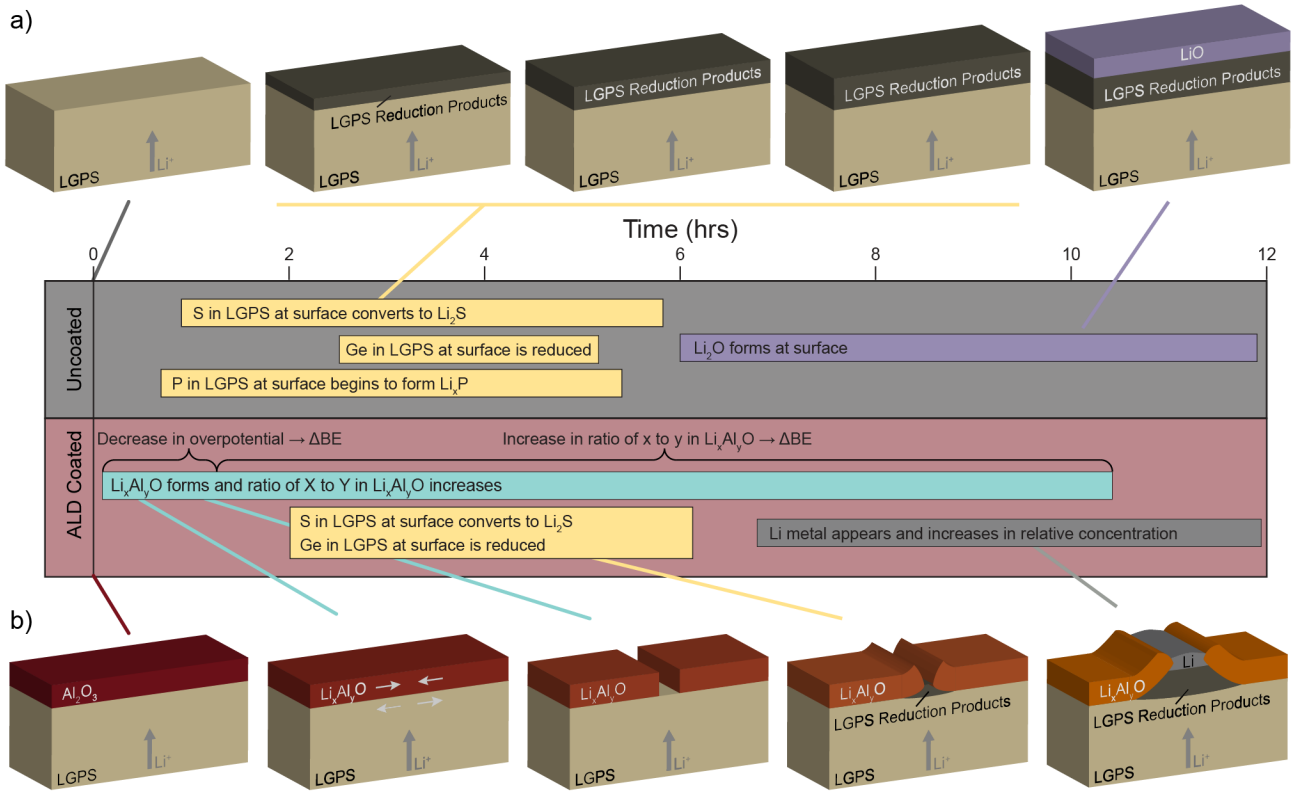

Figure 3.8. Timeline and schematics showing evolution of the LGPS surface during opXPS experiments. (a) The Uncoated sample shows rapid reduction of the LGPS into Li_2S, Li_xP and Li_xGe. After ~6 hr, Li_2O begins forming at the surface. Li metal plating is not observed even after 12 hr. (b) The ALD coated sample shows the lithiation of the Al_2O_3 layer into Li_xAl_yO which leads to cracking of the ALD film. As the cracking occurs, the LGPS begins to be reduced and by ~7 hr Li metal begins plating out in the cracks. ΔBE is the change in binding energy observed in the XPS spectra.

within the cracks (Figure 3.8b). In contrast, Li plating was not detected throughout the entire 12 hr experiment in the uncoated sample. This difference indicates that despite the mechanical fracturing of the Al_2O_3 film, the ALD coating limits the reduction of LGPS and corresponding SEI formation, allowing for Li plating to occur after less charge has been passed.

Operando optical visualization

To provide further insights into the coupled electro-chemo-mechanical behavior of these systems, *operando* optical video microscopy was performed during electrochemical cycling.[13,88] This *operando* visualization technique was performed in an LTO/LGPS/Mo cell, where 300 nm thick molybdenum current collectors were sputtered onto the ALD-coated (Figure 3.9b) and uncoated (Figure 3.9a) LGPS surfaces to form LTO/LGPS/Mo anode-free cells.[15] Mo deposition was performed in an argon-glovebox-integrated sputter chamber, without any air exposure. A galvanostatic current was applied to drive Li from the LTO electrode to the surface of the Mo current collector. A current density of 0.01 mA/cm^2 across the Mo current collector was used in order to approximate the currents used in the opXPS experiments.

The initial surfaces of the current collectors deposited on both the ALD-coated and uncoated samples are shown Figure 3.9e,f. The synchronized evolution of the Mo surfaces and cell voltage traces are shown in Videos B and C.

Operando optical microscopy images of the uncoated sample after 10 hrs of charging exhibit a relatively homogenous darkening of the Mo current collector (Video B, Figure 3.9g). This darkening also extends radially beyond the edges of the circle and is attributed to reduction of the LGPS and formation of SEI byproducts beneath the current collector. In contrast, in the ALD-coated sample, this homogeneous darkening and radial expansion are not observed.

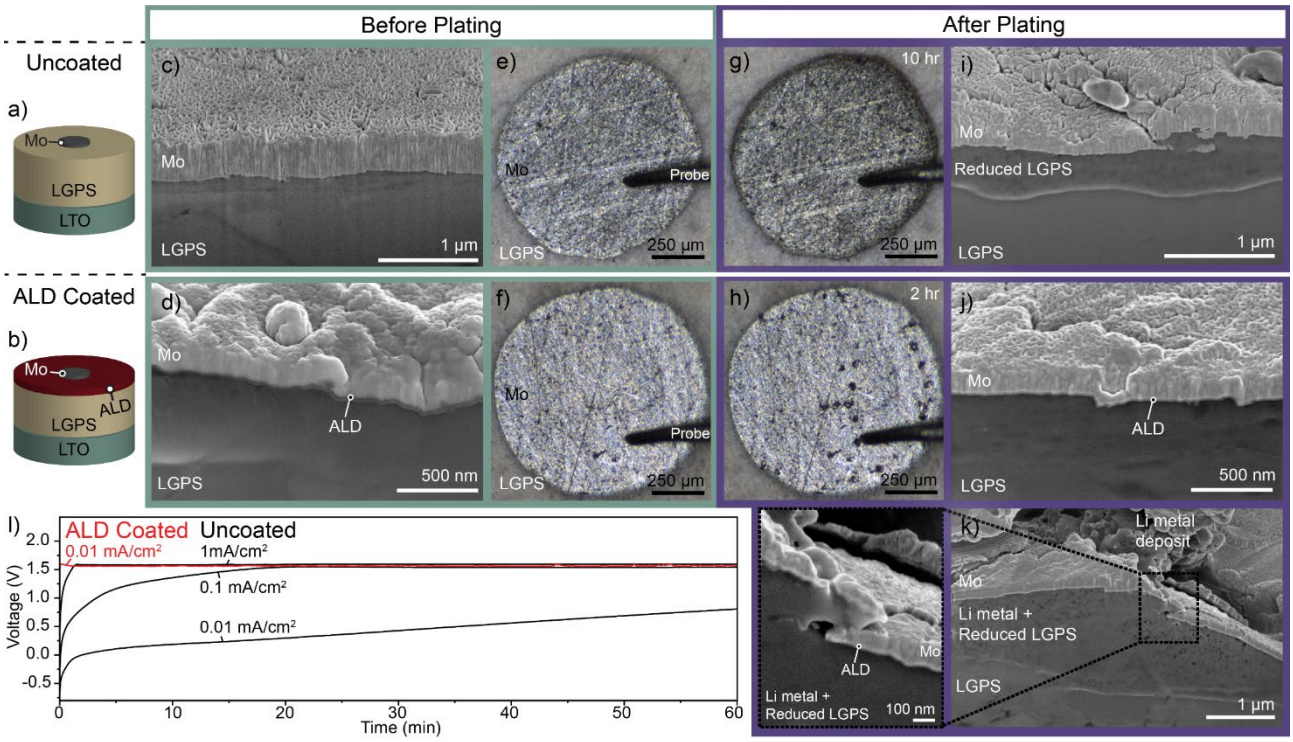

Figure 3.9. *Operando* optical microscopy of LTO/LGPS/Mo anode-free cells. (a) and (b) show schematics of the anode-free cells in the uncoated and ALD coated cases respectively. (e,f) Before charging in both the uncoated and ALD coated samples, the circular Mo current collector is visible on the surface of the LGPS. (c,d) FIB-SEM cross-sectional images show clean interfaces between the Mo and the LGPS, with the ALD film visible at the interface of the ALD coated sample. (g) In the uncoated sample, after 10 hr charging at 0.01 mA/cm^2 visible darkening occurs across the surface of the current collector as the LGPS under the Mo is reduced. (i) After charging, cross-sectional FIB-SEM confirms reduction across the entire LGPS/Mo interface. (h) In contrast, after only 2 hrs of charging at 0.01 mA/cm^2, the ALD coated sample shows Li metal deposition in several hotspots with other regions of the ALD sample showing no visible LGPS reduction. (j) Cross-sectional FIB-SEM confirms that away from hotspots there is little evidence of LGPS reduction or Li metal plating. (i) Cross-sectional FIB-SEM at the hotspots shows Li metal and reduced LGPS underneath cracks in the Mo. Additional Li-metal is visible on the surface after having extruded through cracks in the ALD/Mo bilayer. (l) Voltage profile of LTO/LGPS/Mo anode-free cells at varying current densities.

Instead, evidence of Li plating "hotspots" appears across the surface of the current collector (Video C, Figure 3.9h). These nucleation events occur in the early stages of plating (<2 hr).

Ex situ SEM images of focused ion beam cross sections (FIB-SEM) in Figure 3.9c,d,i-k show the surface before and after charging. In the uncoated sample, a clean LGPS/Mo interface is

observed before charging. After charging, LGPS reduction products are visible along the entire Mo/LGPS interface (Figure 3.9i).

In the ALD-coated sample, the thin Al_2O_3 layer is visible between the LGPS and Mo before charging (Figure 3.9d). After charging, distinct differences were seen in the sub-surface morphology between regions in the vicinity of a hotspot and the regions where no optically visible changes occurred. In the FIB-SEM images, the majority of the interface in regions away from hotspots showed no evidence of LGPS reduction products (Figure 3.9j). In sub-surface regions adjacent to the hotspots, clear evidence of LGPS reduction products and Li plating were visible. Additionally, while the ALD film remains adhered to the Mo surface, cracking of the ALD and Mo films can be observed. Furthermore, the base of the Li-metal deposit, which extruded through the cracks, is visible as well (Figure 3.9k). This observation is consistent with the AES analysis, where lithium plating is selectively observed in the regions where the ALD film cracked. The extruded geometry of the plated Li metal is further evidence of the coupled mechanical-electrochemical nature of the interfacial dynamics, as the flow of Li out of the crack will be affected by visco-plastic nature of Li metal.[79]

We note that the spacing between the cracks from the AES result were much smaller than the spacing between the macroscopic Li filaments grown in the optical visualization platform. This difference in spacing could be due to several factors, including the mechanical constraint of the metal current collector on top of the ALD film (which is absent in the AES analysis), the electrical conductivity of the metal current collector, variations in the local electric field, etc. While a full electro-chemo-mechanical analysis would be needed to fully reconcile these two experimental platforms, these results demonstrate the critical role that mechanical stress

evolution plays at Li-metal/SE interfaces, and points towards the need for development of mechanically tough and ionically conductive interlayers.

One of the major advantages of the *operando* visualization platform is the ability to time-synchronize the voltage trace of the cell with the optical images. The corresponding voltage traces from the *operando* cell are shown in Figure 3.9l. In the ALD-coated sample, the cell voltage rises to 1.53 V within the first few seconds at a current density of 0.01 mA/cm^2. This voltage corresponds to the measured open-circuit voltage of the LTO electrode vs. Li metal in a liquid electrolyte and indicates that Li metal is depositing at the anode.

In contrast, the voltage trace of the uncoated sample at 0.01 mA/cm^2 slowly rises without reaching the Li metal/LTO potential even after 23 hrs (Figure 3.10). Not reaching this potential implies that LGPS is being continually reduced at the interface, and Li metal has not yet plated out. This result is consistent with the FIB-SEM observation of the uncoated sample where no Li-plating is observed and a reduced LGPS SEI layer is present along the interface (Figure 3.9i).

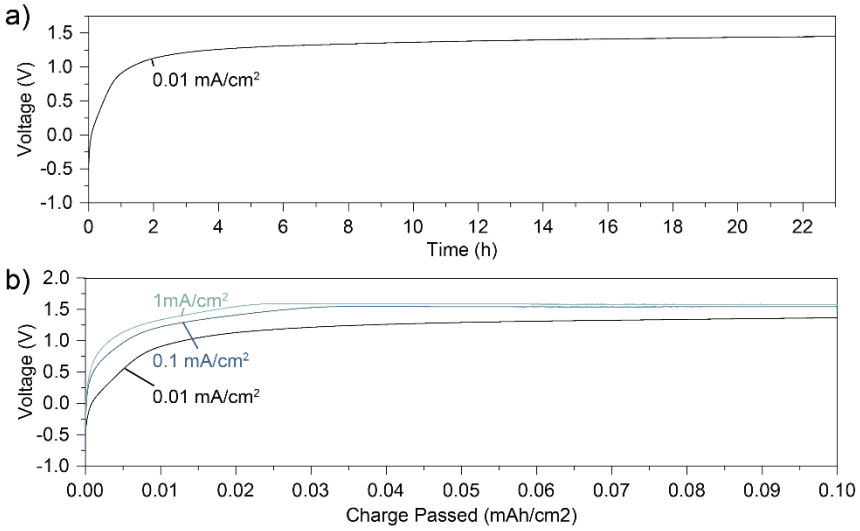

Figure 3.10**.** (a) Extended voltage trace of 0.01 mA/cm^2 uncoated half cell shown in Figure 3.9. Even after 23 hr the cell has not reached 1.53 V (the Li/LTO OCV potential). (b) Voltage traces from Figure 3.9l plotted with respect to charge passed. At higher current densities Li metal plating occurs with less total charge passed.

This result is also consistent with the opXPS results, wherein the LGPS surface decomposes before metallic Li forms, and the onset of Li metal plating occurs sooner in the ALD-coated sample.

By going to higher current densities in the uncoated sample, the onset of Li metal plating can be accelerated dramatically, as shown by the time required to reach the plateau voltage of 1.53 (Figure 3.9l). Interestingly, the amount of charge required to reach 1.53 V decreases as current density increases. In other words, if the current density is increased by a factor of 10, the time required for the onset of Li plating decreases by more than a factor of 10.

One way to rationalize this behavior is to consider the competing kinetics of Li-plating and LGPS reduction. As the total flux of Li ions to the electrochemically active interface increases, a kinetic competition between reaction pathways determines the relative rate of each reaction. At low current densities in the uncoated sample, the LGPS is reduced as quickly as Li^+ are transported to the surface, but at higher current densities the flux of Li^+ outpaces the reduction of the LGPS and Li metal begins to plate on the surface. These different pathways are analogous to spatially varying kinetics among different reaction pathways at Li metal/liquid electrolyte interfaces, which have been shown to strongly influence the voltage trace of Li metal batteries.[13,14,89]

The disproportional hastening of lithium plating at higher current densities in the uncoated samples also points towards one of the influences that the ALD film has on SEI formation. In the ALD-coated sample, the local current density within the cracks is significantly amplified, and therefore the onset of Li plating occurs much sooner than in the uncoated samples. This hastening influences the nature of the SEI that forms. For example, as shown in

the opXPS analysis, Li_2O forms after extensive SEI formation in the uncoated sample, which was not observed in the ALD coated sample before metallic Li plated out.

As shown in Figure 3.2 and Figure 3.3, the evolution of the interfacial impedance of the cell and stabilization of cycling behavior is influenced by the ALD film even after degradation begins to occur, which is likely due to the nature and extent of LGPS reduction at the interface. Ultimately, the design of a stable interlayer must take into account the coupled electro-chemo-mechanical evolution of the interface. Through an improved understanding of the dynamic evolution of the interface with and without the presence of artificial SEI layers, the insights provided from this study point towards design principles for further improvement of interlayers.

Conclusions

In summary, we applied a multi-modal approach to understand LGPS degradation in solid-state Li-metal batteries, and the impact of ALD Al_2O_3 interlayers on this interface. We show that Al_2O_3 interlayers provide short-term stabilization of the interface and slow down the eventual SEI formation. We utilized these interlayers as a model system to improve our understanding of the mechanisms behind SE stabilization and the electro-chemo-mechanical phenomena that lead to eventual decay of artificial SEIs.

As-deposited Al_2O_3 has low ionic conductivity, which increases due to lithiation to form Li_xAl_yO. This lithiation process also leads to volumetric expansion of the ALD film. Due to the brittle nature of Al_2O_3 it is unable to accommodate this strain and eventually fractures. As a consequence of interlayer cracking, current focusing within the cracks occurs, which accelerates Li metal plating relative to SEI formation.

We observed two main effects that limit the long-term effectiveness of Al_2O_3 and similar artificial SEI. 1) During early stage cycling the low ionic conductivity of Al_2O_3 increases the overall cell impedance. This challenge can be directly addressed by developing interlayers with higher ionic conductivities. 2) With extended cycling the ALD layer fractures and is no longer able to passivate the LGPS surface. The Al_2O_3 coatings break down through a two-step process. Initially, the reaction with lithium metal results in the formation of Li_xAl_yO, which is desirable, and increases the ionic conductivity of the artificial SEI. However, after continued lithiation of the ALD film, volumetric expansion leads to cracking. By either entirely preventing the lithiation of the artificial SEI and/or by modifying the mechanical properties of the artificial SEI, its cracking and eventual degradation may be prevented.

To summarize, if ALD interlayers can be developed with 1) high ionic conductivities, 2) minimal volume changes when in contact with Li metal, and 3) improved mechanical properties, long term-improvement in interface stability and performance may be realized.

Experimental Section

Preparation of LGPS State Electrolyte

All air-sensitive materials were handled in an Ar-filled glovebox (MBraun) with oxygen and moisture levels maintained < 0.5 ppm. $Li_{10}GeP_2S_{12}$ (LGPS) powder (MSE Supplies) was used as received. 6 mm diameter pellets were fabricated from 106 mg of LGPS powder by cold pressing (26 °C) at 520 MPa for 10 min. After pressing, both sides of the pellets were polished using 2000 grit sandpaper. Sample densities were determined using geometrical measurements and weight. Thicknesses were consistently 1.98-2.03 mm. Relative densities compared to that of theoretical LGPS were consistently 89%-90%.

Li-Li Symmetric Cell Assembly

Li metal electrodes were prepared from metal foil (750 µm thick, Alfa Aesar). The Li foil surface was scraped and flattened to remove surface layers and achieve a shiny metallic surface. Symmetric Li/LGPS/Li cells were then assembled with 8.8 MPa stack pressure.

LTO Pre-lithiation

Li-LTO coin cells were assembled and cycled to lithiate the LTO active material. Li-LTO cells were assembled using CR2032 coin cell cases, spacers, and wave springs. The electrolyte was 1M $LiPF_6$ in 1:1 EC:EMC (Soulbrain) and 75 µL was used per cell. Li metal (750 µm thick, Alfa Aesar) was used as the counter/reference electrode against the LTO working electrode. The LTO anodes were received from the CAMP facility at Argonne National Laboratory and have a capacity of 160 mAh/g and a loading of 1.96 mAh/cm^2.

After assembly, cells were first rested for 6 hrs to ensure full electrolyte infiltration into the LTO anodes, followed by 3 formation cycles at C/10 rate between 1-2 V vs. Li counter electrodes. For the last formation cycle, cells were stopped after once a cutoff voltage of 1.53 V was reached, which is just before the end of the LTO voltage plateau (Figure 3.11). The lithiated

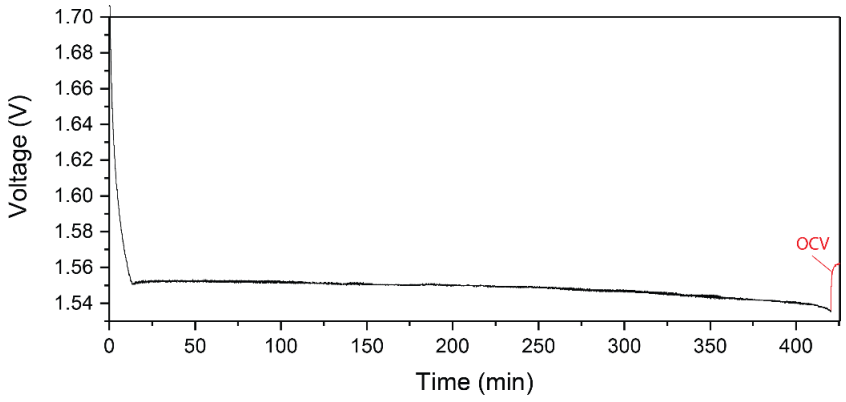

Figure 3.11. Final lithiation cycle and following OCV rest of LTO electrode in liquid electrolyte coin cell.

LTO electrodes were collected from coin cells and rinsed with fresh dimethyl carbonate multiple times to remove electrolyte residue. The electrodes were dried in the glovebox antechamber under vacuum.

LTO Anode-free Cell Assembly

Lithiated LTO, LGPS powder, and carbon black conductive additive (C-nergy Super C65) were combined in a 3:6:1 (wt%) ratio and mixed by mortar and pestle for 10 min to form a composite LTO electrode. LTO/LGPS anode-free cells were formed by lightly pressing and electrolyte pellet using 104 mg LGPS powder, and then subsequently pressing an additional 7.3 mg (1 mAh/cm^2) composite LTO powder against one side of the electrolyte. The entire anode-free cell was then pressed at 520 MPa for 10 min. The LGPS surface was polished with 2000 grit sandpaper. 300 nm current collectors were sputtered onto the surface of the samples used for *operando* video microscopy using a glovebox integrated Angstrom Engineering Nexdep sputter coater.

ALD Al_2O_3 Surface Coating of LGPS Pellets

ALD coatings were carried out in a Savannah S200 Ultratech ALD reactor that is integrated into an argon glovebox, allowing for direct coating of the LGPS surface and cell assembly without air exposure.[63] Trimethylaluminum (TMA) and O_3 as precursors. LGPS pellets were coated at 60°C using TMA pulses of 0.1 s, ozone pulses of 4 s, and a carrier gas flow rate of 10 SCCM Argon. Growth rates were measured on (100) silicon using both *in situ* QCM and ex-situ ellipsometry. Al_2O_3 growth rates of 1 Å/cycle were measured using SEM (Figure 3.1, FEI Helios 650 Nanolab SEM/FIB) and ellipsometry (Woollam M-2000DI). Multiple ALD thicknesses were tested and

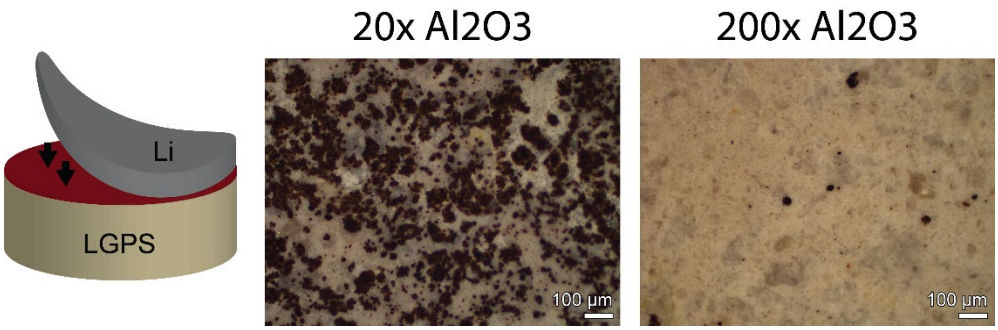

Figure 3.12. Optical microscopy of ALD coated LGPS surfaces with different numbers of ALD cycles after 1 hr of contact with Li. 200 cycles of Al_2O_3 showed significantly better stabilization than 20 cycles.

200x (20 nm) was chosen based on preliminary performance for Li-Li symmetric cells and for operando video microscopy cells (Figure 3.12). A thinner (4 nm) coating was used for the opXPS experiments so that the underlying LGPS spectra could simultaneously be observed.

Electrochemical Characterization

All electrochemical measurements were taken using biologic potentiostats (SP-200 and VSP) at 26 °C. Complex impedance measurements were taken using EIS with a 10-mV sinus amplitude and a frequency range of 6 MHz to 1 kHz. Li-Li symmetric cell cycling was performed at 0.1 mA/cm^2. Lithium plating in LTO/LGPS anode-free cells for *operando* XPS was done at ~4 $\mu A/cm^2$. Anode-free cells with currents between 0.01 mA/cm^2 – 1 mA/cm^2 were used for *operando* optical visualization.

SEM and Optical Microscopy

Post-mortem optical microscope images of the interface were taken in an Ar environment using a Keyence VHX-7000 digital microscope. A Tescan MIRA3 GMU FEGSEM was used for top-down SEM analysis. FIB cross-sections were made and analyzed using an FEI Helios Nanolab 650 SEM/FIB.

Optical Visualization Cell

Synchronized plan-view optical visualization was performed using a custom build visualization platform. Current was applied by a probe contacting the Mo surface. Videos were taken with an Opto Engineering RT-HR-6M-71 telecentric lens.

Operand Photoelectron Spectroscopy (op-XPS)

OpXPS measurements were performed using a Physical Electronics 5600 photoelectron spectrometer at ultrahigh vacuum (~5×10^{-10} Torr). Monochromated Al Kα X-rays were generated with an anode power of 350 W. The sample surface normal was oriented at 45° to both the X-ray source and photoelectron spectrometer. An optimal noise to resolution pass energy was determined to be 29.35 eV. In this work relative (delta) Binding-energy (BE) shifts are used as described elsewhere.[87] Curve fitting and data processing was performed using Igor Pro with a custom program adapted from Schmid et. al.[90]

Auger Electron Spectroscopy

AES measurements were performed using a Physical Electronics 670 system, under beam energy of 5 kV, with 20-nA beam current. Typical pressures were ~7×10^{-10} Torr. Samples were loaded into the XPS without air exposure through a connected glovebox. After *operando* XPS testing samples were transferred directly into AES for analysis through a UHV connection.

Chapter 4

Interphase Dynamics in Anode-Free Solid-State Batteries

Adapted with permission from Davis, A. L.; Kazyak, E.; Liao, D. W.; Wood, K. N.; Dasgupta, N. P. Operando Analysis of Interphase Dynamics in Anode-Free Solid-State Batteries with Sulfide Electrolytes. *Journal of The Electrochemical Society* **2021**, *168* (7), 070557.

In Chapter 3, we investigated interface degradation of LGPS/Li, showing that LGPS is very unstable against Li metal. In addition to that work, a number of other studies have used a wide range of techniques to analyze sulfide SE/Li-metal interfaces[91,92] including XPS [40,53,54,93], Raman spectroscopy[50], x-ray diffraction[94], x-ray tomography,[95,96] density functional theory[48,52], and molecular dynamics modeling [51]. In addition to the thermodynamic instabilities calculated for sulfide SEs, the role of SEI formation kinetics has been investigated. Among the SEs that are thermodynamically unstable vs Li metal, two distinct categories of SEI have been observed.[20,21] In the first category, which includes LPSCl (Li6PS5Cl) and LPS (Li3PS4), the SEI components are electrically insulating. Therefore, after initial SEI formation, the interface stabilizes, resulting in a thin and low-resistance SEI. [40] In contrast, SEs the second category [including LGPS (Li10GeP2S12) and LSPS (Li10SnP2S12)], form an SEI with electrically conducting constituents. This electrically conducting interphase allows for continuous transport of electrons to the SE/SEI interface, resulting in continued degradation of the SE and formation of a thick

SEI. The formation of this thick SEI consumes active Li and causes mechanical degradation of the interface, leading to low Coulombic efficiencies, high cell impedance, and eventual cell failure.[5,47,54–56]

While several fundamental studies have led to an improved understanding of individual electrolytes, fewer *in situ/operando* studies have performed to directly contrast these two SE categories.[94] Additionally, most previous work has focused on a single technique; however, multi-modal *operando* characterization using complimentary microscopy and spectroscopy techniques is a powerful approach to further elucidate the complex interplay between the electrical, chemical, and mechanical mechanisms leading to electrolyte degradation.[40,92,94,97]

An emerging class of SSBs where differences in SEI formation dynamics are particularly impactful is anode-free batteries, where the Li metal anode is completely formed *in situ* using Li provided by the cathode. Anode-free batteries have received increased attention recently due to their potential to increase battery energy density and ease of manufacturing. [15,16,98–100] In addition to these potential benefits, anode-free cells allow for quantitative analysis of SEI formation and Coulombic efficiency because the SEI is formed exclusively during cycling and is therefore not convoluted with prior SEI formation during cell assembly. Furthermore, the SEI is not buried underneath a bulk Li electrode during SEI formation, which facilitates SEI analysis using a variety of *operando* techniques.[5]

In this work, we investigate the role of sulfide SE stability during Li plating on LPSCl (electrically insulating SEI) and LGPS (electrically conducting SEI) electrolytes in anode-free cells. We apply a multi-modal approach that combines operando analysis with post-mortem characterization of SEI formation across multiple length scales, ranging from bulk cells to nanoscale surface analysis. The electrochemical signatures of nucleation at a current collector/SE

interface are compared, indicating a stark difference in the Faradaic efficiency for Li plating between the SE materials. Specifically, Li nucleation and growth occur rapidly in the LPSCl system, while the Faradaic yield is dominated by continuous SEI formation in LGPS.

The mechanisms behind these differences are analyzed using operando video microscopy and operando X-ray photoelectron spectroscopy (XPS) to probe the chemical evolution of the SEI and the initial nucleation of Li metal. Operando imaging of the anode-free current collector is synchronized with the cell voltage traces, which allows for observation of SEI formation and Li metal plating and direct correlation of these reaction pathways with the corresponding electrochemical signatures. This is complemented by operando XPS analysis, which reveals chemical differences on the SE surface during dynamic SEI evolution, and highlights the evolution of distinct SEI components in the two SE systems. The XPS analysis also provides chemical confirmation of the earlier onset of Li metal nucleation on the SE that forms a stable SEI (LPSCl). Together, these results help elucidate the mechanisms behind SEI growth in anode-free SSBs by directly contrasting the differences between stable and unstable SE systems.

Experimental Section

Preparation of Solid Electrolyte

All air-sensitive materials were handled in an Ar-filled glovebox (MBraun) with oxygen and moisture levels maintained below 0.5 ppm. $Li_{10}GeP_2S_{12}$ (LGPS) powder and Li_6PS_5Cl (LPSCl) powders were used as received (MSE Supplies). Bulk pellets (2 mm thick, 6 mm diameter) were cold pressed to 520 MPa and relative densities were measured to be ~90%. To measure the ionic conductivity, Mo electrodes were sputtered onto both sides of the pellet and electrochemical

impedance spectroscopy was performed using a Biologic SP-200 potentiostat (Figure 4.1). The measured ionic conductivities were 4 mS/cm and 2 mS/cm for LGPS and LPSCl respectively.

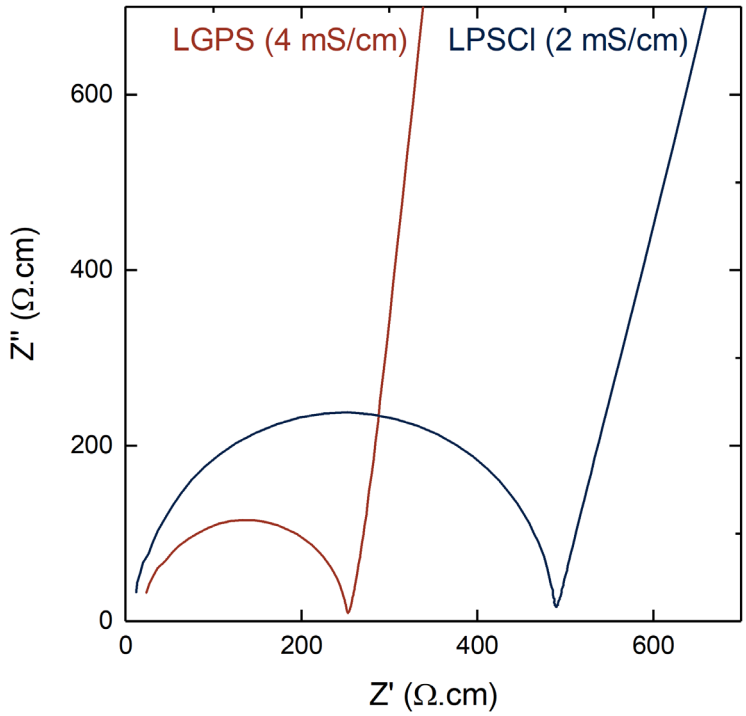

Figure 4.1. Nyquist plot of Mo/SE/Mo cells. Ionic conductivity measurements of LGPS and LPSCl after cold pressing.

Li/SE/Cu Half Cell for Electrochemical Analysis (Figure 4.2A)

LPSCl pellets (1 mm thick, 6 mm diameter) were fabricated from powder by cold pressing at 26 °C. 49 mg LPSCL powder was first soft pressed to 100 MPa, after which a battery-grade Cu foil current collector (10 µm thick, Oak Mitsui Inc.) was placed on one side and the stack was pressed to 520 MPa. After compression, the Cu remained adhered to the SE surface.

After pellet fabrication, Li metal electrodes were prepared from Li foil (750 µm thick, Alfa Aesar). The Li foil surface was scraped and flattened to remove surface layers and achieve a shiny metallic surface. Li was added to the SE/Cu stack and the cell was pressed to 17.7 MPa to

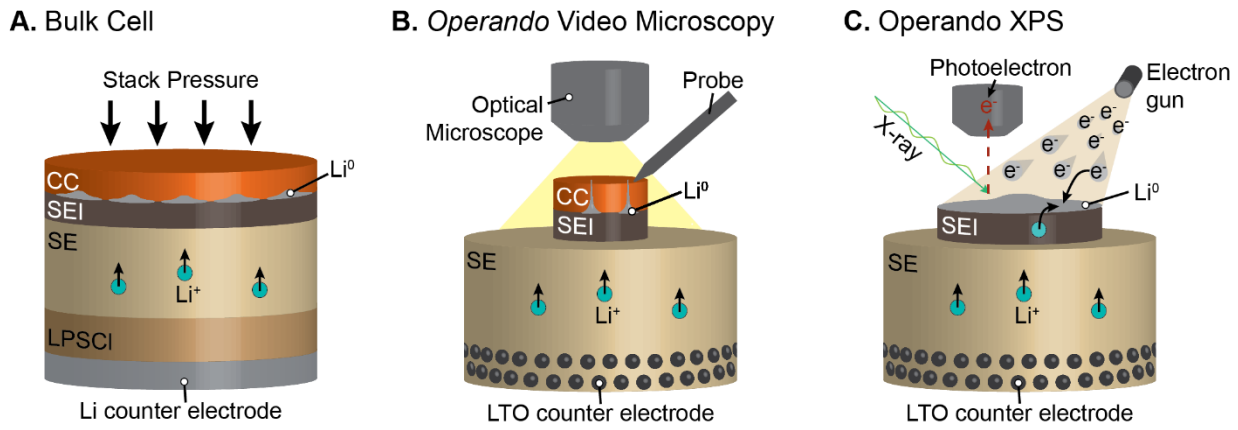

Figure 4.2. Cell configurations. In each configuration Li is plated from the counter electrode up to the anode-free surface at the top of the cell. A) bulk cell with a Cu foil current collector at the anode-free interface. When studying the anode-free interface in LGPS, a thin layer of LPSCl was added at the Li counter electrode interface. B) Operando video microscopy cell with a sputtered Mo current collector at the anode-free interface. C) Operando XPS cell using an electron gun as a virtual electrode.

form the Li/SE interface (Figure 4.2A). The pressure was then decreased to 7 MPa and the cell was held at open circuit conditions for 1 hr before cycling. Bulk Li/SE interfaces were also analyzed in Li/LPSCl/Li symmetric cells cycled at 100 μA/cm^2 and no discernible increase in polarization of LPSCl was observed over 50 cycles (Figure 4.3).

In contrast to LPSCl, Li/LGPS/Li symmetric cells that were cycled showed increasing polarization during cycling (Figure 4.3), which is attributed to continued electrolyte decomposition in LGPS.[5] Therefore, in order to avoid convolution in the voltage trace of the (anode-free) working electrode with side-reactions at the bulk Li foil counter electrode, an LPSCl interlayer was used between the Li and LGPS (Figure 4.2A). LGPS pellets were fabricated in a similar manner to the LPSCl samples. 54 mg of LGPS powder (1 mm) was pressed at 100 MPa and then the Cu current collector was added to one side. 25 mg (0.5 mm) of LPSCl powder was then added to the opposite side of the LGPS pellet (the Li metal side, Figure 4.2A). The whole stack was then pressed to 520 MPa to densify the SE and adhere the Cu to the anode-free surface.[5]

Electrochemical cycling was performed using an Arbin LBT cycler at room temperature. In each cycle 0.5 mAh/cm^2 Li was plated at 10 µA/cm^2 on the Cu current collector followed by stripping at the same current until a 0.1 V cutoff. Post-mortem optical microscope images of the interface were taken in a glovebox using a Keyence VHX-7000 digital microscope. Cyclic

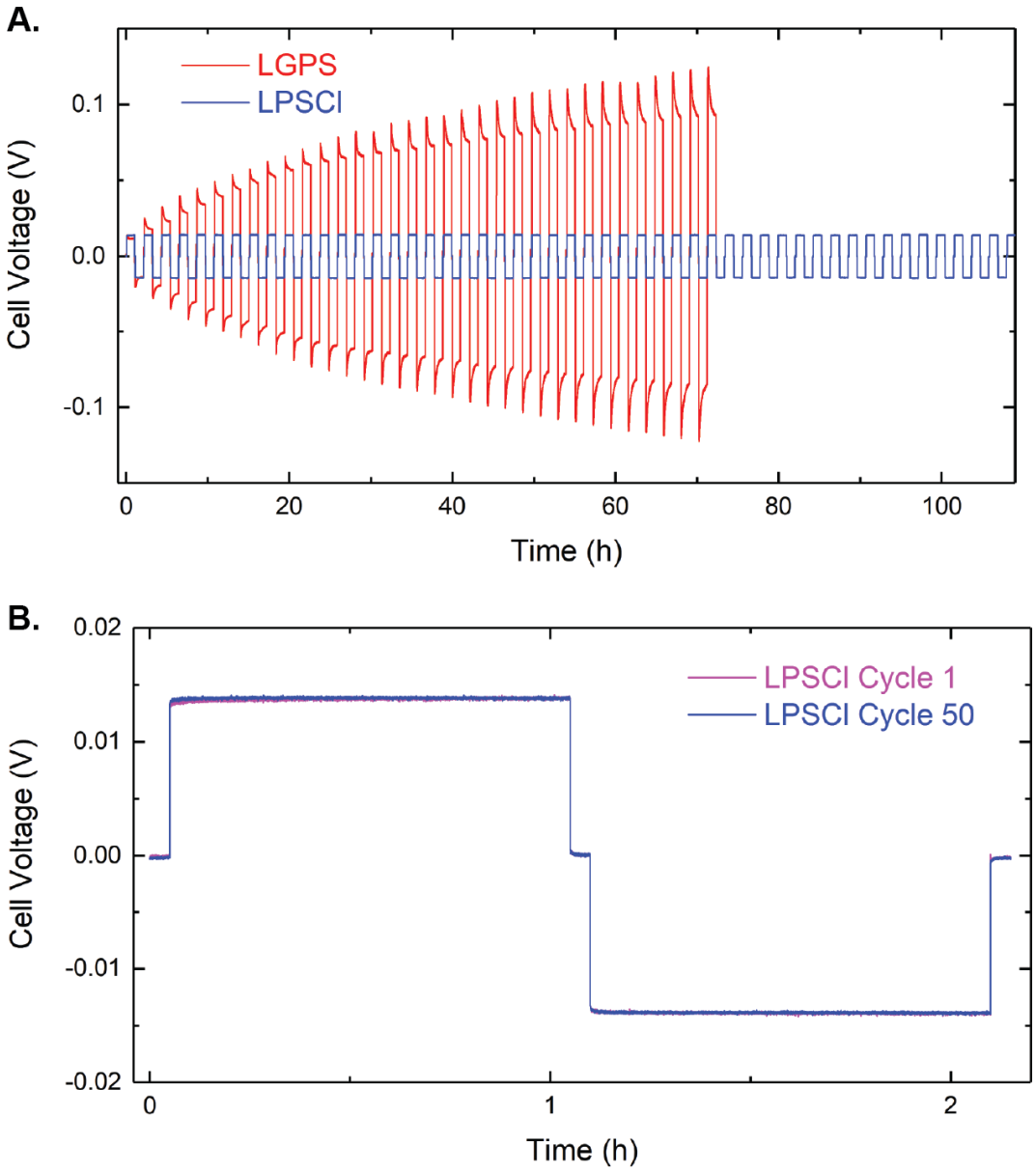

Figure 4.3. Li-Li symmetric cell cycling. A) LGPS and LPSCl stability during cycling. For each cell, 0.1 mAh/cm^2 was cycled at 0.1 mA/cm^2. The LPSCl sample exhibits stable cycling throughout the experiment, indicating minimal SEI growth. In contrast, the LGPS sample shows a continuing increase in cell impedance throughout cycling. B) Overlay of the 1st and 50th cycle in LPSCl showing negligible evolution in the voltage trace

voltammetry (CV) was also performed using a Biologic SP-200 potentiostat. The scan rate was 1 mV/s from the OCV of 1.75 V down to -0.05 V and back (Figure 4.6).

LTO/SE/Mo Half Cell for *Operando* Video Microscopy (Figure 4.2B)

In the operando video microscopy and operando XPS experiments, an LTO composite counter electrode was used instead of Li foil (Figure 4.2B, C). This allowed the operando cells to be cycled without the stack pressure requirements of the Li metal counter electrode. LTO powder was pre-lithiated and prepared as described in Davis et al.[5] LTO electrodes obtained from the CAMP facility at Argonne National Laboratory were lithiated in Li-LTO coin cells to a cutoff voltage of 1.53 V (just before the end of the LTO voltage plateau) using a 1 M LiPF6 in 1:1 EC:EMC (Soulbrain) liquid electrolyte. Lithiated LTO was removed from the current collector and combined with LGPS powder, and carbon black conductive additive (C-nergy Super C65) in a 3:6:1 (wt%) ratio and mixed with a mortar and pestle for 10 min to form composite LTO electrode powder (c-LTO). Either 49 mg of LPSCl or 54 mg of LGPS (enough for a ~1 mm thick pellet) was initially pressed to 100 MPa and then composite LTO electrode powder was added to one side. The SE/c-LTO stack was then densified by pressing to 520 MPa for 10 min. 300 nm thick, 1 mm diameter Mo current collectors were deposited onto the SE surface by DC sputtering using a glovebox-integrated sputtering system (Angstrom Engineering Nexdep). Circular working electrodes were patterned during the sputtering process using a shadow mask.

Electrochemical measurements were taken using a Biologic SP-200 potentiostat at 26 °C. Synchronized plan-view optical visualization was performed using a custom-built visualization platform (Figure 4.2B).[5] A 10 μA/cm^2 Current was applied by contacting a probe to the Mo surface. LPSCl were taken with a Keyence VHX-7000 digital microscope and LGPS videos were taken with an Opto Engineering RT-HR-6M-71 telecentric lens.

LTO/SE Half Cell for *Operando* XPS (Figure 4.2C)

c-LTO/SE cells were prepared in the same manner as the *operando* video microscopy cells, without adding a Mo current collector (Figure 4.2C). Samples were transferred into the XPS analysis chamber via a Ar glovebox-integrated load lock, which eliminated any artifacts air exposure.

Operando XPS was performed with a Kratos Axis Ultra XPS with an 8-channel detector. A monochromated Al-Kα x-ray source at 10mA emission current at 12 kV was used for all scans. Low-energy electrons (3 eV) from the charge-neutralizer were used to drive current as a virtual electrode following a method described in previous reports[5,40,87]. A neutralizer filament current of 2.25 A was used, which corresponded to a current density of 5-15 μA/cm^2 on the pellet surface.

Core-scans for each element of interest were collected using a pass energy of 40 eV. Compositional analysis and fitting were performed using the CasaXPS software package, utilizing the built-in sensitivity factors for Kratos Axis XPS systems. All scans were energy calibrated such that the S 2p 3/2 of Li_2S was 162.5±0.1 eV. Other component peak assignments were predominantly based on those in previous reports [40,54,87]. To enable fitting of each core scan, constraints were applied to fix component ratios, spacings, and areas dependent on those observed in other core scans.

To prevent pre-mature short-circuiting, an aluminum cover was used to block electrons from reaching the sides of the pellet. This cover was shorted to the XPS stage and sits approximately 100 μm above the surface of the pellet, but does not contact the surface, to avoid shorting.

To enable fitting of each core scan, constraints were applied to fix component ratios, spacings, and areas dependent on those observed in other core scans. The ratio of Li_2S to LPSCl or LGPS was calculated based on peak area from the S 2p core scans. These ratios were then used to constrain the ratios of the corresponding components in the Li 1s core scan. The relative areas (corrected by the relative sensitivity factors) of the P 2p components for Li_3P and Li_xP and S 2p of Li_2S were used to fix the ratio between Li_2S and Li_xP components in Li 1s. The area of the Li oxide component of the Li 1s was constrained based on the area of the Li oxide component of the O 1s peak. The ratio between these components was calculated based on a standard sample for Li oxide that is a surface layer on Li metal (as is the case here). A piece of bulk Li foil (99.9%, Alfa Aesar) was sputter-cleaned to remove the surface carbon layer. The resulting surface was composed almost entirely of Li and O, with approximately a 2:1 ratio. The peak area ratio between the Li 1s and the O 1s of this sample (0.0716) was then used to constrain the area of the Li oxide component of the Li 1s for all scans in this work. Finally, the ratio of Ge^0 to Ge^{4+} from the Ge 3d core scan was used to fix the same ratio in the Ge 3p to help deconvolute the Ge 3p peaks from the P 2p.

Results and Discussion

Bulk Electrochemistry

Bulk Li/SE/Cu cells (Figure 4.2A) were used to probe the differences in SEI formation at the anode-free (Cu/SE) interface for both LPSCl and LGPS. A constant current density of 10 $\mu A/cm^2$ was applied during charge and discharge. Figure 4.4 compares the voltage traces during the initial Li plating cycle. The relatively slow current density of 10 $\mu A/cm^2$ allowed for a careful examination of SEI formation and the transition in reaction pathways from SE reduction

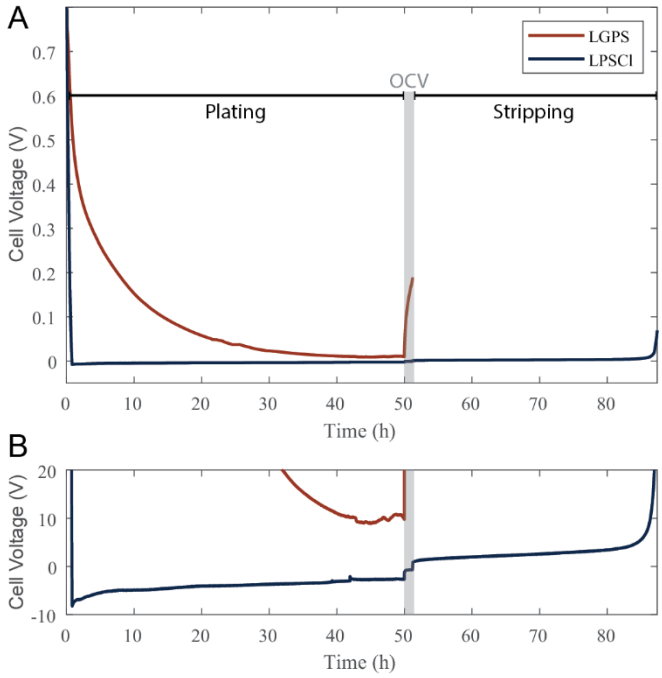

Figure 4.4. Bulk cell voltage traces. A) Full voltage traces. B) Zoomed in view. In the LPSCl cell the voltage rapidly drops below 0 V, indicating Li plating. In the LGPS the voltage never reaches 0 V.

to Li plating.[5] This current density also allowed for a direct comparison with the *Operando* XPS and video microscopy experiments. The relative trends in SEI formation between LGPS and LPSCl were also consistent at a higher formation current density of 100 μA/cm^2 (Figure 4.5). To further probe differences in SEI formation CV was also performed on analogous cells (Figure 4.6).

LPSCl. In the LPSCl sample, the cell voltage quickly decreases from the OCV during the initial SEI formation. The cell voltage drops to below 0 V and a nucleation peak is observed at 51 min (8.5 μAh/cm^2 charge passed), indicating the onset of Li metal plating. The peak then decays to a stable voltage as Li continues to plate out. After the current is stopped, the OCV jumps to 0 V and remains stable, confirming the presence of Li metal at the Cu/LPSCl interface. This same voltage behavior was exhibited in the subsequent cycle, further illustrating the

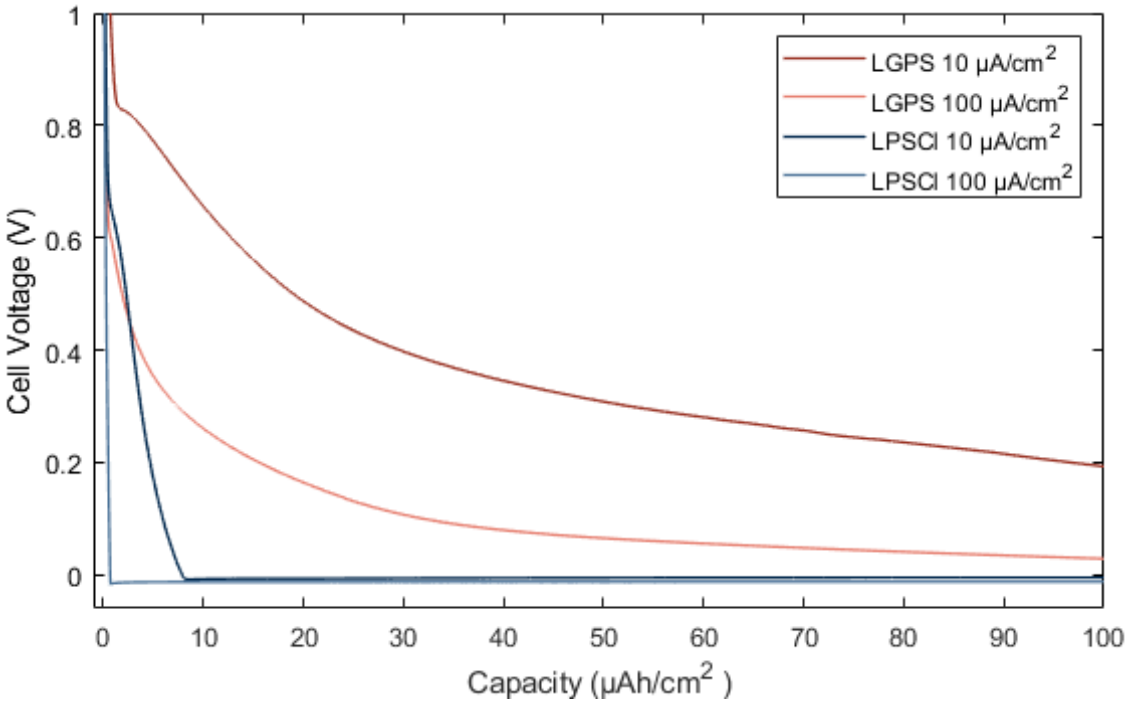

Figure 4.5. Bulk anode free cell cycling at different rates. Voltage traces of LGPS and LPSCl Li/SE/Cu cells at 10 and 100 μA/cm^2. The trend showing increased SEI formation in the LGPS sample is consistent at both current densities.

stability of this interface. Postmortem optical microscopy of the Cu/LPSCl interface shows minimal evidence of electrolyte decomposition byproducts on the surface and confirms the presence of large Li metal deposits (Figure 4.7).

After a 30 min OCV rest, the current was reversed. Initially, a stable voltage plateau is observed as the Li is stripped from the interface. After most of the Li has been stripped, the voltage rapidly increases until the cutoff voltage is reached.

LGPS. In contrast, during the first half cycle the LGPS sample voltage drops significantly more slowly as the SEI is continuously formed. Throughout the entire cycle the cell voltage never drops below 0 V, and no Li nucleation peak is observed even after 50 h (0.5 mAh/cm^2). During the subsequent OCV rest, the voltage rapidly increases, indicating that no metallic Li is present at the interface. Therefore, no stripping of Li metal was possible in the LGPS cell. This is direct evidence of the lower Faradaic efficiency for Li plating in LGPS

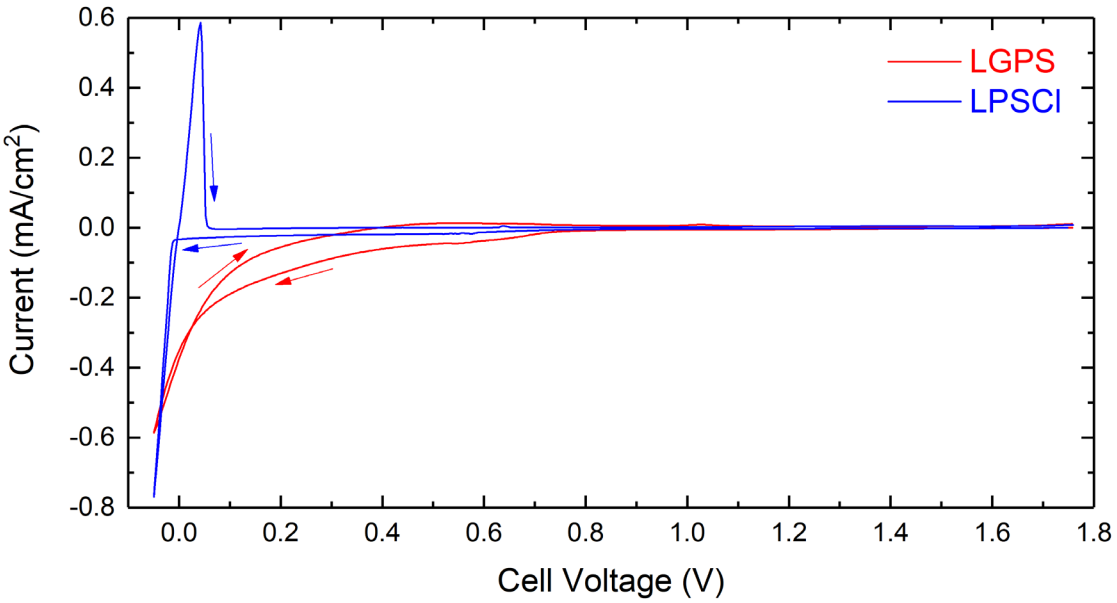

Figure 4.6. Cyclic Voltammetry on bulk anode free cells. (LPSCl) As the voltage is decreased from the OCV (1.75 V), only a slight negative current is obverved above 0 V, indicating only minimal SEI formation. Past 0 V, a significant current is observed due to Li plating. As the sweep direction is reversed, the current switches direction as soon as 0 V is passed indicating the plated Li metal is being stripped. After all Li is stripped, the current drops back close to 0. (LGPS) As the voltage decreases below 0.8 V, the LGPS sample shows significant current corresponding to SEI formation which continues throughout the scan. As the scan direction is reversed, the current remains negative implying continued SEI formation and no reverse current to indicate stripping of Li metal.

compared to LPSCl, as discussed in further detail in the operando XPS section. The continual rise in OCV further suggests that the SEI continues to evolve even after the applied current has stopped. This influences the voltage trace during the subsequent charge cycle, where an increased cell polarization is observed.

Postmortem optical microscopy analysis of the interface shows significant SEI formation (dark spots). This has been previously attributed to volumetric expansion of LGPS as reductive by-products are formed, which leads to mechanical degradation of the interface.[5,80] Degradation is clearly visible on both sides of the interface, in the form of pits on the LGPS surface and

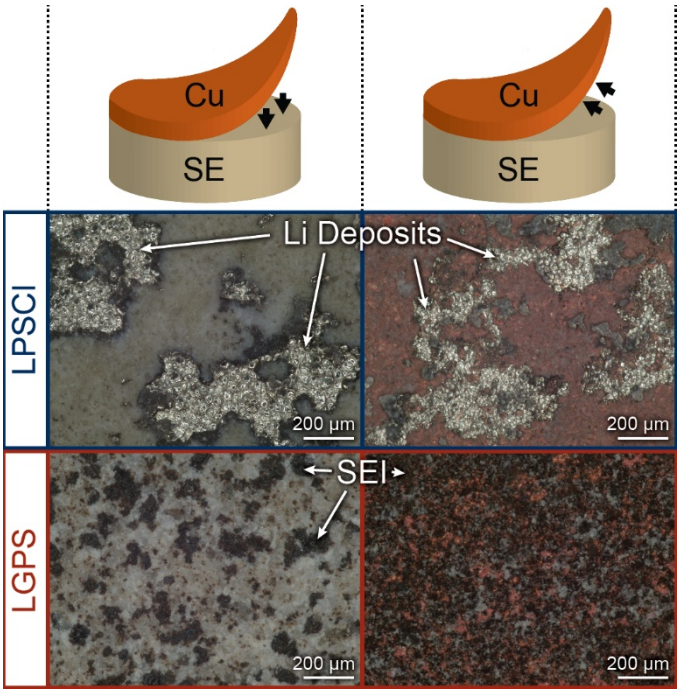

Figure 4.7. Bulk cell optical microscopy. Optical microscopy of the SE and Cu surfaces after the first half cycle. In the LPSCl sample, minimal SEI is observed and Li deposits are visible on both surfaces. In the LGPS sample, both surfaces have significant SEI byproducts and mechanical degradation. No Li is visible on the surface.

detached SEI and LGPS byproducts that remain adhered to the Cu after removing the current collector.

Operando Video Microscopy

To further probe the SEI formation and Li plating behavior, *operando* video microscopy was performed on anode-free cells with sputtered current collectors that were patterned on the SE surface (Figure 4.2B). In the LPSCl sample, during the the first 34 µAh/cm^2 of charging the cell voltage decreases to a plateau at -1.58 V (Figure 4.8A). This corresponds to the open-circuit voltage of the lithiated LTO vs. Li metal (-1.54 V) and indicates that metallic Li has formed at the working electrode. [5] During the initial voltage drop, a uniform color change is visible across the CC surface as the SEI is formed. When the voltage reaches the plateau, Li whiskers nucleate

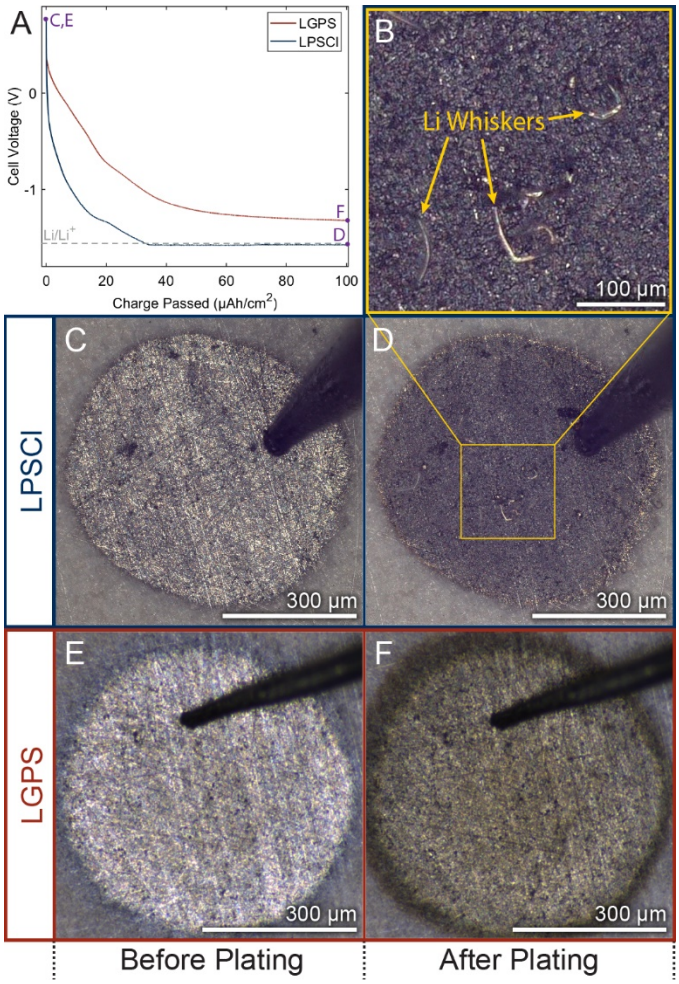

Figure 4.8. Operando video microscopy images and voltage traces. A) Top-down microscope images of the circular Mo current collector on the SE both before and after plating. After images show SEI formation in both samples, however, Li whiskers are only visible on the LPSCl sample. B) Sample voltage traces confirming that only the LPSCl sample goes below the Li/Li^+ potential and begins plating Li. In the video, Li whisker nucleation is confirmed to occur when voltage drops below the Li/Li^+ potential.

and mechanically break through the current collector. Throughout the plateau, the Li deposits continue to grow and extrude through the current collector (Figure 4.8B,D).

Consistent with the bulk Li/SE/Cu voltage traces, in the LGPS sample the voltage drops more slowly. Within the time scale of the experiment never drops below −1.54 V. Throughout the experiment, significant color and morphological changes are visible that extend beyond the WE border, indicating a larger extent of SEI formation than is seen in the LPSCl sample (Figure

4.8F). This provides visual evidence that the Faradaic efficiency is lower in anode-free cells with LGPS, since the reaction pathway never transitions from SEI formation to Li plating.

Operando X-Ray Photoelectron Spectroscopy

To compliment the optical visulalization experiments, *operando* XPS was performed to probe the chemical evolution of the anode-free surface during SEI formation. In the *operando* XPS technique employed here, a "virtual electrode" is formed by using an electron gun to provide a flux of electrons to the SE surface (Figure 4.2B).[5,40,87] Similar to a cell with a physical current collector, as charge builds up on the SE surface, a potential gradient is generated across the cell. Li+ ions are pulled from the grounded counter electrode and drawn up through the SE to the exposed anode-free surface. At the exposed surface, the Li+ ions combine with the electrons from the electron gun, driving reduction reactions. Initially, the reduction products are composed of SEI species, and after a sufficient amount of charge is passed, the reaction pathway transitions to plating of metallic Li. Therefore, operando XPS provides insight not only into the dynamic evolution of SEI formation in anode-free cells but also into the chemical reaction pathways that determine the Faradaic efficiency of Li plating.

At intervals throughout the experiment, XPS spectra are collected to probe the chemical composition of the surface. Figure 4.9 shows the XPS spectra for LPSCl and LGPS samples (Li 1s, S 2p, P 2p, and Cl 2p or Ge 3d respectively). Figure 4.10 shows the corresponding peak fitting.

S and P core spectra. In both the LPSCl and LGPS samples, the evolution of the S and P peaks are similar. The primary component of the S 2p core spectrum shifts from an initial state of ~164 eV (associated with the PS_4 tetrahedra in the SEs) to a lower binding energy of ~162.5 eV (Li_2S) (Figure 4.9A,E; Figure 4.10A,E). The peak intensity then slowly decays as it is buried

underneath subsequent species that form on the top surface. Similarly, the P 2p peak shifts from an initial state of ~134.5 eV (also associated with the PS_4 tetrahedra in the SE) to binding energies (BEs) associated with Li_xP (~133-130 eV) and then to ~128.5 eV, corresponding to Li_3P (Figure 4.9B,F; Figure 4.10B,F). The P peak then decays as it is similarly buried by subsequent products.

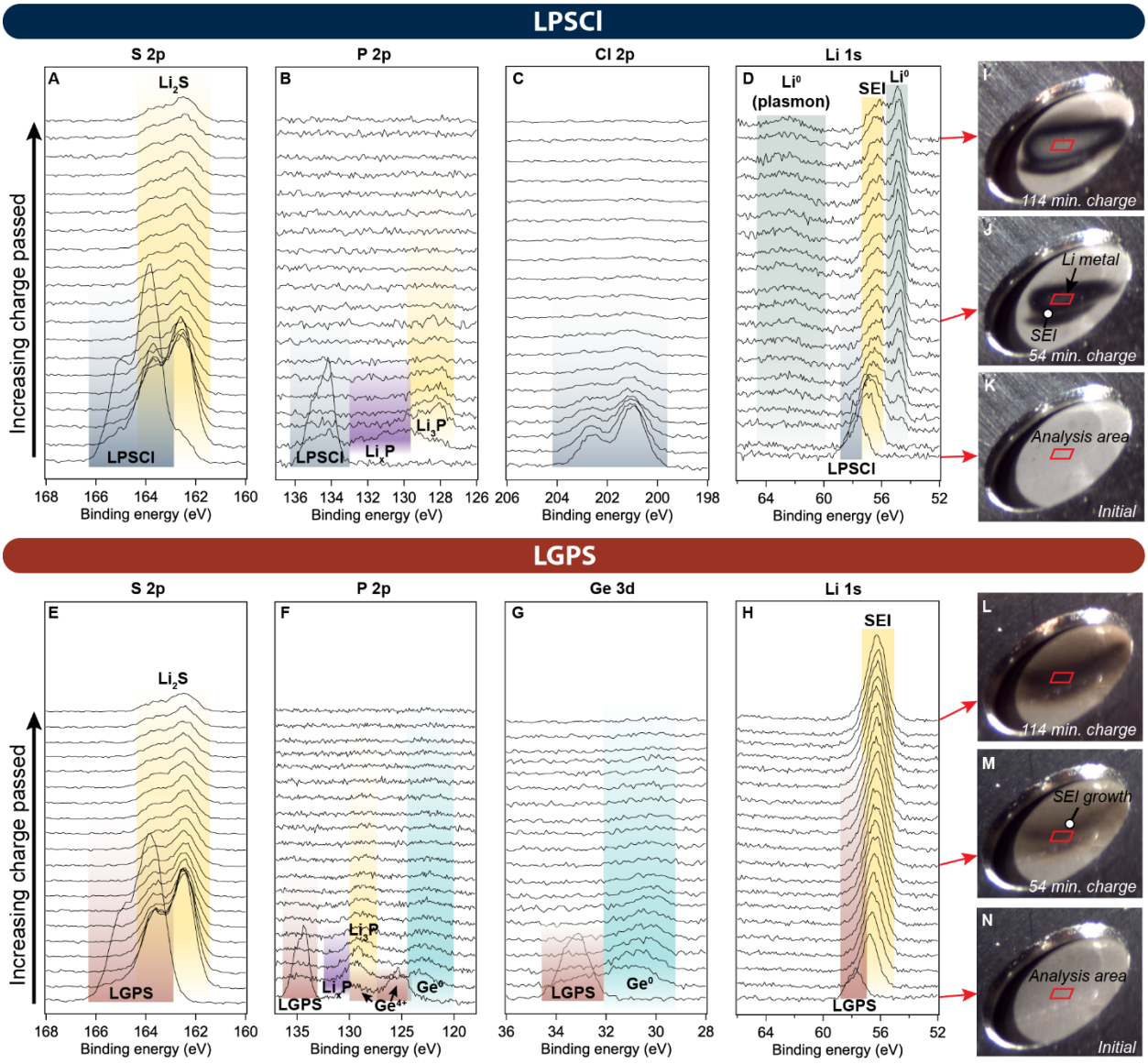

Figure 4.9. Operando XPS core scans and corresponding optical microscopy. A-D and E-H) Core scans throughout the experiment for the LPSCl and LGPS samples respectively, with each scan corresponding to an addition 6 min. of charging. I-K and L-N) Corresponding optical images of anode-free surface throughout experiment.

Cl/Ge core spectra. In the Cl/Ge and Li core spectra, significant differences are observed between the LPSCl and LGPS samples. In LPSCl, no change in the BE of the Cl peaks is observed, implying that the bonding environment of the Cl is not changing significantly (Figure 4.9C, 6C). In contrast, the Ge peak in LGPS quickly shifts from ~33 eV for the Ge in

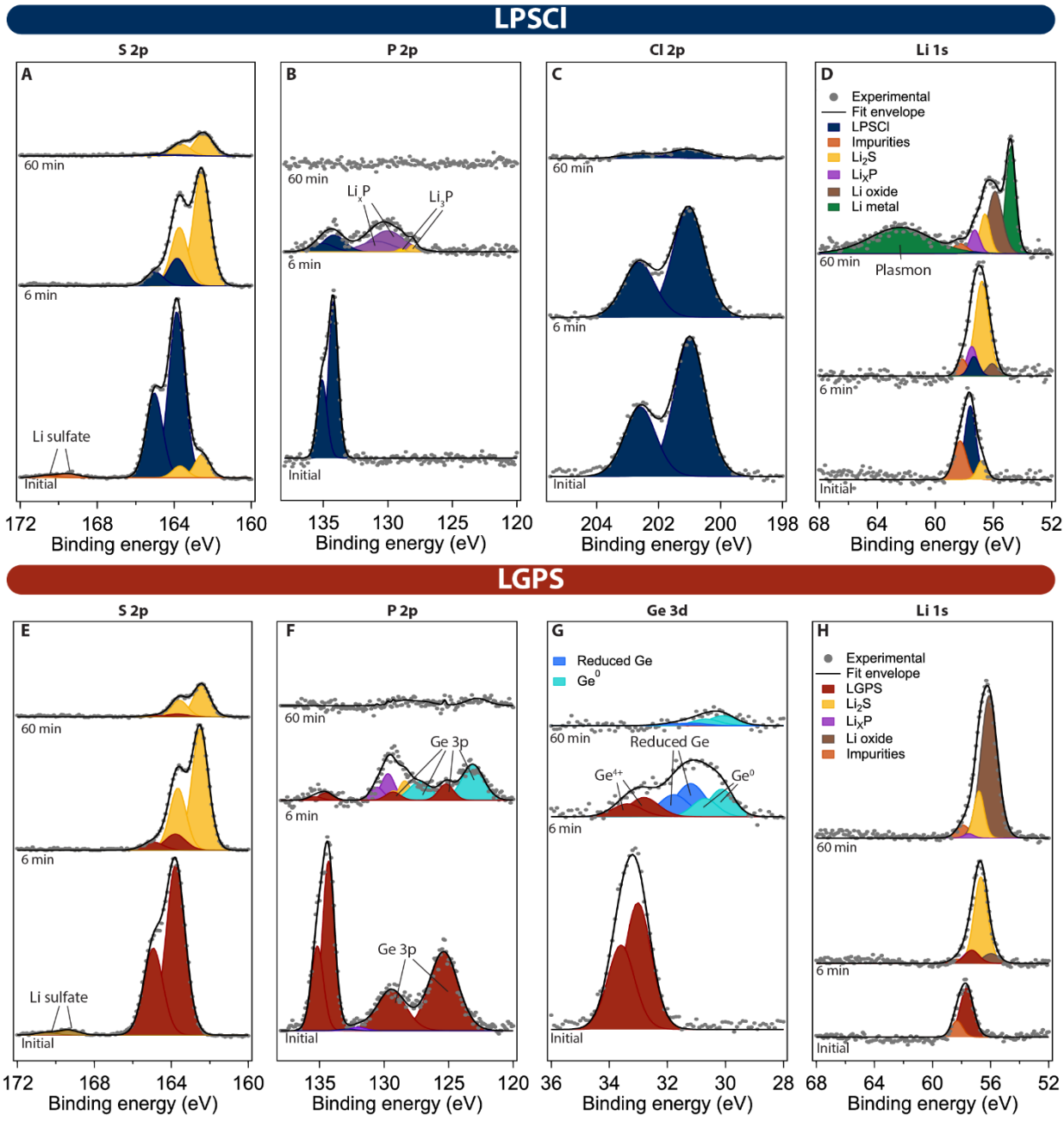

Figure 4.10. Operando XPS peak fitting. A-D) S 2p, P 2p, Cl 2p, and Li 1s peak fits for LPSCl. E-H) Corresponding peaks for LGPS with Ge replacing Cl. Peaks are shown for 0, 6 and 60 min of plating.

LGPS to ~31 eV, corresponding to the formation of a Li-Ge alloy (Figure 4.9G; Figure 4.10G). Similar to the S and P peaks, the Cl and Ge peaks decay over time as they are buried underneath subsequent product species. The susceptibility of Ge to reduction, and the electronic conductivity of the resulting byproduct (Li-Ge alloy), results in a pathway for electronic transport to the bulk SE-SEI interface. This causes further SEI formation, which strongly influences the relative differences in performance between LGPS and LPSCl.[20,21]

Li core spectra. In LPSCl, the primary Li peak initially shifts from ~58 eV to ~57 eV as the SEI forms. However, within the first 20 min, a Li^0 peak at ~55 eV and the corresponding plasmon peak begin to grow, indicating that Li metal has begun to plate out on the LPSCl surface (Figure 4.9D; Figure 4.10D). The Li peak in the LGPS sample initially follows the same trend as the LPSCl where it is reduced to an SEI peak. However, in contrast to the LPSCl sample, a Li^0 peak does not appear, and instead the SEI peak continues to grow until the whole surface is dominated by SEI coverage (Figure 4.9H; Figure 4.10H). This difference is also apparent in *in situ* optical images captured concurrently with the XPS spectra. In the LPSCl (Figure 4.9I-K), a silver-colored patch of metallic Li appears early in the charging process. The LGPS (Figure 4.9L-N) never reaches this point, and the dark discoloration continues to grow throughout the charge.

In summary, the *operando* XPS analysis provides complementary information to the bulk electrochemistry and the *operando* video microscopy experiments. In particular, the low Faradaic efficiency in the LGPS samples is shown to correspond with continuous SEI formation throughout the experiment. In contrast, in the LPSCl samples the interface stabilizes relatively after which Li metal plates out at the anode-free surface.

One way to rationalize these trends in Faradaic efficiency is to consider the fractional distribution of total current among the available reaction pathways at the electrode/electrolyte interface, including SEI formation (iSEI), Li metal nucleation (inuc), and growth of the Li metal deposits (igrowth) (Figure 4.11A). Under galvanostatic (constant current) conditions, the summation of these values equals the total current. The magnitude of the fractional current associated with each pathway depends on the time-dependent impedance of that pathway, where the current will "follow the path" of least impedance. Analogous to Li nucleation and growth in liquid electrolytes,[13] these changes in impedance can be influenced by both the kinetic rate of each charge transfer reaction pathway and changes in the interface area, morphology and/or transport properties.

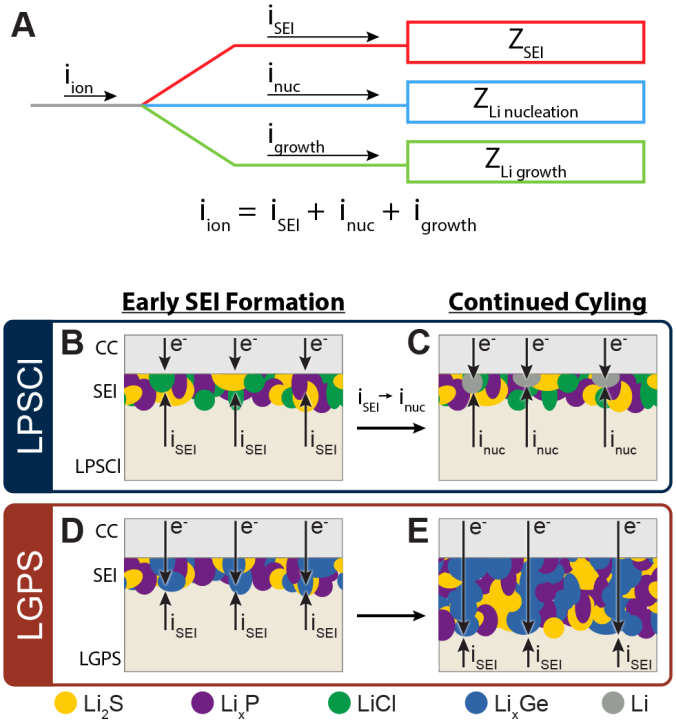

Figure 4.11. Li Reaction Pathways. A) Schematic showing possible Li reaction pathways. B-E) Schematic showing differences between SEI composition and the unstabilizing impact of the electronically conducting Li_xGe phase in the LGPS sample.

In the LPSCl sample, early in the cycle, the dominant reaction pathway is SEI formation (Figure 4.11B). The reduction of the SE initially occurs at more positive potentials than 0 V vs Li/Li+, as shown in the cyclic voltammetry data (Figure 4.6). As the Li concentration in the SEI increases, the voltage drops. Owing to the electrically insulating nature of the SEI components in LPSCl (which were identified using *operando* XPS, Figure 4.9), when the SEI becomes sufficiently thick and continuous, electronic transport is blocked to the SEI/SE interface. Therefore, all charge transfer reactions must occur at the current collector/SEI interface (Figure 4.11C). Once the fully reduced phases of the SEI components (Li_2S, Li_3P, LiCl) are formed, the impedance associated with continued SEI formation increases significantly, and therefore the dominant reaction pathway transitions from SEI formation to Li nucleation and subsequent growth (Figure 4.11C). Evidence of this transition is provided in both the *operando* optical microscopy (Figure 4.8) and *operando* XPS (Figure 4.9) results.

In contrast, in the LGPS sample, reduction of the SE involves the formation of a Li-Ge alloy, which imparts electrically conductive pathways through the SEI layer (Figure 4.11D). This allows for continual reduction reactions to occur at the SEI/SE interface, which propagates deeper into the bulk SE (Figure 4.11E). Therefore, the transition in reaction pathways to Li plating never occurs because the impedance associated with the SEI formation pathway remains sufficiently low throughout cycling. The low impedance of the SEI pathway is maintained by the continual increase in interfacial area between the conductive Li-Ge constituents and the "fresh" SE that has not been reduced (Figure 4.11E). Evidence of this continual SEI formation without a transition to Li nucleation is provided in both the *operando* optical microscopy (Figure 4.8) and *operando* XPS (Figure 4.9) results.

Conclusion

In this study, a multi-modal *operando* analysis was employed to provide a direct comparison of the differences in SEI formation and Li plating between a sulfide SE that forms an electrically conducting SEI (LGPS) and one that forms an electrically insulating SEI (LPSCl). Anode-free cell configurations were probed using ex situ optical microscopy, *operando* video microscopy, and o*perando* XPS. For LPSCl SEs, after initial SEI formation, the interface stabilizes and Li metal plating initiates. In contrast, for LGPS SEs, the interface does not stabilize and the SEI continues to grow throughout the charging process. *Operando* XPS analysis of the SEI components demonstrates the dynamic evolution of SEI formation in the two SEs. Specifically, the formation of LiCl in LPSCl and a Li-Ge alloy in LGPS result in dramatic differences in SEI formation dynamics. By integrating the observations from this multi-modal analysis, it can be concluded that the transition in reaction pathways from SEI formation to Li plating determines the Faradaic efficiency in anode-free SSBs.

These results have significant implications on the energy density and cycle life of sulfide SSBs, particularly in anode-free configurations. Because the Li reservoir in anode-free configurations comes entirely from the cathode, Faradaic inefficiency in the first half cycle directly reduces energy density. As a result of this loss in Li inventory, SEs such as LGPS are impractical for use in anode-free cell configurations, unless this instability can be addressed. In contrast, LPSCl exhibits significantly higher Faradaic efficiency and correspondingly minimal Li loss during the initial SEI formation (<30 uAh cm^{-2} which is <1% of a standard 3 mAh cm^{-2} electrode). Moving forward, other sources of Coulombic inefficiency, including dead Li formation and any continual SEI formation after Li plating must also be addressed to enable anode-free SSBs, which are important areas of focus for future studies.[14,22,101]

Chapter 5

The Effects of the Physical Properties of Li on the Critical Current Density

Adapted with permission from Kinzer, B.; Davis, A. L.; Krauskopf, T.; Hartmann, H.; LePage, W. S.; Kazyak, E.; Janek, J.; Dasgupta, N. P.; Sakamoto, J. Operando Analysis of the Molten Li|LLZO Interface: Understanding How the Physical Properties of Li Affect the Critical Current Density. *Matter* **2021**, *4* (6), 1947–1961.

Chapters 3 and 4 focused on electrochemical degradation and SEI formation at sulfide SE/Li metal interfaces. In addition to SEI formation, the mechanical evolution of the interface plays a critical roll in cell degradation and shorting. In this Chapter, we use LLZO, a ceramic electrolyte with good stability vs. Li metal, to probe mechanical fracture and filament nucleation in the SE.

Recently, stabilizing Li during cycling using bulk-scale SEs has attracted interest.[102–105] High cycling stability and Coulombic efficiencies have been shown at lower current densities (< 1 mA/cm^2).[106–108] However, charging at higher rates causes Li filament penetration into the SE leading to short circuiting and cell failure.[25,109–112] The current density above which Li penetrates a SE is commonly referred to as the critical current density (CCD).[113]

Several studies have focused on elucidating the mechanisms by which Li and Na metals, relatively soft materials, can penetrate significantly stiffer ceramic SEs. Two main mechanisms behind filament formation and propagation have been proposed.[23,24] In Mechanism 1, current focusing in defects or surface flaws leads to an increase in localized mechanical stress, which causes SE fracture.[25–29] In Mechanism 2, electronic defects within the SE lead to the internal nucleation of Li/Na metal in the SE.[27,30,31] Evidence of both of these mechanisms has been shown in various SE systems, and the results indicate that the role of each mechanism varies based on the interfacial resistance and the properties of the SE such as ionic and electronic conductivity.[30,113,114] In addition, the mechanical properties of Li and Na metals are thought to play an important role.[26,113,115–119]

Direct connections have been shown between the CCD and the cell temperature,[113] pressure,[115,117,120] and amount of charge passed.[121] In particular, increasing the cell temperature below the melting temperature of Li results in an exponential increase in the CCD.[113] At temperatures above the melting point of Li (180 °C), a molten Li electrode is formed leading to an even greater increase in the CCD. A recent study demonstrated a molten Li|LLZO|Bi-Pb solid-state battery at 240 °C can stably cycle at 100 mA/cm^2, which is two orders of magnitude higher than room temperature solid Li|LLZO.[122] Several factors likely contribute to this increased rate capability. First, the increased ionic conductivity of the LLZO leads to less current focusing at interfacial defects.[26] Second, the liquid phase of the Li anode allows the Li to more easily flow out of cracks/defects where current focusing occurs; therefore, a higher local current density can be accommodated before sufficient pressure builds up to cause fracture of the SE. In addition to increasing the CCD during plating, molten lithium alleviates the problems with void formation during stripping that are common with solid Li cells and therefore removes the need

for stack pressure.[24,117,123] Previous studies of molten Li batteries have demonstrated stable voltage responses even after 300 cycles without stack pressure indicating that due to its lower viscosity and/or higher self-diffusivity, void formation in Li is negligible. Molten Li cells are limited by plating, rather than stripping mechanisms.[122,124,125] An increase in cell polarization indicates void formation,[117] but in this study the cell polarization decreases from linearity offering evidence of negligible void formation.

In this work, we perform a multi-modal *operando* microscopy analysis to examine the role of cell temperature and metal anode melting on filament formation and propagation and probe the mechanisms behind the change in CCD observed across the melting point. Utilizing Li|LLZO as a model system, we use custom electrochemical cells to synchronize *operando* optical and scanning electron microscopy videos with cell voltage traces. *Operando* video analysis reveals that filament formation and propagation is dominated by surface eruptions occurring in cycles of pressure build-up and release. However, in the same cell configuration using solid Li, surface extrusions are much more limited. We report the CCD of the molten Li|LLZO in-plane cell as (530 ± 140) mA/cm^2 just above the melting point of Li at 195 °C. This represents a step change in the temperature-dependent CCD of solid Li|LLZO across the melting point of Li. A mechanical model is used to probe the transition from the visco-plastic behavior of solid Li to the viscous behavior of molten Li. This transition in viscosity as well as changes in Li^0 self-diffusivity, correspond with the step change in CCD. Our results show that the mechanical properties of alkali metal electrodes play a crucial role in governing the CCD and filament formation and propagation in solid-state batteries. In addition, our results demonstrate that the molten Li|LLZO interface is stable at ultra-high current densities, which supports the potential of molten Li cells for the electric grid, where rapid response times are needed.

Results and Discussion

Synchronized Electrochemical Testing and *Operando* In-plane Li|LLZO|Li Cell Analysis

Molten metal batteries often use a tubular geometry to physically confine the molten metal, which prevents the direct optical observation of Li penetration. To overcome this challenge, we employed an in-plane cell configuration (Figure 5.1a), which allows for *operando* visualization of physical changes during molten Li plating. The model indicates that most of the interface is relatively close to the nominal current density (within a factor of <2). However, near the edges of the droplet, the local current density is even higher than the nominal, which matches similar edge effects of traditional through-plane cells.[112,126] Since CCD is an interface driven phenomenon based on local current densities, the measured nominal CCD (530 mA/cm^2) is a conservative estimate and the nominal CCD would likely be higher if the current was uniformly applied across the surface.

To measure the critical current density (CCD) using molten Li, linear sweep amperometry was conducted using in-plane symmetric Li|LLZO|Li cells. Voltage and current data were synchronized with microscopy videos (Figure 5.2a-d; see full video: Video S1). The

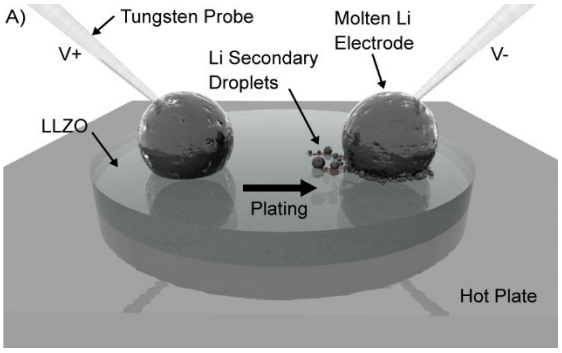

Figure 5.1. Schematic representation of the optical in-plane test setup of molten li current sweep tests.

current was increased at a rate of 2 mA/(cm^2 · s) from 0 mA/cm^2 up to 2000 mA/cm^2. Figure 5.2 shows representative voltage versus current traces for a typical test. Initially, the cell exhibits a linear response in cell polarization at relatively low current densities up to 550 mA/cm^2 (Figure 5.2a-b). However, upon increasing the current density the voltage deviates from linear behavior starting above 550 mA/cm^2 (Figure 5.2c) until the maximum current density of 2000 mA/cm^2 (Figure 5.2d).

Associated with the deviation from linear voltage response, physical changes in the molten Li electrodes were observed. Despite the highly-controlled glovebox environment (< 0.5 ppm of O_2 and H_2O), after placing the Li droplet on the LLZO surface, a thin solid shell forms on the outer surface, which is likely a result of the reactivity of the Li metal with trace background gases. Since the shell is only on the outer surface it plays no role in governing cell failure since it does not impact the Li-LLZO interface (e.g. charge transfer kinetics and viscous Li flow remain the same). As current flows, buckling of this shell is visible on the stripping (left) droplet. Little change is seen in the plating electrode at low current densities (Figure 5.2a-b). As

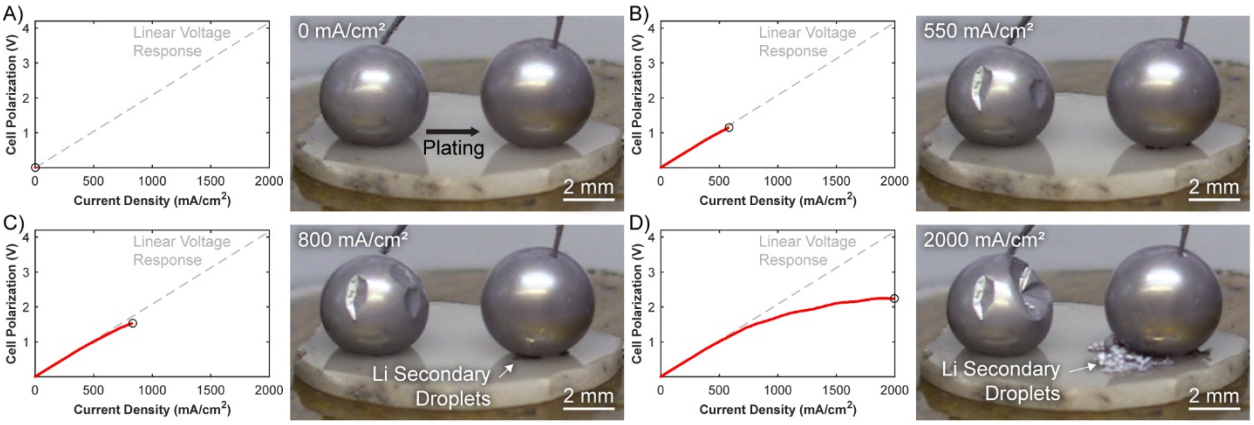

Figure 5.2. Synchronized Electrochemical Testing and *Operando* Visualization of Molten Li on LLZO. Current is swept from 0 to 2000 mA/cm^2 at a rate of (2 mA/(cm^2 · s)). From 0 to 550 mA/cm^2 the cell exhibits a linear voltage response (A-B) and the shell layer on the stripping (left) electrode begins to buckle. At 800 mA/cm^2 (C) deviation from voltage linearity is observed and secondary Li droplets appear at the base of the plating electrode. At 2000 mA/cm^2 (D) the secondary Li droplets continue to grow while the cell deviation from voltage linearity is amplified. The full video is included in Video S1.

the current density increases, secondary Li droplets are observed to extrude from the LLZO surface near the plating electrode (Figure 5.2c). The number and size of these secondary droplets increases as the current density increases (Figure 5.2d). The synchronization of the video and voltage response shows a clear correlation between the formation of secondary Li droplets and deviation from a linear voltage response.

After electrochemical testing, *post-mortem* FIB-SEM was used to analyze the secondary Li droplets. In Figure 5.3a, cross-sectional imaging reveals the source of the secondary droplet to be a crack in the underlying LLZO, through which molten Li was extruded. This matches previous observations of the solid Li|LLZO interface, where at current densities above the CCD, sub-surface cracking was observed in the LLZO during filament propagation.[112] In regions where the cracks reached the surface of the LLZO, metallic Li metal extrusions were visible. In a similar manner, we observe subsurface cracking and Li extrusion; however, due to the decreased viscosity of molten Li, significantly higher volumes of Li are extruded, forming the secondary droplets. Additional FIB-SEM images were taken on a sample where all Li droplets on the LLZO surface were removed. Cracks apparent on the LLZO top surface indicate where the secondary Li droplets were present (Figure 5.3b). Near some of the secondary droplets, Li filled pores are

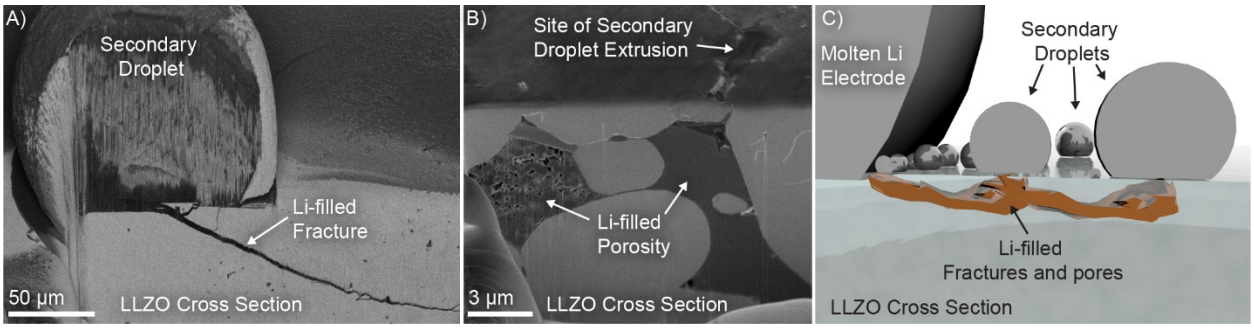

Figure 5.3. FIB-SEM Analysis of Molten Li|LLZO Cell after Current Sweep and Proposed Li Secondary Droplet Mechanism Schematic. (A) FIB-SEM showing site of Li secondary droplet extrusion. (B) FIB-SEM etched area showing Li filling pre-existing porosity leading to a Li secondary droplet surface eruption. The Li secondary droplet was removed before imaging. (C) Schematic of proposed mechanism of filament propagation and secondary droplet formation.

visible beneath the LLZO surface. The pre-existing LLZO porosity in the region shown is an order of magnitude higher (~40% porosity, estimated using ImageJ) than the nominal bulk porosity of < 3% (determined through geometric density measurement). This indicates that regions with high subsurface porosity preferentially lead to Li filament propagation, which has also been shown for solid Li|LLZO.[110] Similar to mechanisms previously described for solid Li|LLZO,[25,112] we propose the following mechanism for filament propagation and secondary droplet formation (Figure 5.3c). Initially, Li filaments nucleate at defects at the Li|LLZO interface. If the current density in the defect is sufficiently high, the LLZO will fracture due to pressure build-up.[25] According to the framework of linear-elastic fracture mechanics, the fracture criterion will depend on both a loading parameter (described by a stress-intensity factor, K_I) and the material properties of the SE (described by fracture toughness, K_{IC}). The loading parameter K_I will be determined by the energy-release rate, G, which will be affected by the geometry of the system, as well as tensile stresses at the crack tip imposed by pressure build-up in the Li metal and the elastic modulus of the SE. Therefore, the driving force for crack propagation will be impacted by the material properties of both the SE and Li, which set up an energetic balance between viscous flow of molten Li away from the crack tip and fracture of the SE. The filament propagates as Li continues to plate into the crack leading to further pressure build-up and cracking. Whenever the crack reaches the surface of the pellet or subsurface porosity, this allows for a pressure release as Li flows to form a secondary droplet or to fill the porosity. Over time, the pressure again builds up and the filament continues to propagate.

From Figure 5.2 and Figure 5.3 it is apparent that secondary droplet formation is tied to molten Li penetration as well as deviation from linear voltage behavior. Up until LLZO fracture, the cell resistance is constant leading to a linear voltage response. As the molten Li penetrates

the LLZO and secondary droplets form, the Li|LLZO interfacial contact area increases and the distance between the electrodes decreases, which leads to a decrease in the cell polarization.[112] The planar contact area between the original molten Li droplet and the LLZO surface remains almost constant throughout the test, and therefore changes in bulk droplet volume are unlikely to affect the voltage trace. Therefore, the CCD is marked by the point at which secondary droplets begin forming and the corresponding cell voltage deviates from linearity, which for this study coincided with a 2.5% change from linearity. Across 5 samples, the CCD was calculated to be (530 ± 140) mA/cm^2. This value is over 500 times the room temperature CCD of Ta-LLZO.[113] This is also in good agreement with a previous study where stable short-term cycling of a molten Li|Ta-LLZO|Bi-Pb tube cell at 500 mA/cm^2 at 240 °C was shown.[122]

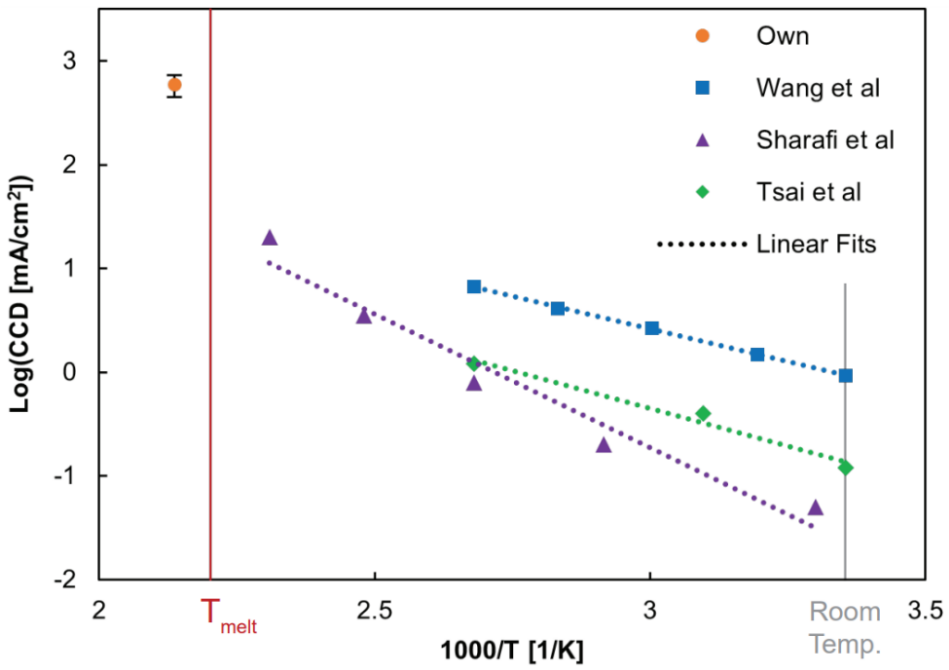

Figure 5.4. Critical Current Density (CCD) vs. Temperature for LLZO. The orange circle represents the current sweep molten Li CCD with standard deviation shown for results of this paper at 195 °C. Solid Li reference data and trend lines come from Wang et al.,[113] Sharafi et al., [124] and Tsai et al.[103]

Previous results from solid Li|LLZO show that the CCD of the solid Li|LLZO interface increases with increasing temperature.[106,113,127] In the cases of Tsai and Wang *et al*., the CCD appears to follow Arrhenius behavior as indicated by the straight lines in Figure 5.4.[9,17] It is possible that the CCD did not follow Arrhenius behavior in the case of Sharafi *et al*.,[3] because the interface resistance was relatively high (> 500 Ω/cm^2 vs. < 10 Ω/cm^2 for Wang *et al.*[17] and < ~ 50 Ω/cm^2 from Tsai *et al.*[9] who used gold as an interlayer). It is also possible that the interface resistance dramatically decreases with temperature, thus becoming negligible at higher temperatures. If this is true, the data from Wang *et al*.[17] appears to extrapolate to the highest temperature data solid Li CCD data from Sharafi *et al*.[35] Since our study also achieved < 10 Ω/cm^2 interface resistance at room temperature, it is more appropriate to use the data by Wang *et al*.[17] to extrapolate the CCD to just below the melting temperature of Li. Based off this comparison there is a roughly one order of magnitude step change in CCD across the melting point of Li (Figure 5.4), which is in agreement with Na-β" alumina studies where the CCD for solid Na just below its melting point ($T_{melt,Na}$ = 98 °C) is between 30-40 mA/cm^2 and above the melting point is closer to 1100 mA/cm^2.[27,128,129]

Many properties of the Li|LLZO system are temperature dependent and likely play a role in the Arrhenius behavior of the CCD below the melting temperature (Table 1). While electronic conductivity has been suggested as a possible failure mechanism,[27,30,31] it must be able to explain why there is an increase in CCD across the melting point of Li where the nominal electronic conductivity of LLZO lacks a step change. Since there is no evidence of isolated Li nucleation from the FIB-SEM (Figure 5.3b) and only the mechanical properties of Li exhibit a step change across the melting point of Li, mechanical mechanisms of failure are expected to be dominant.

Since liquid Li can flow more easily than solid Li, much higher current densities can be achieved before crack propagation occurs within the LLZO.

To gain insight into how propagation of molten and solid Li differs, a current sweep experiment was run in the optical cell with a Ta-LLZO sample held just below the melting point of Li (170 °C) until failure occurred. Solid Li tests failed across a wide range of current densities (15-200) mA/cm^2 making it difficult to specify a CCD for in-plane solid Li|LLZO cells at 170 °C. This wide range may be due to uneven localized melting from Joule heating during Li plating since the cell is operating just below the melting point of Li.[130] In contrast to molten Li, after failure, a solid Li filament with a smaller filament volume was observed to extrude out of the LLZO surface (Figure 5.7a). This suggests that due to the higher viscosity of solid Li, solid Li cells are less able to relieve pressure within filaments by surface extrusion, and therefore they have a higher degree of subsurface Li growth with long extended cracks than molten Li cells. This indicates that the mechanical properties of Li, such as viscosity, play an important role in governing cell failure.

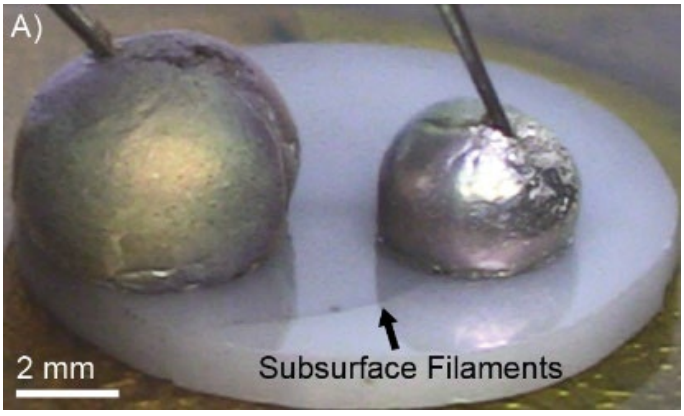

Figure 5.5. Solid Li Filament Propagation for Optical Current Sweeps. Solid Li current sweep at 170 ℃ for Ta-LLZO (Plating from left to right). Subsurface propagation dominates due to the mechanical properties of solid Li.

Derivation of Solid Li Pseudo-Viscosity

To compare the mechanical properties of Li across the melting point, we adapted previous models that use a pseudo-viscosity to describe the behavior of a visco-plastic solid, such as Li.[26] This enables the analysis of strain-rate and applied stress effects on pseudo-viscosity.[131–133] Recently, Barroso-Luque et al.[26] adapted the Perzyna formulation for plastic von-Mises flow[131] assuming Li had minimal elasticity and no hardening and found the pseudo-viscosity follows

$$\eta = \frac{\sigma_{\text{flow}}}{\sqrt{3}\dot{\epsilon}} \quad (Equation\ 1)$$

Where η (Pa·s) is the pseudo-viscosity, $\dot{\epsilon}$ (s^{-1}) is the local strain rate, σ_{flow} (Pa) is the applied stress that results in plastic flow, and the $1/\sqrt{3}$ factor is due to the von-Mises flow assumption. At the temperatures of interest for solid Li, creep deformation should be the primary deformation mechanism[116] where σ_{creep} comes from power law creep and is represented as

$$\sigma_{\text{creep}} = \left(\frac{\dot{\varepsilon}}{A_c}\right)^{\frac{1}{m}} \exp\left(\frac{Q_c}{mRT}\right) \quad (Equation\ 2)$$

Where A_c is a material-specific creep parameter, Q_c is the activation energy for dislocation climb, m is the power law creep exponent, T is the temperature in Kelvin, and R is the Universal Gas Constant.[116,118] Assuming plastic deformation/flow occurs when $\sigma_{\text{flow}} = \sigma_{\text{creep}}$, substituting Eq. 2 into Eq. 1 results in

$$\eta = \frac{1}{\sqrt{3}\dot{\varepsilon}}\left(\frac{\dot{\varepsilon}}{A_c}\right)^{1/m} \exp\left(\frac{Q_c}{mRT}\right) \quad (Equation\ 3)$$

The alternative to Eq. 3 is to set $\sigma_{\text{flow}} = \sigma_{\text{yield}}$ where σ_{yield} is the yield stress. Interestingly, whether $\sigma_{\text{flow}} = \sigma_{\text{yield}}$ or $\sigma_{\text{flow}} = \sigma_{\text{creep}}$, similar pseudo-viscosity values were found across a wide range of temperatures and strain rates.[26] This overlap might be partially explained by the observation that significant amounts of creep may occur for low stresses and

strains for alkali metals.[118,119] Since the yield model can only be used where there is existing data at a fixed temperature and strain rate, the creep model is more robust. Therefore, Eq. 3 was used to calculate the pseudo-viscosity of solid Li using the parameter values from LePage et al.[116]

To further quantify the role of mechanical properties of Li on the CCD, the viscosity and diffusivity were analyzed as a function of temperature and across the melting point of Li (Figure 5.8). The liquid Li diffusivity reference data is extrapolated using nuclear magnetic resonance[134] and the Cohen-Turnbull theory for liquid metal diffusion.[134,135] The solid Li diffusivity data comes from published sources that used a tracer diffusion method.[113,136] Molten Li viscosity comes from an average of published oscillating sphere/cylinder viscometer data,[137] and the strain-rate dependent pseudo-viscosity of solid Li is from Eq. 3. The strain rate range was calculated using data from LePage et al.[116] using a current density range of 1-1000 mA/cm^2 based off the CCD range shown in Figure 5.4 from 25-195 °C.[116]

Comparison of Viscosity and Diffusivity vs. Critical Current Density Across the Melting Point of Li

Two main properties drive Li transport within the electrode: viscosity and Li^0 diffusivity. Within the solid regime, from 25 °C to 180 °C, viscosity is only slightly affected by temperature, whereas the diffusivity changes by three orders of magnitude (Figure 5.8). Across the melting point both properties have dramatic step changes. The viscosity decreases by about ten orders of magnitude and the diffusivity increases by about three. These step changes likely drive the step change in CCD across the melting point (Figure 5.4). This is in good agreement with previous literature,[138,139] which discuss how these changes in mechanical properties across the melting point of Li influence the mechanisms behind filament formation and CCD. The quantification of step changes in viscosity, Li^0 diffusivity, and CCD across the melting point of Li shown here can

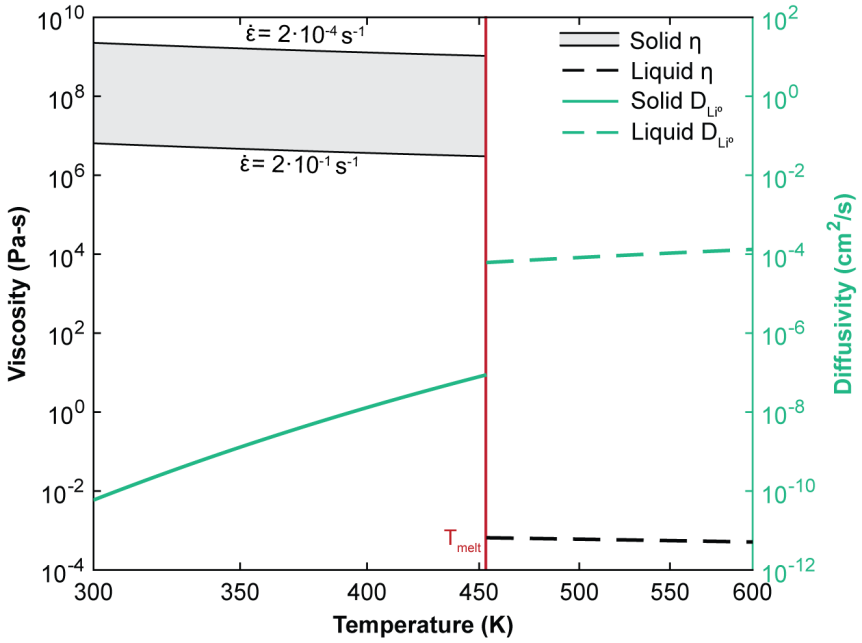

Figure 5.6. Viscosity vs. Strain Rate and Li^0 Diffusivity of both Solid and Molten Li. Viscosity versus diffusivity of Li as a function of temperature across the melting point of Li. Since the exact strain rate is unknown it is presented as a range.

inform future efforts to develop more comprehensive, quantitative models of Li filament nucleation and growth both above and below the melting point of Li.

Conclusions

In this study, we demonstrate that solid-state batteries using molten Li anodes are compatible with high-rate charging. Current sweep experiments reveal the CCD of molten Li|LLZO at 195 °C to be (530 ± 140) mA/cm^2. This CCD is an order of magnitude higher than expected if solid Li CCD trends are followed and is due to a step increase in CCD across the melting point of Li. This step increase is attributed to step changes in the mechanical properties of Li, which allow for pressure relaxation within the Li electrode that prevents LLZO fracture and Li filament formation. *Operando* optical videos reveal that molten Li propagation is marked by cycles of internal pressure build-up followed by pressure release due to surface eruptions. For solid Li, surface eruptions are limited due to a higher resistance to flow. These results shine new light on mechanisms of Li filament propagation, show the promise of a molten Li cell for high-rate applications, and inform future efforts in developing quantitative models of the mechanisms behind filament formation. In addition, the findings highlight similar trends with solid-state batteries using a Na anode, indicating that similar mechanisms may be at play in other alkali-metal anode systems.

Experimental Procedures

LLZO Synthesis and Pre-Conditioning

LLZO powders of composition $Li_{6.5}La_3Ta_{0.5}Zr_{1.5}O_{12}$ were prepared through solid-state reaction synthesis using the following precursor powders: Li Carbonate (99%, Alfa Aesar, Ward Hill, MA), Lanthanum (III) Oxide (99.99%, Pacific Industrial Development Corporation, Ann Arbor, MI), Nano Zirconium Oxide (99.9%, Inframat Advanced Materials LLC, Manchester, CT), and Tantalum (V) Oxide (99.9%, Inframat Advanced Materials LLC). The combined powders were milled and subsequently calcined at 1000 °C for 4 h under flowing dry air on a MgO boat. The calcined powders were then hot-pressed at 1225 °C under flowing argon at constant 47 MPa pressure for 40 minutes using rapid induction hot-pressing as previously described in our prior work.[140] The hot-pressed disks were of high relative density (> 96% relative density) and were ≥ 98% phase pure according to XRD analysis. After hot-pressing, the LLZO was cut into disks 1.3 ± 0.3 mm thick with a 12.7 mm diameter. Each disk was then wet polished down to a 0.1 μm finish using diamond paste and then heat treated in argon at 400 °C for 4 h to remove surface contaminants, such as Li_2CO_3 and LiOH, according to the method described by Sharafi et al.[114] in order to have low interfacial resistance.

O*perando* Optical Li Cycling Cell

The molten Li optical cell experiments were conducted in an argon glovebox with 0.1 ppm or less of O_2 and 0.2 ppm or less of H_2O. A schematic of the cell design is shown in Figure 5.1a. Cells were heated by placing on a hot plate covered with Ni foil and kapton tape to form a thermally conductive but electrically insulating surface. A thermocouple was used to measure the temperature of the base of the LLZO and the hot plate was adjusted until the LLZO was at the

desired temperature. 195 °C was chosen for the molten cycling tests as it is above the melting point of Li, 180 °C, to assure the Li remains molten during testing. Solidification of the Li was not observed during the molten Li tests, indicating minimal (<15 °C) temperature gradients within the LLZO. Since Li penetration begins at the Li-LLZO interface the thermal gradient of the surface plane is likely to be much smaller than this value precluding significant temperature distribution effects on failure.

A reservoir of Li (99.9%, Sigma Aldrich, Inc) was placed in an open-top crucible and heated on the hot plate until the Li melted. The exposed molten Li tended to form a contamination skin, possibly Li_2O or LiOH from trace water and oxygen in the glovebox, so this was skimmed off the surface to purify the Li immediately before drawing up the molten Li into a heated stainless-steel syringe. Molten Li sessile droplets were then deposited on the surface of the heated LLZO from the syringe (Figure 5.1a). The contact angle of the molten Li droplet was used as a proxy of the amount of contamination present on the Li|LLZO interface,[114] so only tests that had low levels of contamination were used. W (tungsten) probes were inserted into the droplets and connected to a Potentiostat (Biologic SP-200). A camera (Canon EOS REBEL T2i/EOS 550D) with 18- 135 mm lens was used to take head-on photos of molten Li droplets to calculate the contact area with the average area being (0.09 ± 0.03) cm^2. The molten Li droplets sat on the heated LLZO for an average of 30 minutes before the start of the tests. Current was passed in one direction. To minimize the effect of Li depletion from stripping, the smaller electrode droplet (0-20% smaller) was used as the plating electrode. The current densities in this paper are set to and defined by this smaller plating area. Post-mortem imaging confirms the main droplet areas remained constant during the experiments.

Post-mortem analysis was also conducted. Two types of samples were analyzed by FIB-SEM. The first were cleaned with isopropyl alcohol to remove Li on the surface and then cross-sectional FIB-SEM images (Thermo Fisher Helios 650 Nanolab SEM/FIB) were taken to show subsurface cracking and voids. For the second type of sample, the surface was not cleaned, leaving the LLZO surface in its pristine post-cycling state. Cross-sectional FIB-SEM (Thermo Fisher Helios G4 PFIB UXe) was then used to show the interactions between the secondary droplets and the subsurface cracking. All FIB-SEM samples had brief air exposure during sample cleaning and/or transfer to FIB-SEM. Samples were also examined under an optical microscope (Opto Engineering RT-HR-6M-71 telecentric lens) with a backlight.

Chapter 6

Rate Limitations in Composite Solid-State Battery Electrodes

Adapted with permission from Davis, A. L.; Goel, V.; Liao, D. W.; Main, M. N.; Kazyak, E.; Lee, J.; Thornton, K.; Dasgupta, N. P. Rate Limitations in Composite Solid-State Battery Electrodes: Revealing Heterogeneity with Operando Microscopy. *ACS Energy Letters* **2021**, 2993–3003. The electrochemical dynamics modeling work included herein was performed by Vishwas Goel and Katsuyo Thornton.

Chapters 3-5 focused on the Li-metal anode. In addition to that work, other research efforts over the past decade have also largely focused on enabling Li metal anodes in SSBs as the holy grail of high energy density materials, with promising results.[15,16] However, while impressive progress has been made with metal anodes, less attention has been paid to composite electrodes, which consist of a blend of SE and active material and more closely resemble Li-ion electrodes. Enabling composite electrodes is an important challenge for the cathode side of SSBs and could also enable all-solid-state graphite anodes, which would eliminate the flammability concerns in current LIB chemistries.

Despite the analogous structure of composite solid-state electrodes to porous electrodes in liquid-based cells, there are several key differences that must be understood in order to explain the behavior of SSBs. In liquid electrolyte systems, the surface of the electrode particles can be easily wetted by the electrolyte because the liquid can flow into any open voids or pores. In contrast, SE

materials are more resistant to deformation. Therefore, any pores that form during electrode manufacturing or from cracking during charging/discharging can reduce the interfacial contact area between active material and the electrolyte.[35,36] Another difference arises from the fact that anions are mobile in liquid electrolytes, which leads to an ionic transference number of significantly less than unity for Li^+.[141] In contrast, most inorganic SEs are single-ion conductors, with Li^+ being the only species with significant mobility. As a consequence, bulk transport through the SE occurs solely through migration. Additionally, variations in Li^+ activity in the SE phase will not influence the equilibrium potential or interfacial kinetics, because no concentration gradients form.

In both LIBs and SSBs, simultaneously achieving high energy density and high power density is challenging. By increasing the electrode thickness (areal capacity) and/or active material volume fraction within the composite electrode, the theoretical cell energy density increases.[38,142] However, both of these factors decrease the electrode rate capability. In LIBs, the fundamental phenomena that govern performance in porous electrodes during fast-charging have been studied extensively.[143,144] While interface resistance and solid-state diffusivity within the active materials play a role, cycling high-energy-density LIBs with graphite anodes at high C-rates is primarily limited by mass-transport in the liquid phase, where large concentration gradients develop.[142,144] These ionic concentration gradients result in current focusing near the surface of the electrode and large cell polarization, which can lead to reduced accessible capacity and irreversible degradation modes including Li plating on graphite.[143]

Compared to liquid electrolytes, the fundamental differences in both mechanical and transport properties will change the behavior of solid-state composite electrodes at high charge/discharge rates. For instance, since the concentration of Li^+ does not vary significantly as

a function of position within single-ion conducting SEs, there is often a perception that current inhomogeneity through the depth of the composite electrode will be significantly suppressed. However, as we show in this study, significant current focusing still occurs, which is amplified at increasing C-rate and decreasing SE content within the composite. In general, the mechanisms that govern rate capability of composite electrodes in SSBs have not been fully elucidated. Furthermore, the role of microstructural features, such as particle-particle contact area, tortuosity, particle sizes, interphase formation, and inter/intra particle cracking, on rate performance of SE-based composite electrodes is not well understood.

Recent studies have begun to probe these phenomena in solid-state composite cathodes. Minnmann et al. and Park et al. examined the effects of electrode microstructure on power density by probing the impacts of the relative electronic and ionic conductivities of the electrode.[145] Shi et al. and Bielefeld et al. combined modeling with electrochemical measurements to examine the effect of particle size on percolation pathways and accessible capacities.[146,147] A variety of *ex situ, in situ* and *operando* techniques have also been used to visualize lithiation throughout the composite cathode including Raman imaging[148], electron energy loss spectroscopy (EELS)[149,150], X-ray absorption spectroscopy (XAS)[151], time-of-flight secondary ion mass spectrometry (ToF SIMS)[152], and Kelvin probe force microscopy (KPFM)[153].

Studies have also probed solid-state composite anode materials, particularly those based on graphite.[37,38] Höltschi et al. analyzed cycling voltage traces to show that rate performance improves with increased temperature but is diminished as electrode thickness increases.[154] Kato et al. used composite graphite electrodes with two different SEs to show that increased ionic conductivity leads to enhanced rate performance.[38] Additionally, Kim et al. demonstrated graphite

electrodes with increased energy density by replacing SE/graphite composite electrodes with slurry cast graphite electrodes without any SE. [155]

Graphite has proven to be a useful model system to study the spatial inhomogeneity in ionic transport and state-of-charge (SOC) in LIBs because of the visible color changes that occur within graphite throughout lithiation. Otoyama et al. recently used plan-view and cross-sectional microscopy to observe the evolution of gradients in local SOC within graphite composite electrodes throughout cycling.[156,157]oughout cycling.[156,157] Overall, while general trends have been increasingly reported in composite electrode processing and analysis, there remains a lack of fundamental mechanistic understanding of the role that microstructural inhomogeneity plays on current focusing in single-ion conducting electrolytes. In particular, there is a need to decouple the relative contributions of solid-state diffusion within the active material, interfacial kinetics, and electrostatic potential gradients in the SE to rate-performance limitations. Deepening our understanding of the role these mechanisms play can improve our ability to rationally design microstructures that enhance cell power densities while maintaining high energy densities.

In this study, we use graphite/Li_6PS_5Cl composite electrodes as a model system to study Li transport within solid-state composite electrodes. By cycling these electrodes at varying C-rates, we show rate performance limitations where the accessible capacity decreases as C-rate is increased. These tradeoffs are amplified as the mass percentage of active material in the composite electrode is increased from 40% to 100%. We further probe the spatial inhomogeneity in local SOC as a function of C-rate and areal capacity using *operando* video microscopy, which allows us to visualize of the influence of electrode microstructure on rate capability with high spatial and temporal resolution.[13,22,39] We observe that similar to liquid electrolytes, current focusing within the composite electrode occurs near the interface with the bulk SE (separator), which is intensified

at high rates. Using electrochemical dynamics simulations, we further investigate the underlying mechanisms that lead to the observed gradients in local SOC. The results of this study point to the important role of electrostatic potential gradients in the SE phase of the composite electrode, solid-state diffusion in the active material, and localized variations in electrode microstructure on the rate capability of composite SSB electrodes. We note that while in this study we use graphite as a model system, the conclusions are relevant to a range of composite electrodes in SSBs, including cathode materials.

Sample Characterization. Experiments were performed in cells with graphite working electrodes and Li metal counter electrodes. To fabricate the composite electrodes, graphite and Li_6PS_5Cl (LPSCl) powders were mixed using roll milling with various weight ratios from 40% graphite/60% LPSCl (40% Gr) to 100% graphite/0% LPSCl (100% Gr). All experiments were performed at 60° C with an applied stack pressure of 7 MPa.

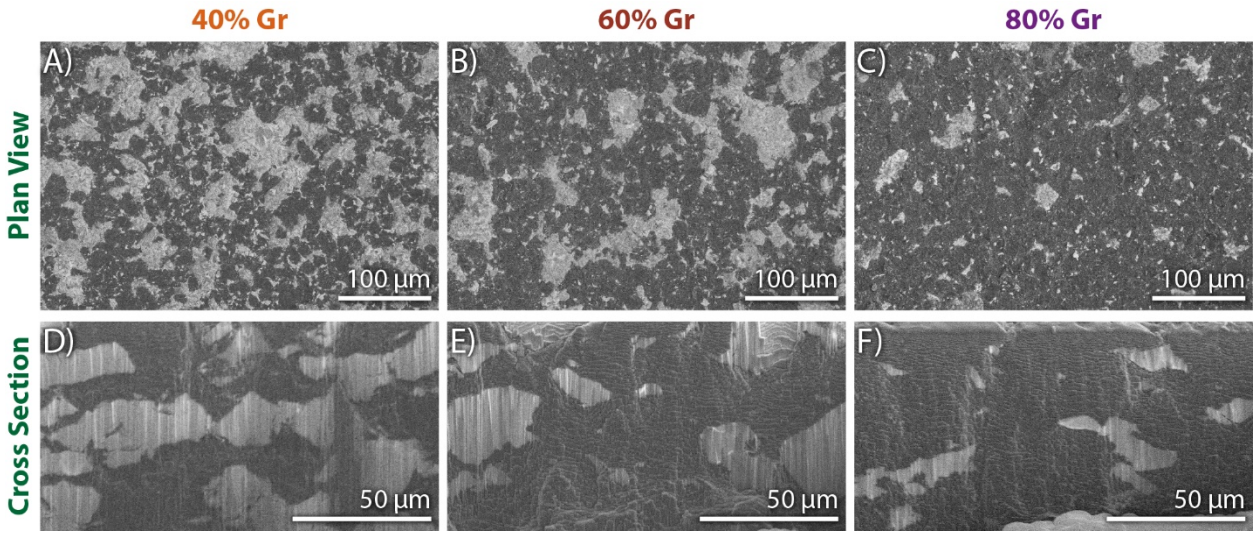

Figure 6.1. (A-C) Plan-view (top-down) and (D-F) FIB cross-sectional SEM images of graphite/LPSCl composite electrodes with varying graphite/SE ratios. The dark regions are graphite, and the bright regions are LPSCl.

Composite electrodes are composed of two interconnected pathways: 1) the electronic pathway through the active material, and 2) the ionic pathway through the SE. To visualize these pathways, scanning electron microscopy (SEM) images were captured from both a plan-view (top-down) perspective and using a focused ion beam (FIB) milling to prepare cross sections (Figure 6.1). In the low-graphite-content sample (40% Gr), clear percolation pathways are visible for both the SE and the graphite. However, as the graphite content increases, the interconnectivity of the SE decreases. We note that additional 3-D pathways will be present that are out of view in each of the 2-D sections.

To further probe these two interconnected pathways, the relative electronic and ionic conductivities of each electrode were measured using electrochemical impedance spectroscopy (EIS) and DC conductivity measurements respectively (Figure 6.2). In all of the samples, the

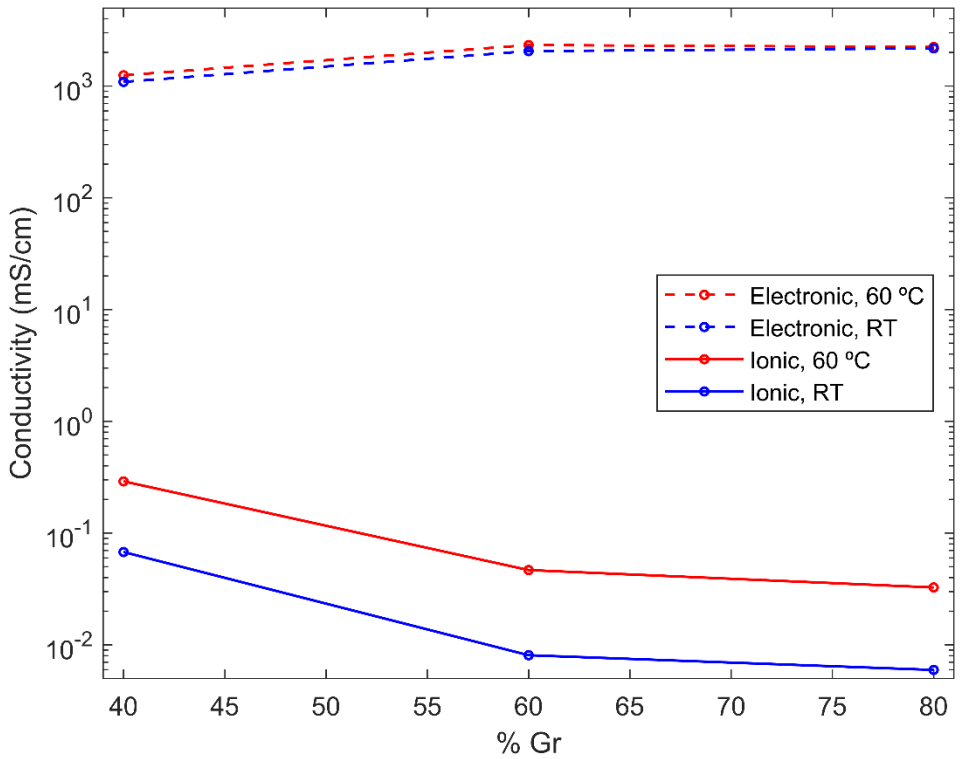

Figure 6.2. Electronic and ionic conductivity measurements of graphite composite electrodes with different graphite ratios and temperatures.

electronic conductivity of the electrode (~10^3 mS/cm) was orders-of-magnitude higher than the ionic conductivity (~0.1 mS/cm), and this difference is further amplified as the graphite fraction is increased. As a result, the transport properties of the composite electrodes are limited by ionic transport.

Electrochemical Rate Performance. To quantify the rate capability of the composite electrodes, cells with varying graphite/SE ratios were assembled and cycled. As the fraction of graphite is increased, the theoretical specific capacity of the composite electrode (including the mass of the SE) increases from 149 mAh/g for 40% Gr to 372 mAh/g for 100% Gr. Each sample was cycled over a range of C-rates from C/16 to 1C using a CC-CV cycling protocol. The constant current (CC) portion of the graphite lithiation was performed at the proscribed C-rate until a cell voltage of 0.02 V vs. Li/Li^+ was reached. This was followed by a constant voltage (CV) hold until the total CC-CV time was reached for a given C-rate value (for example, for a C/16 cycle, the total time of lithiation was 16 hrs).

The accessible capacities during the CC-CV lithiation at each rate are shown in Figure 6.3A. Additional figures summarizing the fraction of this capacity that was accessed during the CC step, as well as the specific capacities are included in the Figure 6.4. Within each sample, as the C-rate is increased, the accessible capacity decreases. Additionally, as the fraction of graphite in the composite electrode is increased, the accessible capacity at each C-rate decreases.

At the end of the rate tests, a final cycle was run at C/16. By comparing the first and last cycles, it is apparent that permanent capacity loss does not occur during cycling, and therefore the trends shown in Figure 6.3A are limited by the electrode rate capability. Throughout cycling, a

constant C/8 delithiation process was used, which allowed for full delithiation of the electrode. (Figure 6.5).

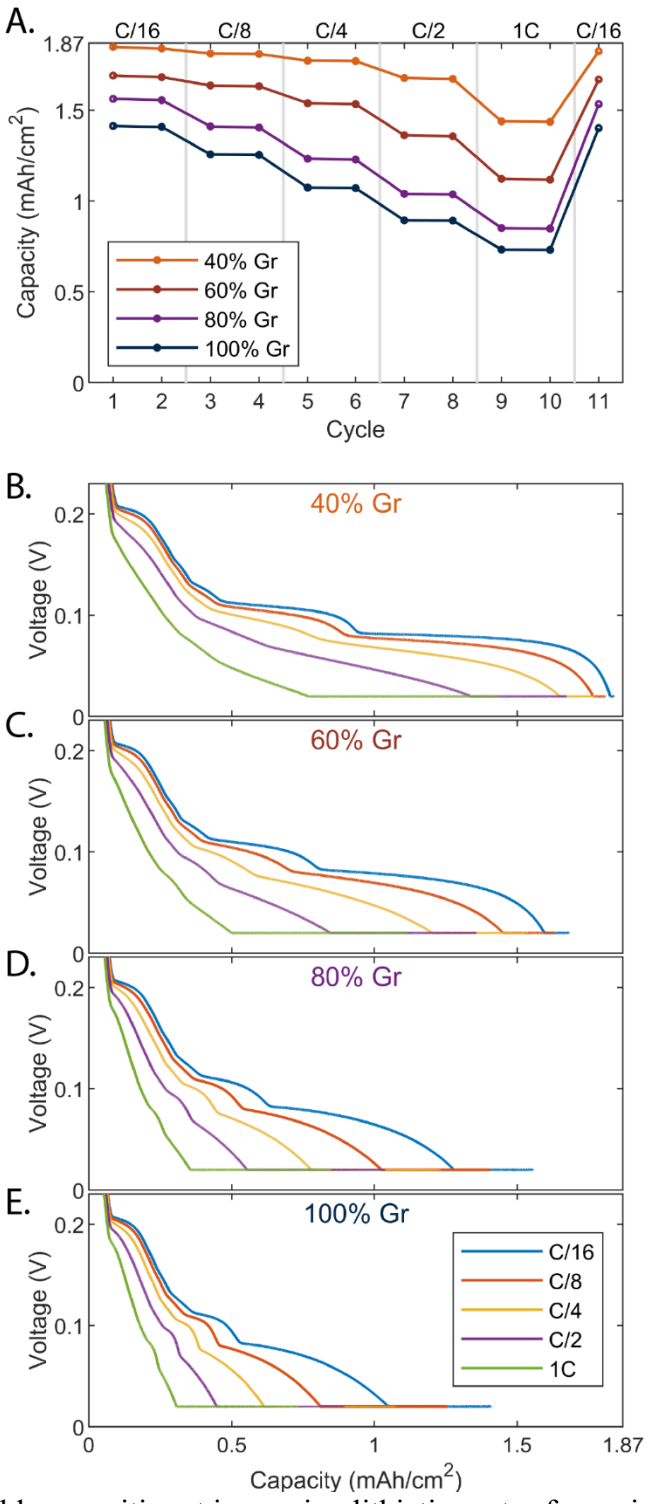

Figure 6.3. (A) Accessible capacities at increasing lithiation rates for various graphite/SE ratios. Sample loadings are 1.87 mAh/cm^2. (B-E) Corresponding lithiation voltage traces for each graphite ratio.

For each sample, the lithiation voltage traces are shown in Figure 6.3B-E. Consistent with liquid electrolytes, the voltage plateaus observed correspond to the stages of graphite lithiation.[158] At low C-rates in the 40% Gr sample (Figure 6.3B), the plateaus are relatively flat, and 99% of the theoretical capacity is accessible. However, as the C-rate increases, the plateaus become more sloped, and the voltage cutoff is reached at successively earlier stages of cycling. As the graphite fraction is increased (Figure 6.3C-E), this sloping of the plateaus is successively amplified.

This sloping of the voltage profile within the plateau region has been shown in liquid LIBs to indicate spatial heterogeneity in local SOC throughout the depth of the electrode.[159,160] The

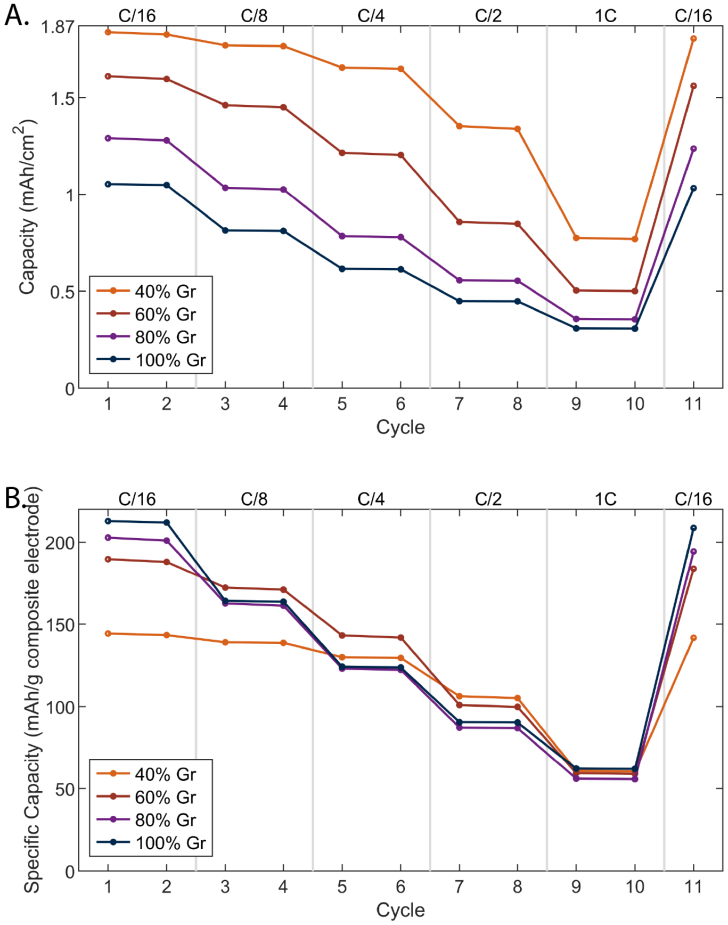

Figure 6.4. (A) Accessible capacity during the CC portion of the lithiation of the 1.87 mAh/cm^2 cells from figure 2 in the main text. (B) CCCV lithiation capacities normalized by the mass of the composite electrode.

observation of these same trends in composite electrodes with a single-ion conducting SE suggest that current focusing still occurs, despite the lack of a concentration gradient in the SE. This effect

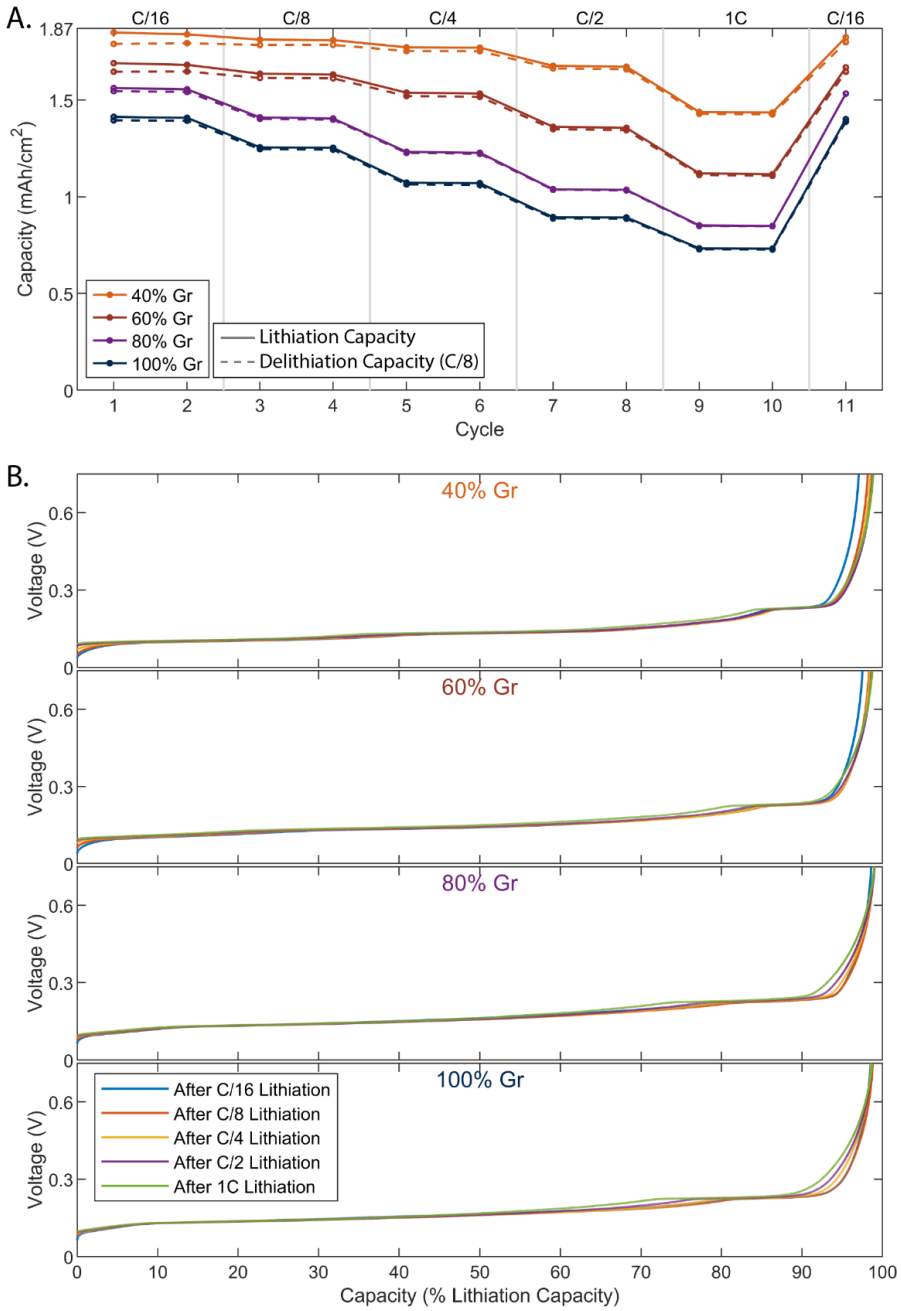

Figure 6.5. (A) Delithiation capacities for 1.87 mAh/cm^2 cells from Figure 2 in the main text. All delithiation cycles were performed at C/8 but are plotted under the C-rate of their corresponding lithiation step. Some coulombic inefficiency is apparent in the early cycles of the 40% and 60% Gr samples due to continued SEI formation. (B) Corresponding voltage traces for each graphite ratio and C-rate. Again, voltage traces are labeled with the c-rate of their corresponding lithiation step. Delithiation voltage traces have also been normalized to lithiation capacity achieved in the lithiation step to allow for a more direct comparison.

will be explored in detail in the *operando* microscopy and modeling results below.

As the fraction of graphite increases to 100%, even at a C/16 rate, most of the plateaus are sloped and the voltage cutoff is reached early in cycling (~1/6 the theoretical capacity). As a result of this increased cell polarization, the charge passed during the CC portion of the lithiation process continually decreases (Figure 6.4). In addition to reducing accessible capacity, the increase in cell polarization also decreases the energy efficiency of the cell.

The rate capability data as a function of graphite ratio shown in Figure 6.3 indicate the presence of clear rate limitations within solid-state composite electrodes. In liquid LIBs, power/energy density tradeoffs are strongly influenced by transport limitations in the electrolyte, which are affected by the electrode porosity and tortuosity in addition to the electrolyte conductivity.[143] However, in SSBs, the single-ion-conducting electrolyte phase does not allow Li^+ concentration gradients to form. Therefore, to study the relationships between electrode microstructure and heterogeneity in local SOC, we applied a combination of *operando* microscopy and electrochemical modeling to develop an improved understanding of the mechanisms of Li transport within composite SSB electrodes.

***Operando* Video Microscopy.** To probe the relationships between rate capability and microstructure within the solid-state composite electrodes, a custom visualization platform was implemented. As graphite lithiates, it changes color, which is caused by shifts in the plasma frequency as a function of SOC.[161,162] This allows for direct observation and analysis of gradients in local SOC throughout the electrode. To directly observe these color changes, *ex situ* experiments were first performed, where the top surface of the graphite electrode was imaged at different stages of lithiation using optical microscopy (Figure 6.6A). Samples were lithiated at a slow C-rate (C/32)

to allow for a relatively uniform lithiation throughout the electrode. The colors observed match those reported for liquid electrolyte systems, where the color of graphite evolves from gray (unlithiated graphite) to blue (LiC_{18}), red (LiC_{12}), and gold (LiC_6).[163–166]

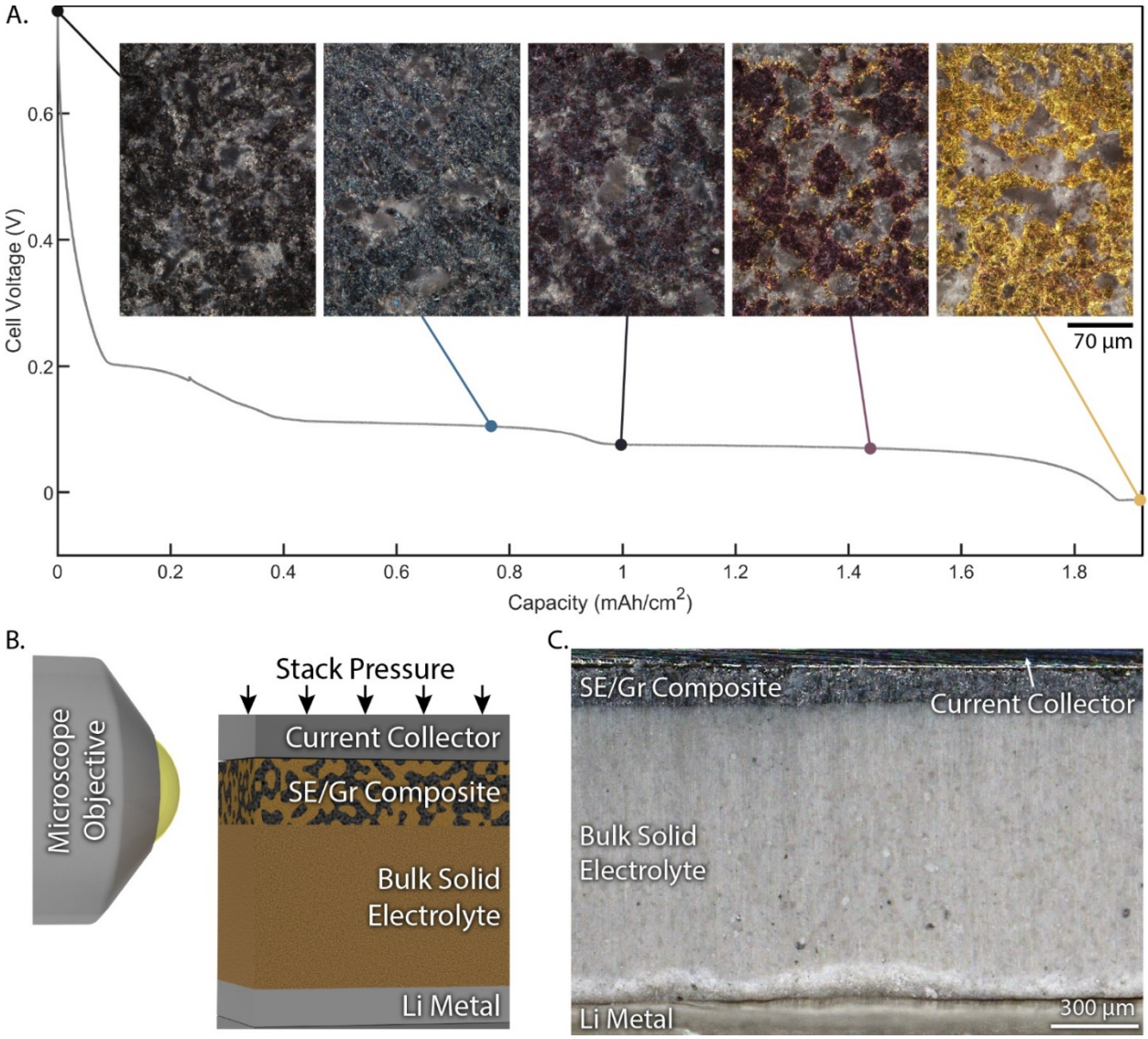

Figure 6.6. (A) Top town ex-situ images of graphite composite electrodes showing color changes in the graphite phase throughout lithiation. Electrodes were lithiated at C/32 to various SOC. Electrode areal capacities are 1.87 mAh/cm^2 with a graphite fraction of 46%. (B) Schematic showing custom cell for *operando* visualization of composite electrode cross. (C) Zoomed out view showing Li/graphite half cell assembled in the visualization platform.

For the *operando* experiments, Li/Gr half cells were assembled in the visualization platform (Figure 6.6B-C). For each cell, a cross-sectional view of the composite electrode was imaged during lithiation. The full videos for 40-100% Gr cells are provided as supplementary videos. Cycling was performed using a similar CC-CV protocol to the *ex situ* cells, with a longer CV duration to allow for an extended visualization of the lithiation process (further details on the cycling protocols are provided in the Supporting Information).

As a representative sample, Figure 6.7 shows the evolution of a 4 mAh/cm^2, 40% Gr cell charged at a C/4 rate. During the early stages of lithiation (Figure 6.7A-B), the graphite turns from dark grey to dark blue. As the electrode reaches >50% global SOC, a gradient in color develops. The graphite close to the interface with the bulk SE turns red and then gold, while the particles deeper within the electrode (closer to the current collector) experience a more delayed color change. This indicates that the local current density is greatest near the bulk SE interface, and reduces with depth. Each color then slowly propagates through the electrode until it reaches the current collector. At the end of charging, a uniform gold color is observed in the graphite throughout the electrode. Figure 6.8 shows the evolution of the electrode throughout delithiation.

Within the composite electrodes, there are two main Li transport paths: 1. Li^+ conduction through the SE (Figure 6.7G) and 2. Li diffusion within the graphite (Figure 6.7H). Limitations in both paths lead to visible gradients in local SOC within the electrode. Corresponding to the first path (Figure 6.7G, ionic transport in the SE), the regions near the bulk SE lithiate faster, which results in a local SOC gradient through the depth of the electrode (Figure 6.7C-E). Corresponding to the second path (Figure 6.7H, Li diffusion in graphite), graphite regions within the composite electrode lithiate inwards from the nearest SE/graphite interface, which generates a gradient in local SOC from the interface into the center of the graphite region. This two-dimensional diffusion

pathway is most visible in the larger graphite regions in Figure 6.7D-E where the edges are gold, but the centers are still blue and red.

To probe the origins of these spatial inhomogeneities in local SOC, we examine the effect of three distinct parameters on the electrode rate capability: (1) graphite/SE ratio, (2) C-rate of lithiation, and (3) total electrode capacity (thickness). Still frames for various graphite/SE ratios

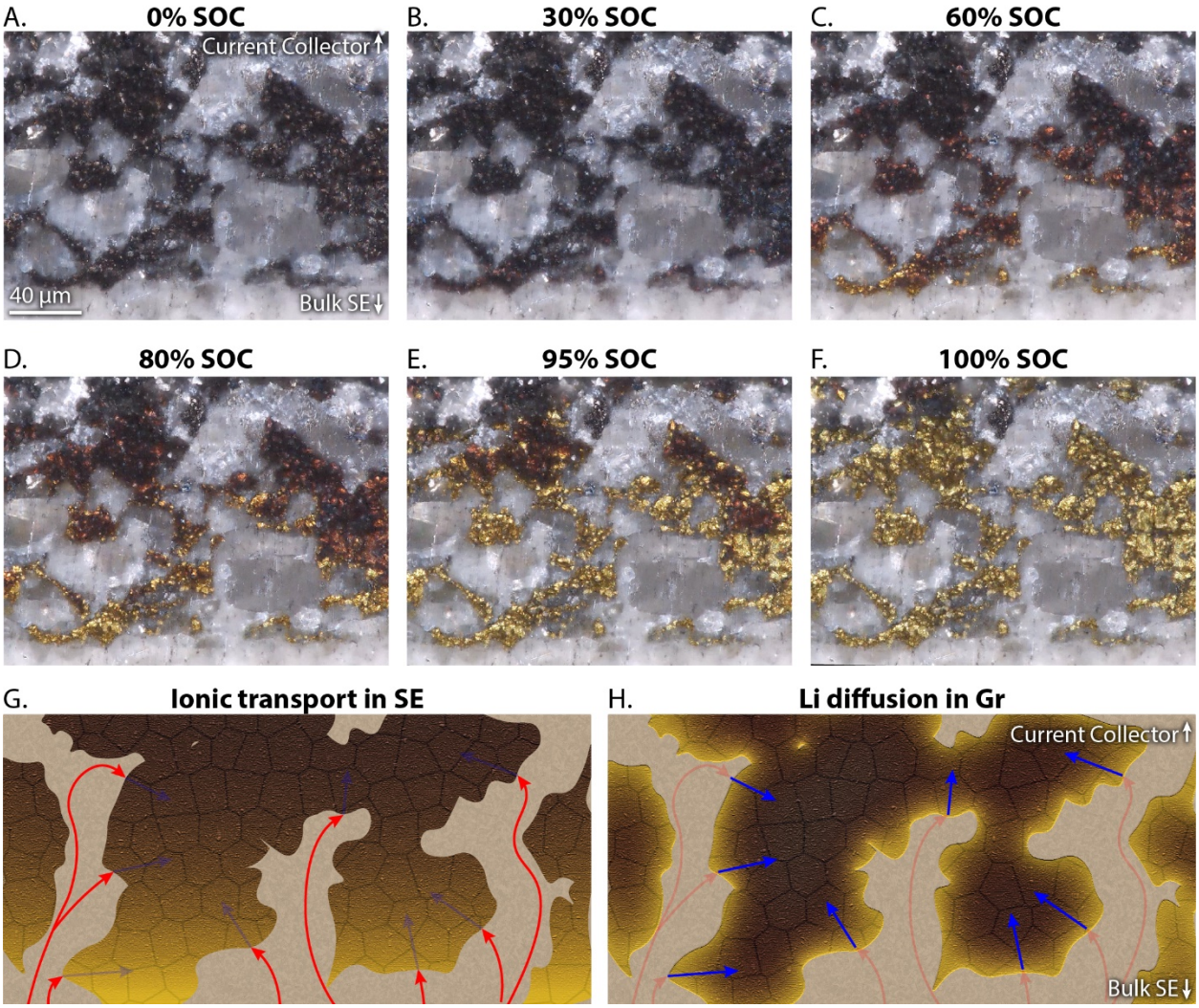

Figure 6.7. (A-F) Time series showing zoomed in microscope images of 40% Gr composite electrode at different states of charge during C/4 lithiation. Full videos for 40-80% Gr are included in the Supporting Information. (G-H) Schematics showing transport limitations due to ion conduction within the SE (G) and Li diffusion within the graphite (H).

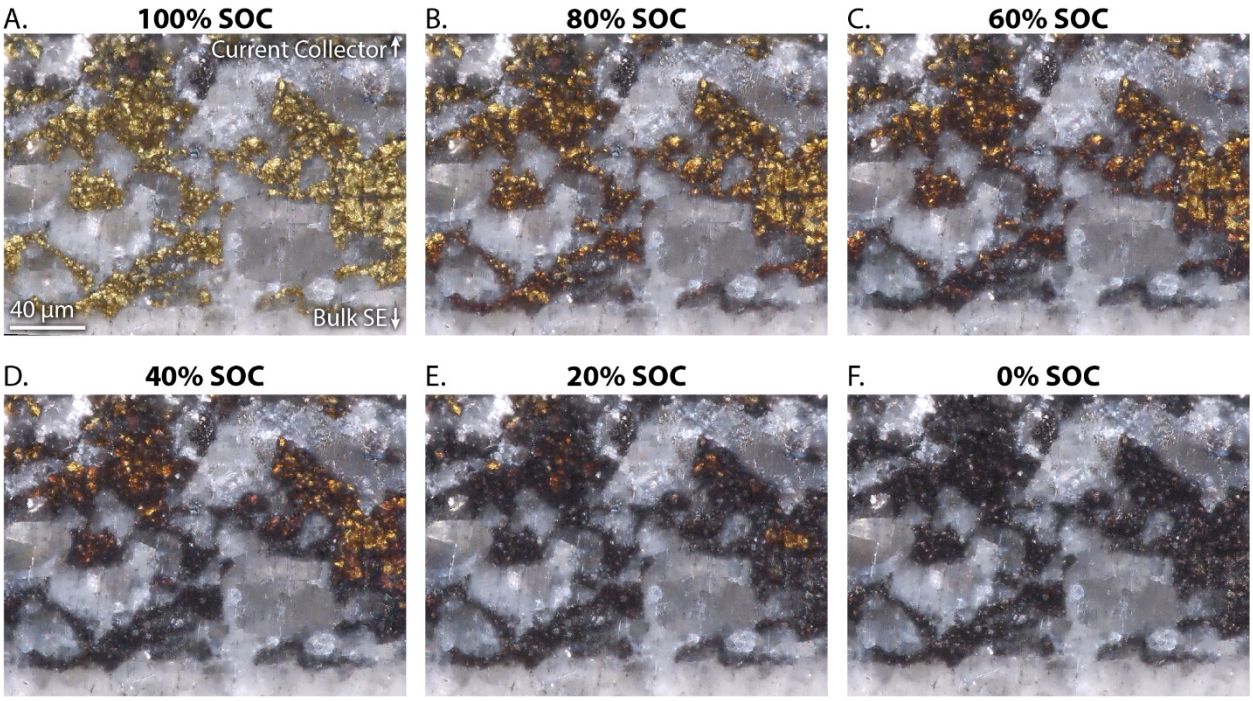

Figure 6.8. Time series showing zoomed in microscope images of 40% Gr composite electrode at different states of charge during C/4 delithiation.

are shown at rates of C/16 (after 16 hr) and C/4 (after 4 hr) in Figure 6.9, and the full videos are provided in Videos S1-S3.

For low graphite fractions (40% Gr) at a slow C-rate (C/16), only slight gradients in local SOC are visible throughout lithiation (Figure 6.9A). At low graphite fractions, the interconnected SE domains in the composite electrode act as low-resistance ionic transport channels, which allow for lithiation deep within the electrode. As the rate is increased to C/4 (Figure 6.9D), a stronger gradient in local SOC develops through the depth of the electrode, with higher concentrations of gold particles near the electrode interface with the bulk SE.

In the 60% Gr electrode (Figure 6.9B), SE channels still assist with ionic transport through the electrode, however the limited SE volume fraction and particle interconnectivity leads to stronger gradients in local SOC through the depth. As the C-rate is increased, these gradients become exaggerated (Figure 6.9E).

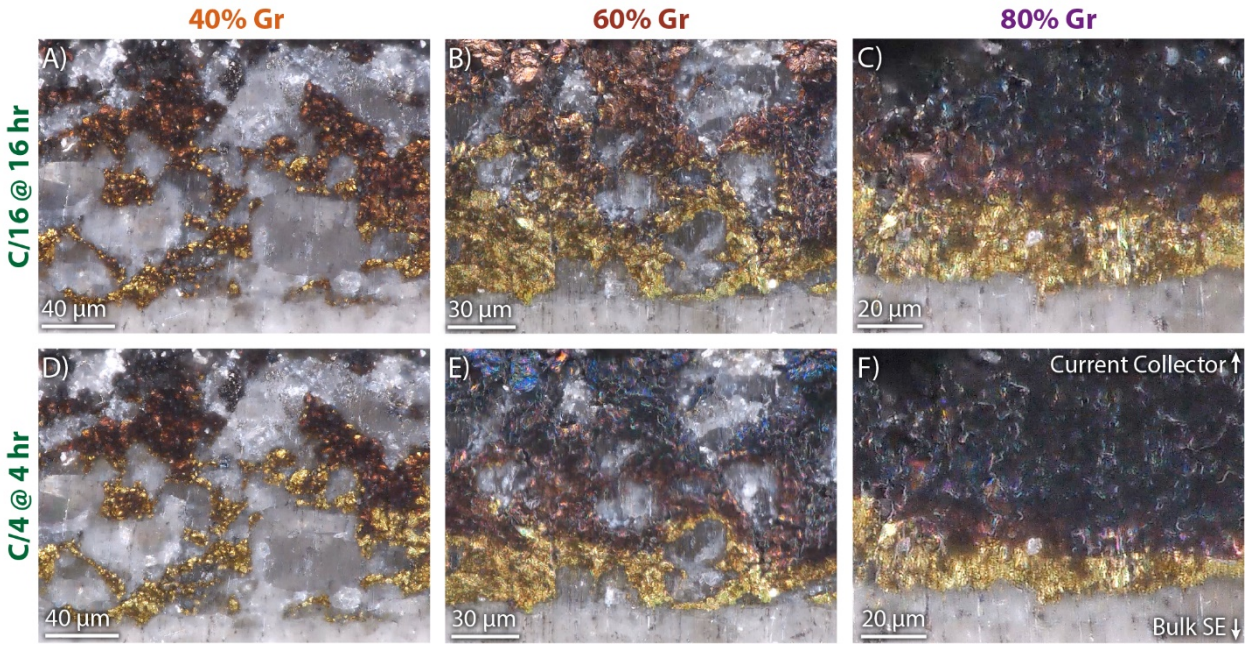

Figure 6.9. (A-F) Cross section snapshots at C/16 (top row) and C/4 (bottom row) rates, taken after 16 hr and 4 hr of lithiation respectively. Composite electrodes are shown with various graphite ratios (40%-80% Gr) and an areal capacity of 4 mAh/cm^2. To better observe the gradients in each sample, the field of view was normalized to the thickness the electrode.

In the 80% Gr electrode (Figure 6.9C), the low SE volume fraction leads to minimal SE interconnectivity and correspondingly sparse SE channels through the electrode. Therefore, Li transport limitations are dominated by solid-state diffusion within the graphite and nearly the entire electrode acts as one large graphite region. As a result of this limitation, the region near the bulk SE fully lithiates during the initial stages of the half-cycle, while the regions near the current collector remain at a low local SOC, creating a strong color gradient (Figure 6.9C). This through-plane gradient is further exacerbated as the C-rate is increased (Figure 6.9F). These same trends are also evident in the 100% Gr sample (Video S4), providing further evidence that solid-state diffusion within the graphite active material is responsible for the observed gradients in local SOC/

To confirm that the trends observed at the cross-sectional surface in the operando experiments are representative of the behavior deeper within the bulk, a 60% Gr sample was

lithiated using a similar CCCV protocol. At the 4 hr cutoff, the sample was quickly disassembled and polished to observe the interior cross-sectional profile at a similar depth as was used in the operando cell. Similar gradients to those observed in the operando video were observed in the ex-situ cross section (See Figure S9 in the supporting information).

In addition to the 4 mAh/cm^2 cells shown here, identical visualization experiments were performed on thinner cells with 1.87 mAh/cm^2 loadings (Figure 6.10). As the electrode loading (and therefore thickness) decreases, the same trends are visible, but the through-plane gradients in local SOC are attenuated because of the shorter transport distances through the electrode. This illustrates another energy/power density tradeoff in solid-state composite electrodes because as areal capacity increases the stack specific energy density will increase, owing to a reduction in the mass of the electrolyte and inactive components of the battery. For this reason, the current trend

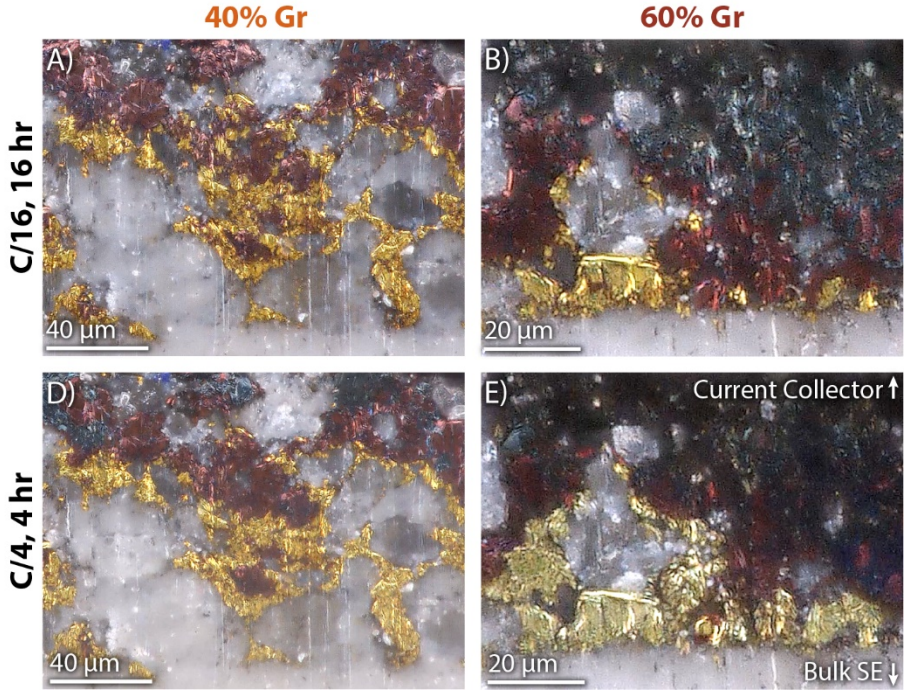

Figure 6.10. Cross section snapshots at 16 hr (C/16 lithiation) and 4 hr (C/4 lithiation) for composite electrodes with various graphite ratios (40%-60% Gr) and an areal capacity of 1.87 mAh/cm^2. To normalize the field of view for the different graphite ratios, the magnification is increased as graphite loading increases.

in commercial production of high-energy-density LIBs for EVs has been to move to increasingly thick electrodes, which will exacerbate rate limitations in composite SSB electrodes.

Overall, the *operando* analysis is consistent with the trends observed in the *ex situ* data shown in Figure 6.3, where higher graphite fractions and higher charge rates lead to reduced accessible capacity. As the graphite/SE ratio is increased, the ionic transport pathways through the SE channels are constricted, and eventually the percolation threshold is reached. The *operando* video results indicate that this transition occurs between the 60% and 80% Gr samples, which is generally consistent with models of spherical particles that suggest that the percolation threshold should be around 25-30%.[167] The breakdown of connected transport paths prevents the relatively facile ionic transport through the SE phase, and therefore Li transport becomes dominated by Li diffusion within the graphite, which is significantly slower. This trend is further corroborated with the ionic conductivity measurements (Figure 6.2), where the effective ionic conductivity within the electrode decreases significantly as the graphite fraction is increased.

Electrochemical Dynamics Simulations. To provide mechanistic insights into the observed behavior of gradients in local SOC within composite electrodes, two-dimensional electrochemical dynamics simulations were performed. We considered ion migration within the SE, Li diffusion in graphite, electronic conduction in the graphite and Li electrodes, and electrochemical reaction rate at the interfaces between the SE and electrodes (graphite and Li). The CC-CV charging protocol in the simulations were the same as in the *operando* microscopy experiments. The details on model equations, associated boundary conditions, model parameters, and the cell geometry used in the model are provided in the paper.[8] The simulated microstructure was generated based on the images captured from the *operando* visualization cell for the 40% Gr electrode with a loading of 4 mAh/cm^2 (shown in Figure 6.7). We note that the two-dimensional

microstructure used in our simulations does not fully capture the transport within the three-dimensional electrode and that the constrictions within the two-dimensional electrode can exacerbate the transport limitations. To test the effect of constriction zones in the microstructure on the electrochemical behavior of the electrode, we broadened the width of all such zones while maintaining the volume fraction of the electrolyte. The corresponding results are described in the Supporting Information (Figure S14), which show that even in the modified microstructure, both types of transport limitations (ionic conduction in SE and Li diffusion in graphite) are present, albeit in a lower magnitude. Thus, we conclude that despite the two-dimensional approximation, the model can still be used to elucidate the rate-limiting mechanisms and qualitative trends observed in the optical visualization experiments.

The results for the simulated voltage and current are provided in the Supporting Information (Figure S12). Consistent with the trends observed in the experimental results, the simulated plateaus in the electrode voltage become more sloped as the C-rate is increased. This corresponds with a larger heterogeneity in local SOC throughout the electrode thickness at a higher C-rate. Furthermore, the electrode reaches the CV cutoff voltage sooner as the C-rate is increased.

Figure 6.11A-E show the simulated distribution of local Li site fraction in graphite, which is directly related to local SOC, during C/4 charging. We note that Li concentration in the active material gets fully homogenized at 100% SOC due to the extended CV hold during charging (as shown in Figure S12, Supporting Information). The simulated results illustrate the two types of gradients in local SOC that were observed experimentally. The first gradient type is the variation through the depth of the electrode (Figure 6.7G), wherein the region near the electrode/bulk SE interface (the bottom edge in Figure 6.11A) is lithiated faster. The second type is the variation

within graphite domains (Figure 6.7H), where a Li concentration gradient develops in the direction from the graphite/SE interface into the interior of the domains.

The variation in local SOC as a function of depth within the electrode (Figure 6.7G) is caused by ionic conduction within the SE phase, which results in a gradient in the electrostatic potential (Ohmic drop) of the SE (Figure 6.11F). The relationship can be understood in terms of the variation in local overpotential at the SE/graphite interface, η_{Gr}, which is defined as

$$\eta_{Gr} = \phi_{s,Gr} - \phi_e - U_{Gr}, \quad (1)$$

where $\phi_{s,Gr}$ and ϕ_e represent the electrostatic potential of graphite and SE within the composite electrode, respectively, and U_{Gr} represents the equilibrium electrochemical potential (OCV) of graphite vs. Li/Li$^+$. The electronic conductivity of graphite is high enough to sustain the applied current without resulting in a large gradient in $\phi_{s,Gr}$. Thus, in the absence of any significant

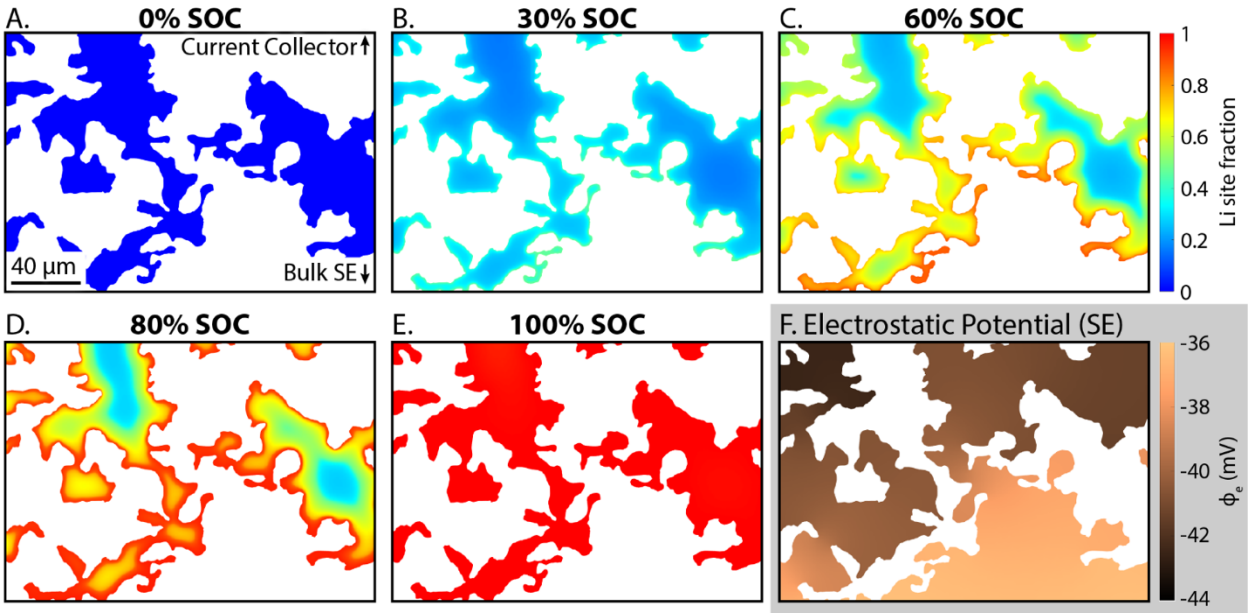

Figure 6.11. (A-E) Evolution of local Li site fraction in the 40% Gr electrode during C/4 charging at different SOCs. (F) Local SE potential in the electrode.

gradient in $\phi_{s,Gr}$, the variation in the overpotential is primarily driven by spatial heterogeneities in ϕ_e, and U_{Gr}.

At the beginning of lithiation, the Li site fraction in graphite (and thus U_{Gr}) is uniform throughout the electrode. Therefore, the spatial variation in η_{Gr} is primarily driven by the gradient in ϕ_e. This gradient results in a larger magnitude of η_{Gr} in the electrode regions near the interface with the bulk SE than regions near the current collector. Consequently, owing to the gradient in ϕ_e, we observe current focusing near the interface with the bulk SE, which results in the local SOC variation of the first type (Figure 6.7G). Furthermore, the results show that current focusing is present throughout charging. Therefore, despite the lack of Li^+ concentration gradients in the single-ion-conducting SE, current focusing occurs in the composite electrode regions near the interface with the bulk SE. Similarly, the current focusing would be observed near the

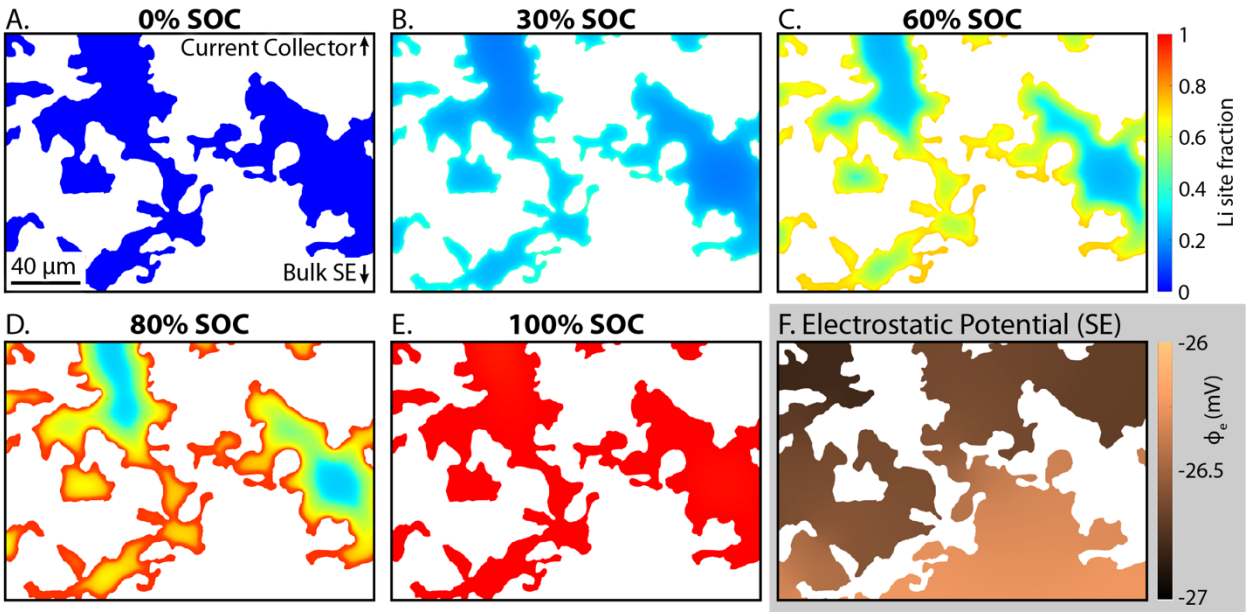

Figure 6.12. Simulation results for a κ value ~11 times higher than the nominal value, conducted to examine the effect of ionic conductivity in SE. (A-E) Evolution of local Li site fraction in the 40% Gr electrode during C/4 charging at different SOCs. (F) Local SE potential in the electrode.

electrode/current collector interface if the electronic conductivity of the active material is the limiting factor as the spatial variation in η_{Gr} would be driven by the gradient in $\phi_{s,Gr}$.[168,169]

To further demonstrate the role of Ohmic transport on the local inhomogeneity in local SOC, we simulated the same electrode geometry using a theoretical SE with ~11 times higher ionic conductivity than LPSCl. The results are summarized in Figure 6.12, which show that when the ionic conductivity of the SE is sufficiently high, negligible variations in the local SOC through the depth of the electrode are observed due to a smaller gradient in the electrostatic potential of the SE. This illustrates the importance of selecting a SE with high ionic conductivity when designing composite electrodes for SSBs, especially as the active material fraction and electrode thickness increase.

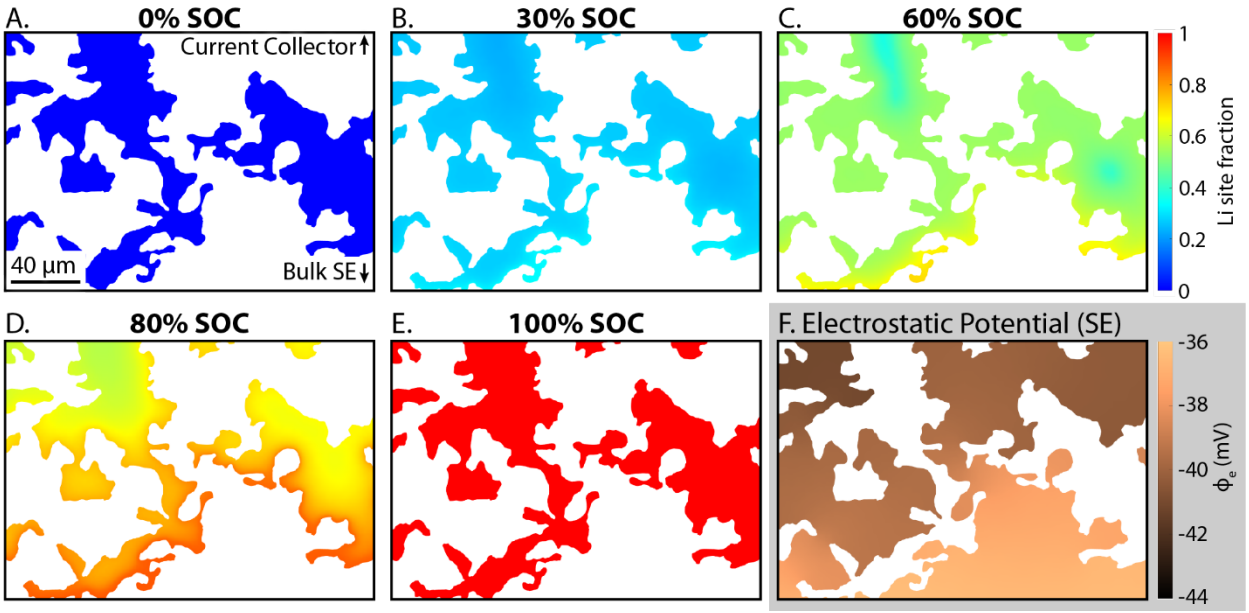

Figure 6.13. Simulation results for a D_{Gr} value 10 times higher than the nominal value, conducted to examine the effect of Li diffusivity in the active material. (A-E) Evolution of local Li site fraction in the 40% Gr electrode during C/4 charging at different SOCs. (F) Local SE potential in the electrode.

The second type of gradient in local SOC is caused by the solid-state diffusion limitation of Li within graphite domains (Figure 6.7H). To demonstrate this effect, we simulated the performance of the 40% Gr electrode with a hypothetical value of Li diffusivity in graphite that is 10 times higher than the actual value. No other model parameter was changed. The results are summarized in Figure 6.13, which show that the second type of gradient in local SOC attenuates significantly as the diffusivity of Li in graphite in increased. We note that although the solid-state diffusivity is an intrinsic property of the active material, the diffusion kinetics can be accelerated by designing microstructures that ensure short transport distances of Li away from the nearest SE/graphite interface. We also note that the solid-state diffusion limitation is even more severe in simulations of the 80% Gr electrode (Supporting Information), which is illustrated by the presence of large SOC gradients (Figure S18). This results in a smaller accessible capacity delivered by the electrode compared to the 40% Gr electrode. Both types of gradients become less severe as the C-rate is decreased to C/16 as shown in Figure 6.14. This is consistent with the experimental

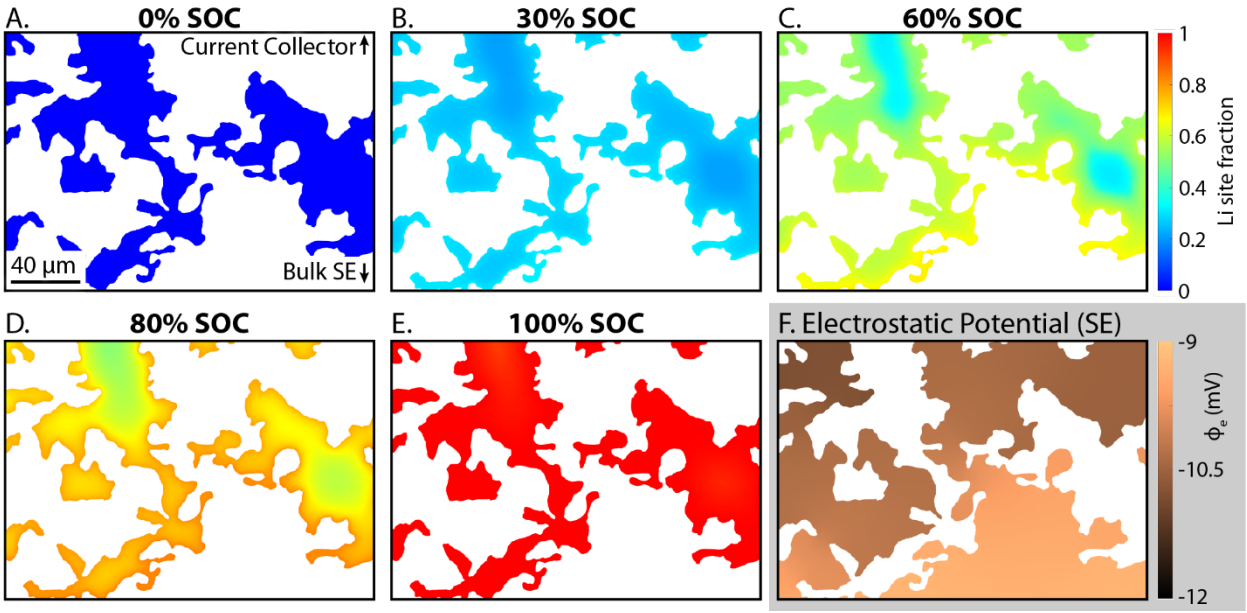

Figure 6.14. (A-E) Evolution of local Li site fraction in the 40% Gr electrode during C/16 charging at different SOCs. (F) Local SE potential in the electrode.

observations. We also note that both ionic conductivity in the SE and solid-state diffusivity depend exponentially on temperature and therefore both of these sources of inhomogeneity in local SOC will become exacerbated under low temperature operation.

In conclusion, in this work we probed the mechanistic origins of rate limitations within solid-state composite electrodes. *Operando* video microscopy was used to directly observe gradients in local SOC within composite electrodes during lithiation, which were correlated with increasingly severe rate performance limitations as the active material/SE ratio is increased. Electrochemical dynamics modeling was used to rationalize the trends in the *operando* microscopy data and identify the specific electrode properties that limit the rate performance. The following key understandings and design rules for composite electrodes were developed:

1. Rate capability limitations exist in solid-state composite electrodes, which are a function of the active material/SE ratio and electrode thickness (both of which affect the areal capacity). As C-rate increases, an increasingly sloping voltage profile is observed, and the CC portion of lithiation is reduced in duration. This leads to a tradeoff between energy density and power performance.

2. Through *operando* optical visualization, we observe that the rate-capability limitations are associated with heterogeneity in local SOC within the active material. Specifically, two gradients in local SOC are observed. First, the local SOC decreases away from the bulk SE, which is attributed to the electrostatic potential drop within the SE phase. Second, the local SOC decreases from the active material/SE interface into the interior of the active material region, which is attributed to solid-state diffusion.

3. The relative importance of these two contributions to heterogeneity in local SOC are a function of both the electrode microstructure and the C-rate. Specifically, at low active material fractions, the SE channels are highly interconnected throughout the electrode. This microstructure results in a lower impedance for ionic transport, which reduces the potential drop through the electrode depth at high C-rates. However, as the active material fraction is increased, the average active material domain sizes become larger and the SE becomes less interconnected. These microstructural effects lead to more significant gradients in local SOC in the through-plane direction and within active material domains, both of which limit rate performance.

4. To describe the origins of gradients in local SOC, an electrochemical dynamics model was constructed. The gradient in local SOC along the depth of the electrode was attributed to the drop in electrostatic potential within the SE phase of the composite electrode. This causes local variations of overpotential that result in the observed current focusing, despite the lack of concentration gradients within the single-ion-conducting SE. The gradient within the active material region was confirmed to be a consequence of solid-state diffusion.

5. The results of this study illustrate design rules to overcome rate limitations in SSB composite electrodes. To reduce gradients in the local SOC away from the bulk SE, effective strategies include increasing SE ionic conductivity or tuning the composite electrode microstructure to decrease the electrostatic potential drop at a given C-rate. To reduce gradients in the local SOC within the active material, effective strategies include choosing active materials with high Li diffusivity and tuning the microstructure to

minimize the distance between the interior of the active material and its interface with the SE.

6. While graphite was used here as a model system, the conclusions and design rules described above are applicable to a range of composite electrodes in SSBs, including cathode materials. Simulations similar to those presented here, with appropriate parameterization, can further inform how the microstructures should be designed to optimize rate performance

Chapter 7

Conclusions and Future Work

Conclusions

Battery metrics such as cycle life and charge rate are dependent on a complex interplay between the electronic, chemical, and mechanical evolution of battery interfaces and electrodes throughout cycling. Herein, a suite of *operando* analysis techniques has been used to probe these phenomena in both Li metal anodes and composite electrodes and the following key insights have been developed:

1. In chapter 3, we utilized Al_2O_3 interlayers as a model system to improve our understanding of the mechanisms behind SE stabilization and the electro-chemo-mechanical phenomena that lead to eventual decay of artificial SEI layers. Two main effects were observed that limit the long-term effectiveness of Al_2O_3 and similar artificial SEI layers. 1) During early stage cycling the low ionic conductivity of Al_2O_3 increases the overall cell impedance. 2) With extended cycling the ALD layer fractures and is no longer able to passivate the LGPS surface.
2. In chapter 4, multi-modal *operando* analysis was employed to provide a direct comparison of the differences in SEI formation and Li plating between unstable (LGPS)

and kinetically stable (LPSCl) sulfide SEs. In kinetically stable SE, after initial SEI formation, the interface stabilizes and Li metal plating initiates. In contrast, for unstable SEs, the interface does not stabilize and the SEI continues to grow throughout the charging process. These results have significant implications on energy density and cycle life of sulfide SSBs, particularly in anode-free configurations. Because the Li reservoir comes entirely from the cathode, Faradaic inefficiency in the first half cycle directly reduces energy density. As a result of this loss in Li inventory, SEs such as LGPS are impractical for use in anode-free cell configurations, unless this instability can be addressed. In contrast, kinetically stable electrolytes such as LPSCl have significantly higher Faradaic efficiency and correspondingly minimal Li loss during the initial SEI formation.

3. In chapter 5, we demonstrate that solid-state batteries using molten Li anodes are compatible with high-rate charging. CCDs measured were an order of magnitude higher than expected if solid Li CCD trends are followed due to a step increase in CCD across the melting point of Li. This step increase is attributed to step changes in the mechanical properties of Li, which allow for pressure relaxation within the Li electrode that prevents LLZO fracture and Li filament formation. These results shine new light on mechanisms of Li filament propagation, show the promise of a molten Li cell for high-rate applications, and inform future efforts in developing quantitative models of the mechanisms behind filament formation.
4. In chapter 6, the mechanistic origins of energy/power density tradeoffs within solid-state composite electrodes were investigated. Operando video microscopy was used to directly observe gradients in local SOC within composite electrodes during lithiation, which were

correlated with increasingly severe rate performance limitations as the active material/SE ratio is increased. Electrochemical dynamics modeling was used to rationalize the trends in the operando microscopy data and identify the specific electrode properties that limit the rate performance, including ionic conductivity of the SE and the Li diffusivity of the active material. While graphite was used here as a model system, the conclusions and design rules described above are applicable to a range of composite electrodes in SSBs, including cathode materials.

Future Work

The increased understanding developed in this work of the mechanisms that limit SSB cycle life and rate performance provide design rules for future development of longer lasting batteries that are compatible with fast charging. Specifically, the following future work stems from these design rules:

1. Interlayers deposited at the Li/SE interface have potential for improving interface stability and enabling extended cycle life. However, realizing these improvements requires interlayers with the following properties: 1) high ionic conductivities, 2) minimal volume changes when in contact with Li metal, and 3) improved mechanical properties. Recent development of ALD and MLD processes for SE films that are stable against Li metal are particularly promising as potential interlayers.[170,171]
2. LPSCl and other kinetically stable SEs show promise for anode free SSB configurations due to limited SEI formation during the first cycle. Further studies understanding interfacial evolution throughout extended cycling and the roll of stack

pressure, dead Li, Li wettability, and surface roughness on Faradaic efficiency are key to realizing long cycle life anode free SSBs.

3. The molten Li/LLZO system provides insight into the mechanical mechanisms behind Li penetration of SEs. This work can inform future efforts in developing quantitative models of the mechanisms behind filament formation. By better understanding these mechanisms, interface microstructure and chemistry can be tuned to prevent filament nucleation and enable higher current densities in solid Li systems.

4. To improve rate performance of composite electrodes, Li transport limitations in both the SE and graphite phases must be addressed. To reduce gradients in the local SOC away from the bulk SE, effective strategies include increasing SE ionic conductivity or tuning the composite electrode microstructure to decrease the electrostatic potential drop at a given C-rate. To reduce gradients in the local SOC within the active material, effective strategies include choosing active materials with high Li diffusivity and tuning the microstructure to minimize the distance between the interior of the active material and its interface with the SE.

In summary, the work contained in this thesis reveals many exiting directions for rational design of high performance SSBs, as well as exhibiting a range of techniques that can be built upon for further mechanistic studies to improve our understanding of the electro-chemo-mechanical phenomena governing SSB performance.

Bibliography

(1) Ritchie, H.; Roser, M. Fossil Fuels. *Our World in Data* **2017**.

(2) Deng, J.; Bae, C.; Denlinger, A.; Miller, T. Electric Vehicles Batteries: Requirements and Challenges. *Joule* **2020**, *4* (3), 511–515. https://doi.org/10.1016/j.joule.2020.01.013.

(3) Lutsey, N. The Rise of Electric Vehicles: The Second Million. *The International Council on Clean Transportation* **2017**.

(4) Wang, M. J.; Kazyak, E.; Dasgupta, N. P.; Sakamoto, J. Transitioning Solid-State Batteries from Lab to Market: Linking Electro-Chemo-Mechanics with Practical Considerations. *Joule* **2021**, *5* (6), 1371–1390. https://doi.org/10.1016/j.joule.2021.04.001.

(5) Davis, A. L.; Garcia-Mendez, R.; Wood, K. N.; Kazyak, E.; Chen, K.-H.; Teeter, G.; Sakamoto, J.; Dasgupta, N. P. Electro-Chemo-Mechanical Evolution of Sulfide Solid Electrolyte/Li Metal Interfaces: *Operando* Analysis and ALD Interlayer Effects. *Journal of Materials Chemistry A* **2020**, *8* (13), 6291–6302. https://doi.org/10.1039/C9TA11508K.

(6) Davis, A. L.; Kazyak, E.; Liao, D. W.; Wood, K. N.; Dasgupta, N. P. Operando Analysis of Interphase Dynamics in Anode-Free Solid-State Batteries with Sulfide Electrolytes. *Journal of The Electrochemical Society* **2021**, *168* (7), 070557. https://doi.org/10.1149/1945-7111/ac163d.

(7) Kinzer, B.; Davis, A. L.; Krauskopf, T.; Hartmann, H.; LePage, W. S.; Kazyak, E.; Janek, J.; Dasgupta, N. P.; Sakamoto, J. Operando Analysis of the Molten Li|LLZO Interface: Understanding How the Physical Properties of Li Affect the Critical Current Density. *Matter* **2021**, *4* (6), 1947–1961. https://doi.org/10.1016/j.matt.2021.04.016.

(8) Davis, A. L.; Goel, V.; Liao, D. W.; Main, M. N.; Kazyak, E.; Lee, J.; Thornton, K.; Dasgupta, N. P. Rate Limitations in Composite Solid-State Battery Electrodes: Revealing Heterogeneity with *Operando* Microscopy. *ACS Energy Letters* **2021**, 2993–3003. https://doi.org/10.1021/acsenergylett.1c01063.

(9) Abraham, K. M. Prospects and Limits of Energy Storage in Batteries. *Journal of Physical Chemistry Letters*. American Chemical Society March 5, 2015, pp 830–844. https://doi.org/10.1021/jz5026273.

(10) Wu, F.; Maier, J.; Yu, Y. Guidelines and Trends for Next-Generation Rechargeable Lithium and Lithium-Ion Batteries. *Chemical Society Reviews*. Royal Society of Chemistry March 7, 2020, pp 1569–1614. https://doi.org/10.1039/c7cs00863e.

(11) Guo, Y.; Li, H.; Zhai, T. Reviving Lithium-Metal Anodes for Next-Generation High-Energy Batteries. *Advanced Materials*. Wiley-VCH Verlag August 4, 2017, p 1700007. https://doi.org/10.1002/adma.201700007.

(12) Cheng, X. B.; Zhang, R.; Zhao, C. Z.; Zhang, Q. Toward Safe Lithium Metal Anode in Rechargeable Batteries: A Review. *Chemical Reviews*. American Chemical Society August 9, 2017, pp 10403–10473. https://doi.org/10.1021/acs.chemrev.7b00115.

(13) Wood, K. N.; Kazyak, E.; Chadwick, A. F.; Chen, K.-H.; Zhang, J.-G.; Thornton, K.; Dasgupta, N. P. Dendrites and Pits: Untangling the Complex Behavior of Lithium Metal Anodes through Operando Video Microscopy. *ACS Central Science* **2016**, *2* (11), 790–801. https://doi.org/10.1021/acscentsci.6b00260.

(14) Chen, K. H.; Wood, K. N.; Kazyak, E.; Lepage, W. S.; Davis, A. L.; Sanchez, A. J.; Dasgupta, N. P. Dead Lithium: Mass Transport Effects on Voltage, Capacity, and Failure of Lithium Metal Anodes. *Journal of Materials Chemistry A* **2017**, *5* (23), 11671–11681. https://doi.org/10.1039/c7ta00371d.

(15) Neudecker, B. J.; Dudney, N. J.; Bates, J. B. "Lithium-Free" Thin-Film Battery with In Situ Plated Li Anode. *Journal of The Electrochemical Society* **2000**, *147* (2), 517. https://doi.org/10.1149/1.1393226.

(16) Lee, Y. G.; Fujiki, S.; Jung, C.; Suzuki, N.; Yashiro, N.; Omoda, R.; Ko, D. S.; Shiratsuchi, T.; Sugimoto, T.; Ryu, S.; Ku, J. H.; Watanabe, T.; Park, Y.; Aihara, Y.; Im, D.; Han, I. T. High-Energy Long-Cycling All-Solid-State Lithium Metal Batteries Enabled by Silver–Carbon Composite Anodes. *Nature Energy* **2020**, *5* (4), 299–308. https://doi.org/10.1038/s41560-020-0575-z.

(17) Kanno, R. Solid Electrolytes Open Doors to Solid-State Batteries. *Tokyo Tech News* **2016**.

(18) Bachman, J. C.; Muy, S.; Grimaud, A.; Chang, H. H.; Pour, N.; Lux, S. F.; Paschos, O.; Maglia, F.; Lupart, S.; Lamp, P.; Giordano, L.; Shao-Horn, Y. Inorganic Solid-State Electrolytes for Lithium Batteries: Mechanisms and Properties Governing Ion Conduction. *Chemical Reviews*. American Chemical Society January 13, 2016, pp 140–162. https://doi.org/10.1021/acs.chemrev.5b00563.

(19) Zheng, F.; Kotobuki, M.; Song, S.; Lai, M. O.; Lu, L. Review on Solid Electrolytes for All-Solid-State Lithium-Ion Batteries. *Journal of Power Sources* **2018**, *389*, 198–213. https://doi.org/10.1016/j.jpowsour.2018.04.022.

(20) Zhu, Y.; He, X.; Mo, Y. Origin of Outstanding Stability in the Lithium Solid Electrolyte Materials: Insights from Thermodynamic Analyses Based on First-Principles Calculations. *ACS Applied Materials & Interfaces* **2015**, *7* (42), 23685–23693. https://doi.org/10.1021/acsami.5b07517.

(21) Bron, P.; Roling, B.; Dehnen, S. Impedance Characterization Reveals Mixed Conducting Interphases between Sulfidic Superionic Conductors and Lithium Metal Electrodes.

Journal of Power Sources **2017**, *352*, 127–134. https://doi.org/10.1016/j.jpowsour.2017.03.103.

(22) Kazyak, E.; Garcia-Mendez, R.; LePage, W. S.; Sharafi, A.; Davis, A. L.; Sanchez, A. J.; Chen, K.-H.; Haslam, C.; Sakamoto, J.; Dasgupta, N. P. Li Penetration in Ceramic Solid Electrolytes: Operando Microscopy Analysis of Morphology, Propagation, and Reversibility. *Matter* **2020**, *2* (4), 1025–1048. https://doi.org/10.1016/j.matt.2020.02.008.

(23) Ansell, R. O. *Review The Chemical and Electrochemical Stability of Beta-Alumina*; 1986; Vol. 21.

(24) Krauskopf, T.; Richter, F. H.; Zeier, W. G.; Janek, J. Physicochemical Concepts of the Lithium Metal Anode in Solid-State Batteries. *Chemical Reviews* **2020**, *120* (15), 7745–7794. https://doi.org/10.1021/acs.chemrev.0c00431.

(25) Porz, L.; Swamy, T.; Sheldon, B. W.; Rettenwander, D.; Frömling, T.; Thaman, H. L.; Berendts, S.; Uecker, R.; Carter, W. C.; Chiang, Y.-M. Mechanism of Lithium Metal Penetration through Inorganic Solid Electrolytes. *Advanced Energy Materials* **2017**, *7* (20), 1701003. https://doi.org/10.1002/aenm.201701003.

(26) Barroso-Luque, L.; Tu, Q.; Ceder, G. An Analysis of Solid-State Electrodeposition-Induced Metal Plastic Flow and Predictions of Stress States in Solid Ionic Conductor Defects. *Journal of The Electrochemical Society* **2020**, *167* (2), 020534. https://doi.org/10.1149/1945-7111/ab6c5b.

(27) De Jonghe, L. C.; Feldman, L.; Buechele, A. Failure Modes of Na-Beta Alumina. *Solid State Ionics* **1981**, *5*, 267–269. https://doi.org/10.1016/0167-2738(81)90244-7.

(28) Feldman, L. A.; De Jonghe, L. C. Initiation of Mode I Degradation in Sodium-Beta Alumina Electrolytes. *Journal of Materials Science* **1982**, *17* (2), 517–524. https://doi.org/10.1007/BF00591486.

(29) Armstrong, R. D.; Dickinson, T.; Turner, J. The Breakdown of β-Alumina Ceramic Electrolyte. *Electrochimica Acta* **1974**, *19*, 187–192. https://doi.org/10.1016/0013-4686(74)85065-6.

(30) Han, F.; Westover, A. S.; Yue, J.; Fan, X.; Wang, F.; Chi, M.; Leonard, D. N.; Dudney, N. J.; Wang, H.; Wang, C. High Electronic Conductivity as the Origin of Lithium Dendrite Formation within Solid Electrolytes. *Nature Energy* **2019**, *4* (3), 187–196. https://doi.org/10.1038/s41560-018-0312-z.

(31) De Jonghe, L. C.; Feldman, L.; Beuchele, A. Slow Degradation and Electron Conduction in Sodium/Beta-Aluminas. *Journal of Materials Science* **1981**, *16* (3), 780–786. https://doi.org/10.1007/BF02402796.

(32) Sakuda, A.; Hayashi, A.; Tatsumisago, M. Sulfide Solid Electrolyte with Favorable Mechanical Property for All-Solid-State Lithium Battery. *Scientific Reports* **2013**, *3* (1), 2261. https://doi.org/10.1038/srep02261.

(33) Balaish, M.; Gonzalez-Rosillo, J. C.; Kim, K. J.; Zhu, Y.; Hood, Z. D.; Rupp, J. L. M. Processing Thin but Robust Electrolytes for Solid-State Batteries. *Nature Energy*. Nature Research March 1, 2021, pp 227–239. https://doi.org/10.1038/s41560-020-00759-5.

(34) Tatsumisago, M.; Nagao, M.; Hayashi, A. Recent Development of Sulfide Solid Electrolytes and Interfacial Modification for All-Solid-State Rechargeable Lithium Batteries. *Journal of Asian Ceramic Societies* **2013**, *1* (1), 17–25. https://doi.org/10.1016/j.jascer.2013.03.005.

(35) Lim, H.-D.; Park, J.-H.; Shin, H.-J.; Jeong, J.; Kim, J. T.; Nam, K.-W.; Jung, H.-G.; Chung, K. Y. A Review of Challenges and Issues Concerning Interfaces for All-Solid-State Batteries. *Energy Storage Materials* **2020**, *25*, 224–250. https://doi.org/10.1016/j.ensm.2019.10.011.

(36) Xu, L.; Tang, S.; Cheng, Y.; Wang, K.; Liang, J.; Liu, C.; Cao, Y.-C.; Wei, F.; Mai, L. Interfaces in Solid-State Lithium Batteries. *Joule* **2018**, *2* (10), 1991–2015. https://doi.org/10.1016/j.joule.2018.07.009.

(37) Yamagishi, Y.; Morita, H.; Nomura, Y.; Igaki, E. Visualizing Lithiation of Graphite Composite Anodes in All-Solid-State Batteries Using *Operando* Time-of-Flight Secondary Ion Mass Spectrometry. *The Journal of Physical Chemistry Letters* **2021**, *12* (19), 4623–4627. https://doi.org/10.1021/acs.jpclett.1c01089.

(38) Kato, Y.; Shiotani, S.; Morita, K.; Suzuki, K.; Hirayama, M.; Kanno, R. All-Solid-State Batteries with Thick Electrode Configurations. *The Journal of Physical Chemistry Letters* **2018**, *9* (3), 607–613. https://doi.org/10.1021/acs.jpclett.7b02880.

(39) Sanchez, A. J.; Kazyak, E.; Chen, Y.; Chen, K.-H.; Pattison, E. R.; Dasgupta, N. P. Plan-View *Operando* Video Microscopy of Li Metal Anodes: Identifying the Coupled Relationships among Nucleation, Morphology, and Reversibility. *ACS Energy Letters* **2020**, *5* (3), 994–1004. https://doi.org/10.1021/acsenergylett.0c00215.

(40) Wood, K. N.; Steirer, K. X.; Hafner, S. E.; Ban, C.; Santhanagopalan, S.; Lee, S.-H.; Teeter, G. Operando X-Ray Photoelectron Spectroscopy of Solid Electrolyte Interphase Formation and Evolution in Li2S-P2S5 Solid-State Electrolytes. *Nature Communications* **2018**, *9* (1), 2490. https://doi.org/10.1038/s41467-018-04762-z.

(41) Kamaya, N.; Homma, K.; Yamakawa, Y.; Hirayama, M.; Kanno, R.; Yonemura, M.; Kamiyama, T.; Kato, Y.; Hama, S.; Kawamoto, K.; Mitsui, A. A Lithium Superionic Conductor. *Nature Materials* **2011**, *10* (9), 682–686. https://doi.org/10.1038/nmat3066.

(42) Seino, Y.; Ota, T.; Takada, K.; Hayashi, A.; Tatsumisago, M. A Sulphide Lithium Super Ion Conductor Is Superior to Liquid Ion Conductors for Use in Rechargeable Batteries. *Energy Environ. Sci.* **2014**, *7* (2), 627–631. https://doi.org/10.1039/C3EE41655K.

(43) Chen, S.; Xie, D.; Liu, G.; Mwizerwa, J. P.; Zhang, Q.; Zhao, Y.; Xu, X.; Yao, X. Sulfide Solid Electrolytes for All-Solid-State Lithium Batteries: Structure, Conductivity, Stability

and Application. *Energy Storage Materials* **2018**, *14* (February), 58–74. https://doi.org/10.1016/j.ensm.2018.02.020.

(44) Park, K. H.; Bai, Q.; Kim, D. H.; Oh, D. Y.; Zhu, Y.; Mo, Y.; Jung, Y. S. Design Strategies, Practical Considerations, and New Solution Processes of Sulfide Solid Electrolytes for All-Solid-State Batteries. *Advanced Energy Materials* **2018**, *8* (18), 1800035. https://doi.org/10.1002/aenm.201800035.

(45) Kato, Y.; Hori, S.; Saito, T.; Suzuki, K.; Hirayama, M.; Mitsui, A.; Yonemura, M.; Iba, H.; Kanno, R. High-Power All-Solid-State Batteries Using Sulfide Superionic Conductors. *Nature Energy* **2016**, *1* (4), 16030. https://doi.org/10.1038/nenergy.2016.30.

(46) Han, F.; Zhu, Y.; He, X.; Mo, Y.; Wang, C. Electrochemical Stability of Li 10 GeP 2 S 12 and Li 7 La 3 Zr 2 O 12 Solid Electrolytes. *Advanced Energy Materials* **2016**, *6* (8), 1501590. https://doi.org/10.1002/aenm.201501590.

(47) Zhu, Y.; He, X.; Mo, Y. First Principles Study on Electrochemical and Chemical Stability of Solid Electrolyte–Electrode Interfaces in All-Solid-State Li-Ion Batteries. *Journal of Materials Chemistry A* **2016**, *4* (9), 3253–3266. https://doi.org/10.1039/C5TA08574H.

(48) Richards, W. D.; Miara, L. J.; Wang, Y.; Kim, J. C.; Ceder, G. Interface Stability in Solid-State Batteries. *Chemistry of Materials* **2016**, *28* (1), 266–273. https://doi.org/10.1021/acs.chemmater.5b04082.

(49) Wu, B.; Wang, S.; Evans IV, W. J.; Deng, D. Z.; Yang, J.; Xiao, J. Interfacial Behaviours between Lithium Ion Conductors and Electrode Materials in Various Battery Systems. *Journal of Materials Chemistry A* **2016**, *4* (40), 15266–15280. https://doi.org/10.1039/C6TA05439K.

(50) Sang, L.; Haasch, R. T.; Gewirth, A. A.; Nuzzo, R. G. Evolution at the Solid Electrolyte/Gold Electrode Interface during Lithium Deposition and Stripping. *Chemistry of Materials* **2017**, *29* (7), 3029–3037. https://doi.org/10.1021/acs.chemmater.7b00034.

(51) Camacho-Forero, L. E.; Balbuena, P. B. Exploring Interfacial Stability of Solid-State Electrolytes at the Lithium-Metal Anode Surface. *Journal of Power Sources* **2018**, *396* (July), 782–790. https://doi.org/10.1016/j.jpowsour.2018.06.092.

(52) Chen, B.; Ju, J.; Ma, J.; Zhang, J.; Xiao, R.; Cui, G.; Chen, L. An Insight into Intrinsic Interfacial Properties between Li Metals and Li 10 GeP 2 S 12 Solid Electrolytes. *Physical Chemistry Chemical Physics* **2017**, *19* (46), 31436–31442. https://doi.org/10.1039/C7CP05253G.

(53) Wenzel, S.; Weber, D. A.; Leichtweiss, T.; Busche, M. R.; Sann, J.; Janek, J. Interphase Formation and Degradation of Charge Transfer Kinetics between a Lithium Metal Anode and Highly Crystalline Li 7 P 3 S 11 Solid Electrolyte. *Solid State Ionics* **2016**, *286*, 24–33. https://doi.org/10.1016/j.ssi.2015.11.034.

(54) Wenzel, S.; Randau, S.; Leichtweiß, T.; Weber, D. A.; Sann, J.; Zeier, W. G.; Janek, J. J. Direct Observation of the Interfacial Instability of the Fast Ionic Conductor Li 10 GeP 2 S 12 at the Lithium Metal Anode. *Chemistry of Materials* **2016**, *28* (7), 2400–2407. https://doi.org/10.1021/acs.chemmater.6b00610.

(55) Sakuma, M.; Suzuki, K.; Hirayama, M.; Kanno, R. Reactions at the Electrode/Electrolyte Interface of All-Solid-State Lithium Batteries Incorporating Li–M (M = Sn, Si) Alloy Electrodes and Sulfide-Based Solid Electrolytes. *Solid State Ionics* **2016**, *285*, 101–105. https://doi.org/10.1016/j.ssi.2015.07.010.

(56) Mo, Y.; Ong, S. P.; Ceder, G. First Principles Study of the Li 10GeP 2S 12 Lithium Super Ionic Conductor Material. In *Chemistry of Materials*; 2012; Vol. 24, pp 15–17. https://doi.org/10.1021/cm203303y.

(57) Ma, C.; Cheng, Y.; Yin, K.; Luo, J.; Sharafi, A.; Sakamoto, J.; Li, J.; More, K. L.; Dudney, N. J.; Chi, M. Interfacial Stability of Li Metal-Solid Electrolyte Elucidated via in Situ Electron Microscopy. *Nano Letters* **2016**, *16* (11), 7030–7036. https://doi.org/10.1021/acs.nanolett.6b03223.

(58) Zhang, Z.; Chen, S.; Yang, J.; Wang, J.; Yao, L.; Yao, X.; Cui, P.; Xu, X. Interface Re-Engineering of Li 10 GeP 2 S 12 Electrolyte and Lithium Anode for All-Solid-State Lithium Batteries with Ultralong Cycle Life. *ACS Applied Materials & Interfaces* **2018**, *10* (3), 2556–2565. https://doi.org/10.1021/acsami.7b16176.

(59) Umeshbabu, E.; Zheng, B.; Zhu, J.; Wang, H.; Li, Y.; Yang, Y. Stable Cycling Lithium–Sulfur Solid Batteries with Enhanced Li/Li 10 GeP 2 S 12 Solid Electrolyte Interface Stability. *ACS Applied Materials & Interfaces* **2019**, *11* (20), 18436–18447. https://doi.org/10.1021/acsami.9b03726.

(60) Wang, C.; Adair, K. R.; Liang, J.; Li, X.; Sun, Y.; Li, X.; Wang, J.; Sun, Q.; Zhao, F.; Lin, X.; Li, R.; Huang, H.; Zhang, L.; Yang, R.; Lu, S.; Sun, X. Solid-State Plastic Crystal Electrolytes: Effective Protection Interlayers for Sulfide-Based All-Solid-State Lithium Metal Batteries. *Advanced Functional Materials* **2019**, *29* (26), 1900392. https://doi.org/10.1002/adfm.201900392.

(61) Gao, Y.; Wang, D.; Li, Y. C.; Yu, Z.; Mallouk, T. E.; Wang, D. Salt-Based Organic-Inorganic Nanocomposites: Towards A Stable Lithium Metal/Li 10 GeP 2 S 12 Solid Electrolyte Interface. *Angewandte Chemie International Edition* **2018**, *57* (41), 13608–13612. https://doi.org/10.1002/anie.201807304.

(62) Chien, P.-H.; Feng, X.; Tang, M.; Rosenberg, J. T.; O'Neill, S.; Zheng, J.; Grant, S. C.; Hu, Y.-Y. Li Distribution Heterogeneity in Solid Electrolyte Li 10 GeP 2 S 12 upon Electrochemical Cycling Probed by 7 Li MRI. *The Journal of Physical Chemistry Letters* **2018**, *9* (8), 1990–1998. https://doi.org/10.1021/acs.jpclett.8b00240.

(63) Kazyak, E.; Wood, K. N.; Dasgupta, N. P. Improved Cycle Life and Stability of Lithium Metal Anodes through Ultrathin Atomic Layer Deposition Surface Treatments. *Chemistry of Materials* **2015**, *27* (18), 6457–6462. https://doi.org/10.1021/acs.chemmater.5b02789.

(64) Cao, Y.; Meng, X.; Elam, J. W. Atomic Layer Deposition of Li x Al y S Solid-State Electrolytes for Stabilizing Lithium-Metal Anodes. *ChemElectroChem* **2016**, *3* (6), 858–863. https://doi.org/10.1002/celc.201600139.

(65) Liu, J.; Sun, X. Elegant Design of Electrode and Electrode/Electrolyte Interface in Lithium-Ion Batteries by Atomic Layer Deposition. *Nanotechnology* **2015**, *26* (2), 024001. https://doi.org/10.1088/0957-4484/26/2/024001.

(66) Meng, X.; Yang, X.-Q.; Sun, X. Emerging Applications of Atomic Layer Deposition for Lithium-Ion Battery Studies. *Advanced Materials* **2012**, *24* (27), 3589–3615. https://doi.org/10.1002/adma.201200397.

(67) Lin, C.-F.; Kozen, A. C.; Noked, M.; Liu, C.; Rubloff, G. W. ALD Protection of Li-Metal Anode Surfaces - Quantifying and Preventing Chemical and Electrochemical Corrosion in Organic Solvent. *Advanced Materials Interfaces* **2016**, *3* (21), 1600426. https://doi.org/10.1002/admi.201600426.

(68) Han, X.; Gong, Y.; Fu, K.; He, X.; Hitz, G. T.; Dai, J.; Pearse, A.; Liu, B.; Wang, H.; Rubloff, G.; Mo, Y.; Thangadurai, V.; Wachsman, E. D.; Hu, L. Negating Interfacial Impedance in Garnet-Based Solid-State Li Metal Batteries. *Nature Materials* **2017**, *16* (5), 572–579. https://doi.org/10.1038/nmat4821.

(69) Dasgupta, N. P.; Lee, H.-B.-R.; Bent, S. F.; Weiss, P. S. Recent Advances in Atomic Layer Deposition. *Chemistry of Materials* **2016**, *28* (7), 1943–1947. https://doi.org/10.1021/acs.chemmater.6b00673.

(70) George, S. M. Atomic Layer Deposition: An Overview. *Chemical Reviews* **2010**, *110* (1), 111–131. https://doi.org/10.1021/cr900056b.

(71) Elam, J. W.; Dasgupta, N. P.; Prinz, F. B. ALD for Clean Energy Conversion, Utilization, and Storage. *MRS Bulletin* **2011**, *36* (11), 899–906. https://doi.org/10.1557/mrs.2011.265.

(72) Chen, L.; Connell, J. G.; Nie, A.; Huang, Z.; Zavadil, K. R.; Klavetter, K. C.; Yuan, Y.; Sharifi-Asl, S.; Shahbazian-Yassar, R.; Libera, J. A.; Mane, A. U.; Elam, J. W. Lithium Metal Protected by Atomic Layer Deposition Metal Oxide for High Performance Anodes. *Journal of Materials Chemistry A* **2017**, *5* (24), 12297–12309. https://doi.org/10.1039/c7ta03116e.

(73) Neudeck, S.; Mazilkin, A.; Reitz, C.; Hartmann, P.; Janek, J.; Brezesinski, T. Effect of Low-Temperature Al 2 O 3 ALD Coating on Ni-Rich Layered Oxide Composite Cathode on the Long-Term Cycling Performance of Lithium-Ion Batteries. *Scientific Reports* **2019**, *9* (1), 1–11. https://doi.org/10.1038/s41598-019-41767-0.

(74) Han, B.; Key, B.; Lipton, A. S.; Vaughey, J. T.; Hughes, B.; Trevey, J.; Dogan, F. Influence of Coating Protocols on Alumina-Coated Cathode Material: Atomic Layer Deposition versus Wet-Chemical Coating. *Journal of The Electrochemical Society* **2019**, *166* (15), A3679–A3684. https://doi.org/10.1149/2.0681915jes.

(75) Jung, Y. S.; Cavanagh, A. S.; Dillon, A. C.; Groner, M. D.; George, S. M.; Lee, S. H. Enhanced Stability of LiCoO2 Cathodes in Lithium-Ion Batteries Using Surface Modification by Atomic Layer Deposition. *Journal of the Electrochemical Society* **2010**, *157* (1), 75–81. https://doi.org/10.1149/1.3258274.

(76) Yan, P.; Zheng, J.; Zhang, X.; Xu, R.; Amine, K.; Xiao, J.; Zhang, J. G.; Wang, C. M. Atomic to Nanoscale Investigation of Functionalities of an Al2O3 Coating Layer on a Cathode for Enhanced Battery Performance. *Chemistry of Materials* **2016**, *28* (3), 857–863. https://doi.org/10.1021/acs.chemmater.5b04301.

(77) Wang, C.; Zhao, Y.; Sun, Q.; Li, X.; Liu, Y.; Liang, J.; Li, X.; Lin, X.; Li, R.; Adair, K. R.; Li, Z.; Yang, R.; Lu, S.; Sun, X. Stabilizing Interface between Li10SnP2S12 and Li Metal by Molecular Layer Deposition. *Nano Energy* **2018**, *53* (July), 168–174. https://doi.org/10.1016/J.NANOEN.2018.08.030.

(78) Sang, L.; Bassett, K. L.; Castro, F. C.; Young, M. J.; Chen, L.; Haasch, R. T.; Elam, J. W.; Dravid, V. P.; Nuzzo, R. G.; Gewirth, A. A. Understanding the Effect of Interlayers at the Thiophosphate Solid Electrolyte/Lithium Interface for All-Solid-State Li Batteries. *Chemistry of Materials* **2018**, *30* (24), 8747–8756. https://doi.org/10.1021/acs.chemmater.8b02368.

(79) LePage, W. S.; Chen, Y.; Kazyak, E.; Chen, K.; Sanchez, A. J.; Poli, A.; Arruda, E. M.; Thouless, M. D.; Dasgupta, N. P. Lithium Mechanics: Roles of Strain Rate and Temperature and Implications for Lithium Metal Batteries. *Journal of The Electrochemical Society* **2019**, *166* (2), A89–A97. https://doi.org/10.1149/2.0221902jes.

(80) Wu, F.; Fitzhugh, W.; Ye, L.; Ning, J.; Li, X. Advanced Sulfide Solid Electrolyte by Core-Shell Structural Design. *Nature Communications* **2018**, *9* (1), 1–11. https://doi.org/10.1038/s41467-018-06123-2.

(81) Jain, A.; Ong, S. P.; Hautier, G.; Chen, W.; Richards, W. D.; Dacek, S.; Cholia, S.; Gunter, D.; Skinner, D.; Ceder, G.; Persson, K. A. Commentary: The Materials Project: A Materials Genome Approach to Accelerating Materials Innovation. *APL Materials* **2013**, *1* (1). https://doi.org/10.1063/1.4812323.

(82) Zhu, Y.; He, X.; Mo, Y. Strategies Based on Nitride Materials Chemistry to Stabilize Li Metal Anode. *Advanced Science* **2017**, *4* (8), 1–11. https://doi.org/10.1002/advs.201600517.

(83) Liu, Y.; Hudak, N. S.; Huber, D. L.; Limmer, S. J.; Sullivan, J. P.; Huang, J. Y. In Situ Transmission Electron Microscopy Observation of Pulverization of Aluminum Nanowires and Evolution of the Thin Surface Al2O3 Layers during Lithiation-Delithiation Cycles. *Nano Letters* **2011**, *11* (10), 4188–4194. https://doi.org/10.1021/nl202088h.

(84) Hao, S.; Wolverton, C. Lithium Transport in Amorphous Al2O3 and AlF 3 for Discovery of Battery Coatings. *Journal of Physical Chemistry C* **2013**, *117* (16), 8009–8013. https://doi.org/10.1021/jp311982d.

(85) Park, J. S.; Meng, X.; Elam, J. W.; Hao, S.; Wolverton, C.; Kim, C.; Cabana, J. Ultrathin Lithium-Ion Conducting Coatings for Increased Interfacial Stability in High Voltage Lithium-Ion Batteries. *Chemistry of Materials* **2014**, *26* (10), 3128–3134. https://doi.org/10.1021/cm500512n.

(86) Jung, S. C.; Han, Y. K. How Do Li Atoms Pass through the Al2O3 Coating Layer during Lithiation in Li-Ion Batteries? *Journal of Physical Chemistry Letters* **2013**, *4* (16), 2681–2685. https://doi.org/10.1021/jz401231e.

(87) Wood, K. N.; Teeter, G. XPS on Li-Battery-Related Compounds: Analysis of Inorganic SEI Phases and a Methodology for Charge Correction. *ACS Applied Energy Materials* **2018**, *1* (9), 4493–4504. https://doi.org/10.1021/acsaem.8b00406.

(88) Gupta, A.; Kazyak, E.; Craig, N.; Christensen, J.; Dasgupta, N. P.; Sakamoto, J. Evaluating the Effects of Temperature and Pressure on Li/PEO-LiTFSI Interfacial Stability and Kinetics. *Journal of the Electrochemical Society* **2018**, *165* (11), A2801–A2806. https://doi.org/10.1149/2.0901811jes.

(89) Wood, K. N.; Noked, M.; Dasgupta, N. P. Lithium Metal Anodes: Toward an Improved Understanding of Coupled Morphological, Electrochemical, and Mechanical Behavior. *ACS Energy Letters* **2017**, *2* (3), 664–672. https://doi.org/10.1021/acsenergylett.6b00650.

(90) Schmid, M.; Steinrück, H. P.; Gottfried, J. M. A New Asymmetric Pseudo-Voigt Function for More Efficient Fitting of XPS Lines. *Surface and Interface Analysis* **2014**, *46* (8), 505–511. https://doi.org/10.1002/sia.5521.

(91) Tan, D. H. S.; Wu, E. A.; Nguyen, H.; Chen, Z.; Marple, M. A. T.; Doux, J. M.; Wang, X.; Yang, H.; Banerjee, A.; Meng, Y. S. Elucidating Reversible Electrochemical Redox of Li6PS5Cl Solid Electrolyte. *ACS Energy Letters* **2019**, 2418–2427. https://doi.org/10.1021/acsenergylett.9b01693.

(92) Strauss, F.; Kitsche, D.; Ma, Y.; Teo, J. H.; Goonetilleke, D.; Janek, J.; Bianchini, M.; Brezesinski, T. Operando Characterization Techniques for All-Solid-State Lithium-Ion Batteries. *Advanced Energy and Sustainability Research* **2021**, 2100004. https://doi.org/10.1002/aesr.202100004.

(93) Wenzel, S.; Sedlmaier, S. J.; Dietrich, C.; Zeier, W. G.; Janek, J. Interfacial Reactivity and Interphase Growth of Argyrodite Solid Electrolytes at Lithium Metal Electrodes. *Solid State Ionics* **2018**, *318* (July 2017), 102–112. https://doi.org/10.1016/j.ssi.2017.07.005.

(94) Schwietert, T. K.; Arszelewska, V. A.; Wang, C.; Yu, C.; Vasileiadis, A.; de Klerk, N. J. J.; Hageman, J.; Hupfer, T.; Kerkamm, I.; Xu, Y.; van der Maas, E.; Kelder, E. M.; Ganapathy, S.; Wagemaker, M. Clarifying the Relationship between Redox Activity and Electrochemical Stability in Solid Electrolytes. *Nature Materials* **2020**, *19* (4), 428–435. https://doi.org/10.1038/s41563-019-0576-0.

(95) Lewis, J. A.; Cortes, F. J. Q.; Liu, Y.; Miers, J. C.; Verma, A.; Vishnugopi, B. S.; Tippens, J.; Prakash, D.; Marchese, T. S.; Han, S. Y.; Lee, C.; Shetty, P. P.; Lee, H. W.;

Shevchenko, P.; de Carlo, F.; Saldana, C.; Mukherjee, P. P.; McDowell, M. T. Linking Void and Interphase Evolution to Electrochemistry in Solid-State Batteries Using Operando X-Ray Tomography. *Nature Materials* **2021**, *20* (4), 503–510. https://doi.org/10.1038/s41563-020-00903-2.

(96) Kasemchainan, J.; Zekoll, S.; Spencer Jolly, D.; Ning, Z.; Hartley, G. O.; Marrow, J.; Bruce, P. G. Critical Stripping Current Leads to Dendrite Formation on Plating in Lithium Anode Solid Electrolyte Cells. *Nature Materials* **2019**, *18* (10), 1105–1111. https://doi.org/10.1038/s41563-019-0438-9.

(97) Lewis, J. A.; Tippens, J.; Cortes, F. J. Q.; McDowell, M. T. Chemo-Mechanical Challenges in Solid-State Batteries. *Trends in Chemistry*. Cell Press December 1, 2019, pp 845–857. https://doi.org/10.1016/j.trechm.2019.06.013.

(98) Tian, Y.; An, Y.; Wei, C.; Jiang, H.; Xiong, S.; Feng, J.; Qian, Y. Recently Advances and Perspectives of Anode-Free Rechargeable Batteries. *Nano Energy*. Elsevier Ltd December 1, 2020, p 105344. https://doi.org/10.1016/j.nanoen.2020.105344.

(99) Wang, M. J.; Carmona, E.; Gupta, A.; Albertus, P.; Sakamoto, J. Enabling "Lithium-Free" Manufacturing of Pure Lithium Metal Solid-State Batteries through in Situ Plating. *Nature Communications* **2020**, *11* (1), 1–9. https://doi.org/10.1038/s41467-020-19004-4.

(100) Weber, R.; Genovese, M.; Louli, A. J.; Hames, S.; Martin, C.; Hill, I. G.; Dahn, J. R. Long Cycle Life and Dendrite-Free Lithium Morphology in Anode-Free Lithium Pouch Cells Enabled by a Dual-Salt Liquid Electrolyte. *Nature Energy* **2019**, *4* (8), 683–689. https://doi.org/10.1038/s41560-019-0428-9.

(101) Fang, C.; Li, J.; Zhang, M.; Zhang, Y.; Yang, F.; Lee, J. Z.; Lee, M. H.; Alvarado, J.; Schroeder, M. A.; Yang, Y.; Lu, B.; Williams, N.; Ceja, M.; Yang, L.; Cai, M.; Gu, J.; Xu, K.; Wang, X.; Meng, Y. S. Quantifying Inactive Lithium in Lithium Metal Batteries. *Nature* **2019**, *572* (7770), 511–515. https://doi.org/10.1038/s41586-019-1481-z.

(102) Albertus, P.; Babinec, S.; Litzelman, S.; Newman, A. Status and Challenges in Enabling the Lithium Metal Electrode for High-Energy and Low-Cost Rechargeable Batteries. *Nature Energy* **2018**, *3* (1), 16–21. https://doi.org/10.1038/s41560-017-0047-2.

(103) Choi, N. S.; Chen, Z.; Freunberger, S. A.; Ji, X.; Sun, Y. K.; Amine, K.; Yushin, G.; Nazar, L. F.; Cho, J.; Bruce, P. G. Challenges Facing Lithium Batteries and Electrical Double-Layer Capacitors. *Angewandte Chemie - International Edition*. John Wiley & Sons, Ltd October 1, 2012, pp 9994–10024. https://doi.org/10.1002/anie.201201429.

(104) Famprikis, T.; Canepa, P.; Dawson, J. A.; Islam, M. S.; Masquelier, C. Fundamentals of Inorganic Solid-State Electrolytes for Batteries. *Nature Materials*. Nature Research December 1, 2019, pp 1278–1291. https://doi.org/10.1038/s41563-019-0431-3.

(105) Hatzell, K. B.; Chen, X. C.; Cobb, C. L.; Dasgupta, N. P.; Dixit, M. B.; Marbella, L. E.; McDowell, M. T.; Mukherjee, P. P.; Verma, A.; Viswanathan, V.; Westover, A. S.; Zeier, W. G. Challenges in Lithium Metal Anodes for Solid-State Batteries. *ACS Energy Letters*.

American Chemical Society March 13, 2020, pp 922–934. https://doi.org/10.1021/acsenergylett.9b02668.

(106) Tsai, C. L.; Roddatis, V.; Chandran, C. V.; Ma, Q.; Uhlenbruck, S.; Bram, M.; Heitjans, P.; Guillon, O. Li7La3Zr2O12 Interface Modification for Li Dendrite Prevention. *ACS Applied Materials and Interfaces* **2016**, *8* (16), 10617–10626. https://doi.org/10.1021/acsami.6b00831.

(107) Taylor, N. J.; Stangeland-Molo, S.; Haslam, C. G.; Sharafi, A.; Thompson, T.; Wang, M.; Garcia-Mendez, R.; Sakamoto, J. Demonstration of High Current Densities and Extended Cycling in the Garnet Li7La3Zr2O12 Solid Electrolyte. *Journal of Power Sources* **2018**, *396* (June), 314–318. https://doi.org/10.1016/j.jpowsour.2018.06.055.

(108) Lee, Y.-G.; Fujiki, S.; Jung, C.; Suzuki, N.; Yashiro, N.; Omoda, R.; Ko, D.-S.; Shiratsuchi, T.; Sugimoto, T.; Ryu, S.; Hwan Ku, J.; Watanabe, T.; Park, Y.; Aihara, Y.; Im, D.; Taek Han, I. High-Energy Long-Cycling All-Solid-State Lithium Metal Batteries Enabled by Silver–Carbon Composite Anodes. https://doi.org/10.1038/s41560-020-0575-z.

(109) Cheng, E. J.; Sharafi, A.; Sakamoto, J. Intergranular Li Metal Propagation through Polycrystalline Li6.25Al0.25La3Zr2O12 Ceramic Electrolyte. *Electrochimica Acta* **2017**, *223*, 85–91. https://doi.org/10.1016/j.electacta.2016.12.018.

(110) Shen, F.; Dixit, M. B.; Xiao, X.; Hatzell, K. B. Effect of Pore Connectivity on Li Dendrite Propagation within LLZO Electrolytes Observed with Synchrotron X-Ray Tomography. *ACS Energy Letters* **2018**, *3* (4), 1056–1061. https://doi.org/10.1021/acsenergylett.8b00249.

(111) Sun, F.; Moroni, R.; Dong, K.; Markötter, H.; Zhou, D.; Hilger, A.; Zielke, L.; Zengerle, R.; Thiele, S.; Banhart, J.; Manke, I. Study of the Mechanisms of Internal Short Circuit in a Li/Li Cell by Synchrotron X-Ray Phase Contrast Tomography. *ACS Energy Letters* **2017**, *2* (1), 94–104. https://doi.org/10.1021/acsenergylett.6b00589.

(112) Kazyak, E.; Garcia-Mendez, R.; Lepage, W. S.; Haslam, C.; Sakamoto, J.; Dasgupta, N. P. Li Penetration in Ceramic Solid Electrolytes: Operando Microscopy Analysis of Morphology, Propagation, and Reversibility. *Matter* **2020**, *2* (4), 1025–1048. https://doi.org/10.1016/j.matt.2020.02.008.

(113) Wang, M.; Wolfenstine, J. B.; Sakamoto, J. Temperature Dependent Flux Balance of the Li/Li 7 La 3 Zr 2 O 12 Interface. *Electrochimica Acta* **2019**, *296*, 842–847. https://doi.org/10.1016/j.electacta.2018.11.034.

(114) Sharafi, A.; Kazyak, E.; Davis, A. L.; Yu, S.; Thompson, T.; Siegel, D. J.; Dasgupta, N. P.; Sakamoto, J. Surface Chemistry Mechanism of Ultra-Low Interfacial Resistance in the Solid-State Electrolyte Li7La3Zr2O12. *Chem. Mater.* **2017**, *29*, 7961–7968. https://doi.org/10.1021/acs.chemmater.7b03002.

(115) Spencer Jolly, D.; Ning, Z.; Darnbrough, J. E.; Kasemchainan, J.; Hartley, G. O.; Adamson, P.; Armstrong, D. E. J.; Marrow, J.; Bruce, P. G. Sodium/Na B″ Alumina Interface: Effect of Pressure on Voids. *ACS Applied Materials & Interfaces* **2020**, *12* (1), 678–685. https://doi.org/10.1021/acsami.9b17786.

(116) LePage, W. S.; Chen, Y.; Kazyak, E.; Chen, K. H.; Sanchez, A. J.; Poli, A.; Arruda, E. M.; Thouless, M. D.; Dasgupta, N. P. Lithium Mechanics: Roles of Strain Rate and Temperature and Implications for Lithium Metal Batteries. *Journal of the Electrochemical Society* **2019**, *166* (2), A89–A97. https://doi.org/10.1149/2.0221902jes.

(117) Kasemchainan, J.; Zekoll, S.; Spencer Jolly, D.; Ning, Z.; Hartley, G. O.; Marrow, J.; Bruce, P. G. Critical Stripping Current Leads to Dendrite Formation on Plating in Lithium Anode Solid Electrolyte Cells. *Nature Materials* **2019**, *18* (10), 1105–1111. https://doi.org/10.1038/s41563-019-0438-9.

(118) Masias, A.; Felten, N.; Garcia-Mendez, R.; Wolfenstine, J.; Sakamoto, J. Elastic, Plastic, and Creep Mechanical Properties of Lithium Metal. *Journal of Materials Science* **2019**, *54* (3), 2585–2600. https://doi.org/10.1007/s10853-018-2971-3.

(119) Wang, M. J.; Chang, J.-Y.; Wolfenstine, J. B.; Sakamoto, J. Analysis of Elastic, Plastic, and Creep Properties of Sodium Metal and Implications for Solid-State Batteries. *Materialia* **2020**, *12*, 100792. https://doi.org/10.1016/j.mtla.2020.100792.

(120) Krauskopf, T.; Hartmann, H.; Zeier, W. G.; Janek, J. Toward a Fundamental Understanding of the Lithium Metal Anode in Solid-State Batteries - An Electrochemo-Mechanical Study on the Garnet-Type Solid Electrolyte Li 6.25 Al 0.25 La 3 Zr 2 O 12. *ACS Applied Materials and Interfaces* **2019**, *11* (15), 14463–14477. https://doi.org/10.1021/acsami.9b02537.

(121) Chen, K.-H.; Wood, K. N.; Kazyak, E.; LePage, W. S.; Davis, A. L.; Sanchez, A. J.; Dasgupta, N. P. Dead Lithium: Mass Transport Effects on Voltage, Capacity, and Failure of Lithium Metal Anodes. *Journal of Materials Chemistry A* **2017**, *5*, 11671–11691. https://doi.org/10.1039/C7TA00371D.

(122) Jin, Y.; Liu, K.; Lang, J.; Zhuo, D.; Huang, Z.; Wang, C. an; Wu, H.; Cui, Y. An Intermediate Temperature Garnet-Type Solid Electrolyte-Based Molten Lithium Battery for Grid Energy Storage. *Nature Energy* **2018**, *3* (9), 732–738. https://doi.org/10.1038/s41560-018-0198-9.

(123) Wang, M. J.; Choudhury, R.; Sakamoto, J. Characterizing the Li-Solid-Electrolyte Interface Dynamics as a Function of Stack Pressure and Current Density. *Joule* **2019**, *3* (9), 2165–2178. https://doi.org/10.1016/j.joule.2019.06.017.

(124) Jin, Y.; Liu, K.; Lang, J.; Jiang, X.; Zheng, Z.; Su, Q.; Huang, Z.; Long, Y.; Wang, C. an; Wu, H.; Cui, Y. High-Energy-Density Solid-Electrolyte-Based Liquid Li-S and Li-Se Batteries. *Joule* **2020**, *4* (1), 262–274. https://doi.org/10.1016/j.joule.2019.09.003.

(125) Lang, J.; Liu, K.; Jin, Y.; Long, Y.; Qi, L.; Wu, H.; Cui, Y. A Molten Battery Consisting of Li Metal Anode, AlCl 3-LiCl Cathode and Solid Electrolyte. **2019**. https://doi.org/10.1016/j.ensm.2019.07.027.

(126) Swamy, T.; Park, R.; Sheldon, B. W.; Rettenwander, D.; Porz, L.; Berendts, S.; Uecker, R.; Carter, W. C.; Chiang, Y.-M. Lithium Metal Penetration Induced by Electrodeposition through Solid Electrolytes: Example in Single-Crystal Li6La3ZrTaO12 Garnet. *J. Electrochem. Soc* **2018**, *165* (16), A3648-3655. https://doi.org/10.1149/2.1391814jes.

(127) Sharafi, A.; Meyer, H. M.; Nanda, J.; Wolfenstine, J.; Sakamoto, J. Characterizing the Li-Li7La3Zr2O12 Interface Stability and Kinetics as a Function of Temperature and Current Density. *Journal of Power Sources* **2016**, *302*, 135–139. https://doi.org/10.1016/j.jpowsour.2015.10.053.

(128) Virkar, A. V.; Viswanathan, L. Sodium Penetration in Rapid Ion Conductors. *Journal of the American Ceramic Society* **1979**, *62* (9–10), 528–529. https://doi.org/10.1111/j.1151-2916.1979.tb19123.x.

(129) Vashishta, P.; Mundy, J. N.; Shenoy, G. K. Fast Ion Transport in Solids : Electrodes, and Electrolytes. In *Fast ion transport in solids : electrodes, and electrolytes: Proceedings of the International Conference on Fast Ion Transport in Solids, Electrodes, and Electrolytesroceedings of the International Conference on Fast Ion Transport in Solids, Electrodes, a*; North Holland, 1979; pp 87–90.

(130) Manalastas, W.; Rikarte, J.; Chater, R. J.; Brugge, R.; Aguadero, A.; Buannic, L.; Llordés, A.; Aguesse, F.; Kilner, J. Mechanical Failure of Garnet Electrolytes during Li Electrodeposition Observed by In-Operando Microscopy. *Journal of Power Sources* **2019**, *412*, 287–293. https://doi.org/10.1016/j.jpowsour.2018.11.041.

(131) Chernyi, G. G.; Dryden, H. L.; Germain, P.; Howarth, L.; Olszak, W.; Prager, W.; Probstein, R. F.; Ziegler, H. Excerpt. In *Advances in Applied Mechanics*; 1966; Vol. 9, p 243.

(132) Sadd, M. Maxwell Model. In *Continuum Mechanics Modeling of Material Behavior*; 2019; pp 209–218.

(133) Anand, L.; Narayan, S. An Elastic-Viscoplastic Model for Lithium. *Journal of The Electrochemical Society* **2019**, *166* (6), A1092–A1095. https://doi.org/10.1149/2.0861906jes.

(134) Murday, J. S.; Cotts, R. M. Self-Diffusion Coefficient of Liquid Lithium. *The Journal of Chemical Physics* **1968**, *48* (11), 4938–4945. https://doi.org/10.1063/1.1668160.

(135) Cohen, M. H.; Turnbull, D. Molecular Transport in Liquids and Glasses. *The Journal of Chemical Physics* **1959**, *31*, 1164. https://doi.org/10.1063/1.1730566.

(136) Lodding, A.; Mundy, J. N.; Ott, A. Isotope Inter-Diffusion and Self-Diffusion in Solid Lithium Metal. *Physica Status Solidi (b)* **1970**, *38* (2), 559–569. https://doi.org/10.1002/pssb.19700380206.

(137) Dauison, H. W. *COMPILATION OF THERMOPHYSICAL PROPERTIES OF LIQUID LITHIUM*; 1968.

(138) Klinsmann, M.; Hildebrand, F. E.; Ganser, M.; McMeeking, R. M. Dendritic Cracking in Solid Electrolytes Driven by Lithium Insertion. *Journal of Power Sources* **2019**, *442*, 227226. https://doi.org/10.1016/j.jpowsour.2019.227226.

(139) Bucci, G.; Christensen, J. Modeling of Lithium Electrodeposition at the Lithium/Ceramic Electrolyte Interface: The Role of Interfacial Resistance and Surface Defects. *Journal of Power Sources* **2019**, *441*, 227186. https://doi.org/10.1016/j.jpowsour.2019.227186.

(140) Han, G.; Kinzer, B.; Garcia-Mendez, R.; Choe, H.; Wolfenstine, J.; Sakamoto, J. Correlating the Effect of Dopant Type (Al, Ga, Ta) on the Mechanical and Electrical Properties of Hot-Pressed Li-Garnet Electrolyte. *Journal of the European Ceramic Society* **2020**, *40* (5), 1999–2006. https://doi.org/10.1016/j.jeurceramsoc.2019.12.054.

(141) Diederichsen, K. M.; McShane, E. J.; McCloskey, B. D. Promising Routes to a High Li^+ Transference Number Electrolyte for Lithium Ion Batteries. *ACS Energy Letters* **2017**, *2* (11), 2563–2575. https://doi.org/10.1021/acsenergylett.7b00792.

(142) Gallagher, K. G.; Trask, S. E.; Bauer, C.; Woehrle, T.; Lux, S. F.; Tschech, M.; Lamp, P.; Polzin, B. J.; Ha, S.; Long, B.; Wu, Q.; Lu, W.; Dees, D. W.; Jansen, A. N. Optimizing Areal Capacities through Understanding the Limitations of Lithium-Ion Electrodes. *Journal of The Electrochemical Society* **2016**, *163* (2), A138–A149. https://doi.org/10.1149/2.0321602jes.

(143) Chen, K. H.; Namkoong, M. J.; Goel, V.; Yang, C.; Kazemiabnavi, S.; Mortuza, S. M.; Kazyak, E.; Mazumder, J.; Thornton, K.; Sakamoto, J.; Dasgupta, N. P. Efficient Fast-Charging of Lithium-Ion Batteries Enabled by Laser-Patterned Three-Dimensional Graphite Anode Architectures. *Journal of Power Sources* **2020**, *471*, 228475. https://doi.org/10.1016/j.jpowsour.2020.228475.

(144) Sawai, K.; Ohzuku, T. Factors Affecting Rate Capability of Graphite Electrodes for Lithium-Ion Batteries. *Journal of The Electrochemical Society* **2003**, *150* (6), A674. https://doi.org/10.1149/1.1568107.

(145) Minnmann, P.; Quillman, L.; Burkhardt, S.; Richter, F. H.; Janek, J. Editors' Choice—Quantifying the Impact of Charge Transport Bottlenecks in Composite Cathodes of All-Solid-State Batteries. *Journal of The Electrochemical Society* **2021**, *168* (4), 040537. https://doi.org/10.1149/1945-7111/abf8d7.

(146) Bielefeld, A.; Weber, D. A.; Janek, J. Modeling Effective Ionic Conductivity and Binder Influence in Composite Cathodes for All-Solid-State Batteries. *ACS Applied Materials & Interfaces* **2020**, *12* (11), 12821–12833. https://doi.org/10.1021/acsami.9b22788.

(147) Shi, T.; Tu, Q.; Tian, Y.; Xiao, Y.; Miara, L. J.; Kononova, O.; Ceder, G. High Active Material Loading in All-Solid-State Battery Electrode via Particle Size Optimization. *Advanced Energy Materials* **2020**, *10* (1), 1902881. https://doi.org/10.1002/aenm.201902881.

(148) Otoyama, M.; Ito, Y.; Hayashi, A.; Tatsumisago, M. Raman Imaging for LiCoO2 Composite Positive Electrodes in All-Solid-State Lithium Batteries Using Li2S–P2S5 Solid Electrolytes. *Journal of Power Sources* **2016**, *302*, 419–425. https://doi.org/10.1016/j.jpowsour.2015.10.040.

(149) Nomura, Y.; Yamamoto, K.; Hirayama, T.; Ohkawa, M.; Igaki, E.; Hojo, N.; Saitoh, K. Quantitative *Operando* Visualization of Electrochemical Reactions and Li Ions in All-Solid-State Batteries by STEM-EELS with Hyperspectral Image Analyses. *Nano Letters* **2018**, *18* (9), 5892–5898. https://doi.org/10.1021/acs.nanolett.8b02587.

(150) Yamamoto, K.; Iriyama, Y.; Hirayama, T. *Operando* Observations of Solid-State Electrochemical Reactions in Li-Ion Batteries by Spatially Resolved TEM EELS and Electron Holography. *Microscopy* **2016**, *66* (1), 50–61. https://doi.org/10.1093/jmicro/dfw043.

(151) Fakkao, M.; Chiba, K.; Kimura, Y.; Nakamura, T.; Okumura, T.; Nitta, K.; Terada, Y.; Uchimoto, Y.; Amezawa, K. Visualization of the Reaction Distribution in a Composite Cathode for an All-Solid-State Lithium-Ion Battery. *Journal of the Ceramic Society of Japan* **2017**, *125* (4), 299–302. https://doi.org/10.2109/jcersj2.16253.

(152) Masuda, H.; Ishida, N.; Ogata, Y.; Ito, D.; Fujita, D. In Situ Visualization of Li Concentration in All-Solid-State Lithium Ion Batteries Using Time-of-Flight Secondary Ion Mass Spectrometry. *Journal of Power Sources* **2018**, *400*, 527–532. https://doi.org/10.1016/j.jpowsour.2018.08.040.

(153) Masuda, H.; Ishida, N.; Ogata, Y.; Ito, D.; Fujita, D. Internal Potential Mapping of Charged Solid-State-Lithium Ion Batteries Using in Situ Kelvin Probe Force Microscopy. *Nanoscale* **2017**, *9* (2), 893–898. https://doi.org/10.1039/C6NR07971G.

(154) Höltschi, L.; Jud, F.; Borca, C.; Huthwelker, T.; Villevieille, C.; Pelé, V.; Jordy, C.; el Kazzi, M.; Novák, P. Study of Graphite Cycling in Sulfide Solid Electrolytes. *Journal of The Electrochemical Society* **2020**, *167* (11), 110558. https://doi.org/10.1149/1945-7111/aba36f.

(155) Kim, J. Y.; Park, J.; Lee, M. J.; Kang, S. H.; Shin, D. O.; Oh, J.; Kim, J.; Kim, K. M.; Lee, Y.-G.; Lee, Y. M. Diffusion-Dependent Graphite Electrode for All-Solid-State Batteries with Extremely High Energy Density. *ACS Energy Letters* **2020**, *5* (9), 2995–3004. https://doi.org/10.1021/acsenergylett.0c01628.

(156) Otoyama, M.; Kowada, H.; Sakuda, A.; Tatsumisago, M.; Hayashi, A. *Operando* Confocal Microscopy for Dynamic Changes of Li^{+} Ion Conduction Path in Graphite Electrode Layers of All-Solid-State Batteries. *The Journal of Physical Chemistry Letters* **2020**, *11* (3), 900–904. https://doi.org/10.1021/acs.jpclett.9b03456.

(157) Otoyama, M.; Sakuda, A.; Hayashi, A.; Tatsumisago, M. Optical Microscopic Observation of Graphite Composite Negative Electrodes in All-Solid-State Lithium Batteries. *Solid State Ionics* **2018**, *323*, 123–129. https://doi.org/10.1016/j.ssi.2018.04.023.

(158) Dahn, J. R. Phase Diagram of LixC6. *Physical Review B* **1991**, *44* (17), 9170–9177. https://doi.org/10.1103/PhysRevB.44.9170.

(159) Doyle, M.; Newman, J.; Gozdz, A. S.; Schmutz, C. N.; Tarascon, J. Comparison of Modeling Predictions with Experimental Data from Plastic Lithium Ion Cells. *Journal of The Electrochemical Society* **1996**, *143* (6), 1890–1903. https://doi.org/10.1149/1.1836921.

(160) Fuller, T. F.; Doyle, M.; Newman, J. Simulation and Optimization of the Dual Lithium Ion Insertion Cell. *Journal of The Electrochemical Society* **1994**, *141* (1), 1–10. https://doi.org/10.1149/1.2054684.

(161) Basu, S.; Zeller, C.; Flanders, P. J.; Fuerst, C. D.; Johnson, W. D.; Fischer, J. E. Synthesis and Properties of Lithium-Graphite Intercalation Compounds. *Materials Science and Engineering* **1979**, *38* (3), 275–283. https://doi.org/10.1016/0025-5416(79)90132-0.

(162) Dresselhaus, M. S.; Dresselhaus, G. Intercalation Compounds of Graphite. *Advances in Physics* **2002**, *51* (1), 1–186. https://doi.org/10.1080/00018730110113644.

(163) Uhlmann, C.; Illig, J.; Ender, M.; Schuster, R.; Ivers-Tiffee, E. In Situ Detection of Lithium Metal Plating on Graphite in Experimental Cells. *Journal of Power Sources* **2015**, *279*, 428–438. https://doi.org/10.1016/j.jpowsour.2015.01.046.

(164) Maire, P.; Evans, A.; Kaiser, H.; Scheifele, W.; Novák, P. Colorimetric Determination of Lithium Content in Electrodes of Lithium-Ion Batteries. *Journal of the Electrochemical Society* **2008**, *155* (11), 862–865. https://doi.org/10.1149/1.2979696.

(165) Grimsmann, F.; Gerbert, T.; Brauchle, F.; Gruhle, A.; Parisi, J.; Knipper, M. Hysteresis and Current Dependence of the Graphite Anode Color in a Lithium-Ion Cell and Analysis of Lithium Plating at the Cell Edge. *Journal of Energy Storage* **2018**, *15*, 17–22. https://doi.org/10.1016/j.est.2017.10.015.

(166) Harris, S. J.; Timmons, A.; Baker, D. R.; Monroe, C. Direct in Situ Measurements of Li Transport in Li-Ion Battery Negative Electrodes. *Chemical Physics Letters* **2010**, *485* (4–6), 265–274. https://doi.org/10.1016/j.cplett.2009.12.033.

(167) Shante, V. K. S.; Kirkpatrick, S. An Introduction to Percolation Theory. *Advances in Physics* **1971**, *20* (85), 325–357. https://doi.org/10.1080/00018737100101261.

(168) Liu, H.; Kazemiabnavi, S.; Grenier, A.; Vaughan, G.; di Michiel, M.; Polzin, B. J.; Thornton, K.; Chapman, K. W.; Chupas, P. J. Quantifying Reaction and Rate Heterogeneity in Battery Electrodes in 3D through Operando X-Ray Diffraction Computed Tomography. *ACS Applied Materials & Interfaces* **2019**, *11* (20), 18386–18394. https://doi.org/10.1021/acsami.9b02173.

(169) Newman, J. S.; Tobias, C. W. Theoretical Analysis of Current Distribution in Porous Electrodes. *Journal of The Electrochemical Society* **1962**, *109* (12), 1183. https://doi.org/10.1149/1.2425269.

(170) Kazyak, E.; Chen, K.-H.; Davis, A. L.; Yu, S.; Sanchez, A. J.; Lasso, J.; Bielinski, A. R.; Thompson, T.; Sakamoto, J.; Siegel, D. J.; Dasgupta, N. P. Atomic Layer Deposition and First Principles Modeling of Glassy Li_3BO_3–Li_2CO_3 Electrolytes for Solid-State Li Metal Batteries. *Journal of Materials Chemistry A* **2018**, 19425–19437. https://doi.org/10.1039/C8TA08761J.

(171) Kazyak, E.; Shin, M.; Lepage, W. S.; Cho, T. H.; Dasgupta, N. P. Molecular Layer Deposition of Li-Ion Conducting "Lithicone" Solid Electrolytes. *Chemical Communications* **2020**, *56* (99), 15537–15540. https://doi.org/10.1039/d0cc06077a.